Non-linear Transport Phenomena in Ultra-High Mobility Two-Dimensional Electron System

Zi Tong Wang, Department of Physics

McGill University, Montreal

November, 2022

A thesis submitted to McGill University in partial fulfillment of the requirements of the degree of

Master of Physics

Abstract

At low temperature and weak magnetic field (B), and under a strong DC current I_{DC}, a two-dimensional electron gas (2DEG) can exhibit a variety of non-linear transport phenomena, which we refer to as phases. In an ultra-high mobility (μ=20 $\times$ 10^6 cm^2/Vs) narrow (15 μm wide) GaAs/AlGaAs Hall bar, with DC current densities up to 0.67 A/m, the various phases are captured together in a single phase diagram, a differential resistivity map of B-field versus DC current. Around zero current, we observe $1/B$ periodic Shubnikov-de Haas (SdH) oscillations and phase inversion of SdH oscillations. Around zero B-field, we observe a negative magnetoresistance and a double peak feature, which are both signs of ballistic electron transport. At high DC current, we observe strong I_{DC}/B oscillations known as Hall-induced resistance oscillations (HIROs). The object of this thesis is to give a general overview of the weak B-field strong DC current phase diagram of 2DEG, as we introduce and report on each of these phases, giving extra emphasis to HIROs. In the work presented in this thesis, we compare our experimental data to existing theories to extract parameters of interest. Notably, we find a difference between the quantum lifetime τ_q extracted from SdH oscillations and from HIROs, an unexpected half-integer HIRO-like feature, and evidence of DC current-induced electron hydrodynamic transport.

Abrégé

À basse température et sous un faible champ magnétique (B), et sous un fort courant DC I_{DC}, un gaz électronique en deux dimensions (GE2D) peut présenter une variété de phénomènes de transport non linéaires, que nous appelons des phases. Dans une barre à effet de Hall composé de GaAs/AlGaAs à ultra-haute mobilité (μ=20 $\times$ 10^6 cm^2/Vs) et étroite (15 μm), avec des densités de courant continu allant jusqu'à 0.67 A/m, les différentes phases sont capturées ensemble dans un diagramme de phase, une représentation graphique de résistivité différentielle du champ magnétique en fonction du courant DC. Autour du zéro courant, nous observons des oscillations périodiques à $1/B$ de l'effet de Shubnikov-de Haas (SdH) et une inversion de phase des oscillations de SdH. Autour du zéro champ magnétique, nous observons une magnétorésistance négative et une caractéristique de double pics, qui sont tous des signes de transport balistique d'électrons. A fort courant continu, nous observons de fortes oscillations à I_{DC}/B connues sous le nom d'oscillations de résistance induites par Hall (HIROs). L'objetif de cette thèse est de donner une vue d'ensemble du diagramme de phase dans un champ B faible et sous un fort courant continu dans un GE2D, en introduisant et en expliquant chacune de ces phases, en concentrant surtout sur les HIROs. Dans le travail présenté dans cette thèse, nous comparons nos données expérimentales aux théories existantes pour extraire les paramètres d'intérêt. En particulier, nous trouvons une différence entre la durée de vie quantique τ_q

extraite des oscillations de l'effet de SdH et des HIROs, une résonance qui ressemble aux HIROs à demi-entier des HIROs, et des signes du transport hydrodynamique d'électrons induit par le courant continu.

Acknowledgements

This Master's thesis was completed in the department of physics at McGill University. I would like to thank my supervisor, Professor Michael Hilke, for guiding me through the Master's program and for giving me the opportunity to study physics with him as a student. I would also like to thank professor Sergei Studenikin and professor Guy Austing at National Research Council Canada who have helped me a lot and have given me the opportunity to participate in their research together with professor Hilke.

Statement of Contributions

The content of this thesis describes largely the results presented in a soon-to-be published manuscript titled "Non-linear Transport Phenomena and Current-induced Hydrodynamics in Ultra-high Mobility Two-dimensional Electron Gas" [1]. This work was performed in collaboration with professors Sergei Studenikin, Guy Austing, N. Fong from the Emerging Technology Division at the National Research Council of Canada (NRC), and with professors Kenneth West, Loren Pfeiffer from Princeton University. The group from Princeton provided the ultra-high mobility GaAs/AlGaAs material. The group at NRC performed data measurements of the Hall bar. Professor Michael Hilke and the author of this thesis worked principally on the data analysis.

Table of Contents

Abstract i

Abrégé ii

Acknowledgements iv

Statement of Contributions v

List of Figures xi

List of Tables xii

I Background Information **1**

1 Introduction **2**

1.1 Phase Diagram 3

1.2 Shubnikov-de Hass Oscillations 5

1.3 Phase Inversion of The SdH Oscillations 7

1.4 Negative Magnetoresistance 8

1.5 Hall-Field Induced Resistance Oscillations 10

1.6 DC Current-Induced Electron Hydrodynamic Transport 10

1.7 Thesis Overview 13

2 Literature Review of HIROs **15**

2.1 Theoretical Framework 16
2.2 Experimental Studies 25

3 Experimental Setup **27**

II Analysis of Experimental Data **30**

4 Hall-Field Induced Resistance Oscillations **31**
4.1 I_{DC}/B Dependence 31
4.2 Quantum Parameters Extracted from HIROs 33
4.3 Small DC Current Dip 38
4.4 Fractional HIROs 39

5 Shubnikov-de Haas Oscillations **42**
5.1 Extraction of τ_q and R_0 43
5.2 Phase Inversion 44

6 Negative Magnetoresistance at Zero Magnetic Field **47**
6.1 Origin of Negative Magnetoresistance 47
6.2 Double Peak 47

7 Hydrodynamic Electron Transport **50**
7.1 Current-Induced Suppression of Electron-Electron Scattering Mean Free Path 50
7.2 Hydrodynamic Magnetoresistance 54
7.2.1 Isolating The Hydrodynamic Contribution 56
7.2.2 Comparison to Theory Using a Perturbative Method 57
7.3 Hydrodynamic Hall Resistivity 60

8 Conclusion **64**

8.1 Summary of Parameters Extracted 64
8.2 Summary of The Phase Diagram 66
8.3 Outline for Future Research 67
8.3.1 Boltzmann Transport Theory Analysis for DC Current-Induced Hydrodynamic Electron Transport 68

A GaAs/AlGaAs Hetero-Structure Fabrication Process **70**

B Hall Resistivity Under Illumination **72**

List of Figures

1.1 Phase diagram of differential resistivity ρ_{xx} vs magnetic field and I_{DC}. . . . 4

1.2 Thermal damping factor D_T versus its derivative with respect to T, plotted versus B-field. 9

1.3 Cartoon simplifying the difference between an electron in the ballistic regime versus hydrodynamic regime. 12

2.1 Differential resistivity ρ_{xx} versus B-field at different DC current showing HIROs. 17

2.2 Landau level transition between spatially tilted Landau levels in a 2DEG under magnetic field and in an electric field. 18

2.3 ρ_{xx} versus I_{DC} at various fixed B-fields. 21

2.4 Normalized differential resistivity calculated from theory Eq. (2.10) of HIROs versus current density j. 24

3.1 Central region of the Hall bar device used for the measurements presented in this thesis. 28

4.1 Fan diagram of HIRO maxima in $\partial\rho_{xx}/\partial|B|$ for each peak up to the sixth order. 32

4.2 HIRO amplitudes in $\partial\rho_{xx}/\partial|B|$ vs B-field fitted to theory, and parameters τ_q and W_{eff} versus I_{DC} extracted from fits. 34
4.3 Arrhenius plot versus $1/B$ of SdH oscillations extrema amplitudes (at I_{DC} = 0 μA) and HIRO extrema amplitudes at I_{DC}=5 μA, in R_{xx}. 37
4.4 HIROs amplitude $\Delta\rho_{xx}$ at B=0.06T plotted versus I_{DC}, experimental data compared to theory. 38
4.5 Differential resistivity ρ_{xx} traces versus B-field for a range of I_{DC} values offset from each other by 0.06 Ω. The "1.5" feature can be observed around $|B|$=0.12 T. 39
4.6 Differential resistivity ρ_{xx} at HIRO maxima in the $-$B-field and $-I_{DC}$ quadrant of the phase diagram, extracted by peak order M and plotted versus I_{DC}. 41

5.1 Resistivity R_{xx} versus B-field at I_{DC}=0 μA and AC current equal to 40 nA. . 42
5.2 SdH oscillations amplitude ΔR_{xx} at I_{DC}=0 μA and AC current equal to 40 nA plotted versus filling factor ($\nu \propto 1/B$), theory fitted to experimental data. 44
5.3 Grayscale plots showing phase inversion of SdH oscillation amplitude Δr_{xx} in differential resistance vs B and I_{DC}, experiment compared to theory. . . . 45
5.4 Electron temperature T_e and $\partial T/\partial I$ plotted versus I_{DC}. theory and from fitting. 46

6.1 Resistivity R_{xx} versus B-field at I_{DC}=0 μA and AC current equal to 40 nA, focused on nMR. 48
6.2 Phase diagram of the differential resistivity ρ_{xx} focused on the double peak feature on top of nMR. 49

7.1 Prediction of electron-electron scattering mean free path l_{ee} versus I_{DC}. . . . 52

7.2 Differential resistivity ρ_{xx} versus I_{DC} for different B-fields. 53
7.3 $\Delta\rho_{xx}$, the change in differential resistivity ρ_{xx} versus increasing I_{DC}, experiment compared to theory. 55
7.4 $\Delta\rho^{*}_{xx}$=$\rho_{xx} - \Delta\rho^{bg}_{xx}$ at $B = 0$ T plotted versus DC current. 56
7.5 Differential resistivity ρ_{xx} plotted versus B-field for different DC currents and subsequent steps to the method used to isolate the DC current-induced hydrodynamic component of ρ_{xx}. 58
7.6 ρ_{xx}-$\rho^{I=0}_{xx}$, deviation of differential resistivity ρ_{xx} from ρ_{xx} at I_{DC}=0 μA. 59
7.7 Electron-electron scattering length l_{ee} and $|r_H|$ extracted from fits of the traces in Fig. 7.5(c) versus DC current. 60
7.8 Hall resistivity ρ_{xy} plotted versus B-field for I_{DC}=0 μA, 4 μA, 8 μA. 61
7.9 Deviation from Hall resistivity $\Delta\rho_{xy}$=$\rho_{xy}$$-$$\rho^{bulk}_{xy}$, $\Delta\rho_{xy}/\rho^{bulk}_{xy}$ and Isolated hydrodynamic component $\Delta\rho^{*}_{xy}/\rho^{bulk}_{xy} = (\Delta\rho_{xy} - \Delta\rho_{xy,I=0})/\rho^{bulk}_{xy}$ versus B-field. 63

8.1 Summary of the observed nonlinear phenomena regions and boundaries in a phase diagram of ρ_{xx} vs B and I_{DC}. 67

A.1 Schematic of the layers of the 2DEG with quantum well doping. 71

B.1 Electron concentration n obtained from Hall resistivity plotted versus illumination time. 72
B.2 $\Delta\rho_{xy}/\rho^{bulk}_{xy}$ plotted versus B-field after different illumination time, without DC current and with DC current of 8 μA. 73

List of Tables

3.1 Key parameters of the Hall bar and the 2DEG material system. 29

8.1 Summary of key extracted parameters extracted. 66

List of Acronyms

2DEG 2-Dimensional Electron Gas

HIROs Hall-Induced Resistance Oscillations

MBE Molecular Beam Epitaxy

nMR Negative Magnetoresistance

QW Quantum Well

SdH Shubnikov-De Haas

Part I

Background Information

1. Introduction

In low dimensional physics, the two-dimensional electron gas (2DEG) has been one of the most studied systems in the past four decades. The extensive experimental studies have made remarkable discoveries, most notably the integer quantum hall effect [2] and the fractional quantum hall effect [3]. 2DEGs are made from semiconductor materials. Recently, with modern fabrication techniques such as molecular beam epitaxy (MBE), we now have access to low disorder, high mobility 2DEG systems. In these high mobility 2DEGs, non-linear phenomena have been discovered at high filling factors (very small magnetic fields), such as Hall-field induced resistance oscillations [4] and microwave induced resistance oscillations [5], which we refer to as phases. These various phases have received significant interest in the past two decades [6, 7].

This thesis focuses on the experimental investigations of non-linear transport of a 2DEG in an ultra-high mobility (μ=20×10^6 cm^2/Vs) narrow (15 μm wide) GaAs/AlGaAs Hall bar, under DC current densities up to 0.67 A/m. Under DC current and in the presence of a weak perpendicular magnetic field, Hall-field induced resistance oscillations (HIROs) can be observed. Previously published experimental works on HIROs have mostly focused on the magnetoresistance of HIROs, where the data are usually presented in a resistivity vs B-field plot at fixed DC current [4, 8–21]. However, the low magnetic field high DC current regime is filled with a rich set of phases, other than HIROs. The

object of our research is to present this regime and its various phases by mapping out the resistance versus both B-field and DC current. This top-down approach allows us to present to the reader a complete picture of the low B-field high DC current regime in one place and from a single sample. This method also allows us to understand the possible relationships between the observable phenomena, and has previously been used successfully in the high magnetic field regime [22–24].

To properly introduce the phases discussed in this thesis, we start by presenting a map of the measured differential resistivity ρ_{xx} along the direction Hall bar versus B-field and DC current, which we refer to as the phase diagram. Then, from the phase diagram, we identify the relevant regions of each phase, as well as their boundaries. For each non-linear phenomenon, we give a review of the background information. Lastly, we present an overview of the content of this thesis.

1.1 Phase Diagram

We start by presenting the phase diagram, a plot of the magneto-resistivity ρ_{xx} in differential resistivity versus DC current I_{DC} up to 10 μA and B-field up to 0.25 T, of a narrow (W=15 μm) and ultra-high mobility (μ=20$\times 10^6$) Hall bar [see Fig. 1.1(a)]. In the phase diagram, there are various non-linear phenomena that we can identify with their own regions and boundaries, which we refer to as phases. Each phase is a feature of the phase diagram that can tell us more about the properties of 2DEG such as how charge carriers in the system interact with impurities, with the boundaries and with each other. Specifically, by comparing the phases to existing theories, we are able to validate our current understandings of non-linear phenomena with experimental data, and extract parameters of interest such as the electronic width, the quantum lifetime and the electron temperature. In the phase diagram, we can identify five distinct phases: Shubnikov-de Haas oscillations

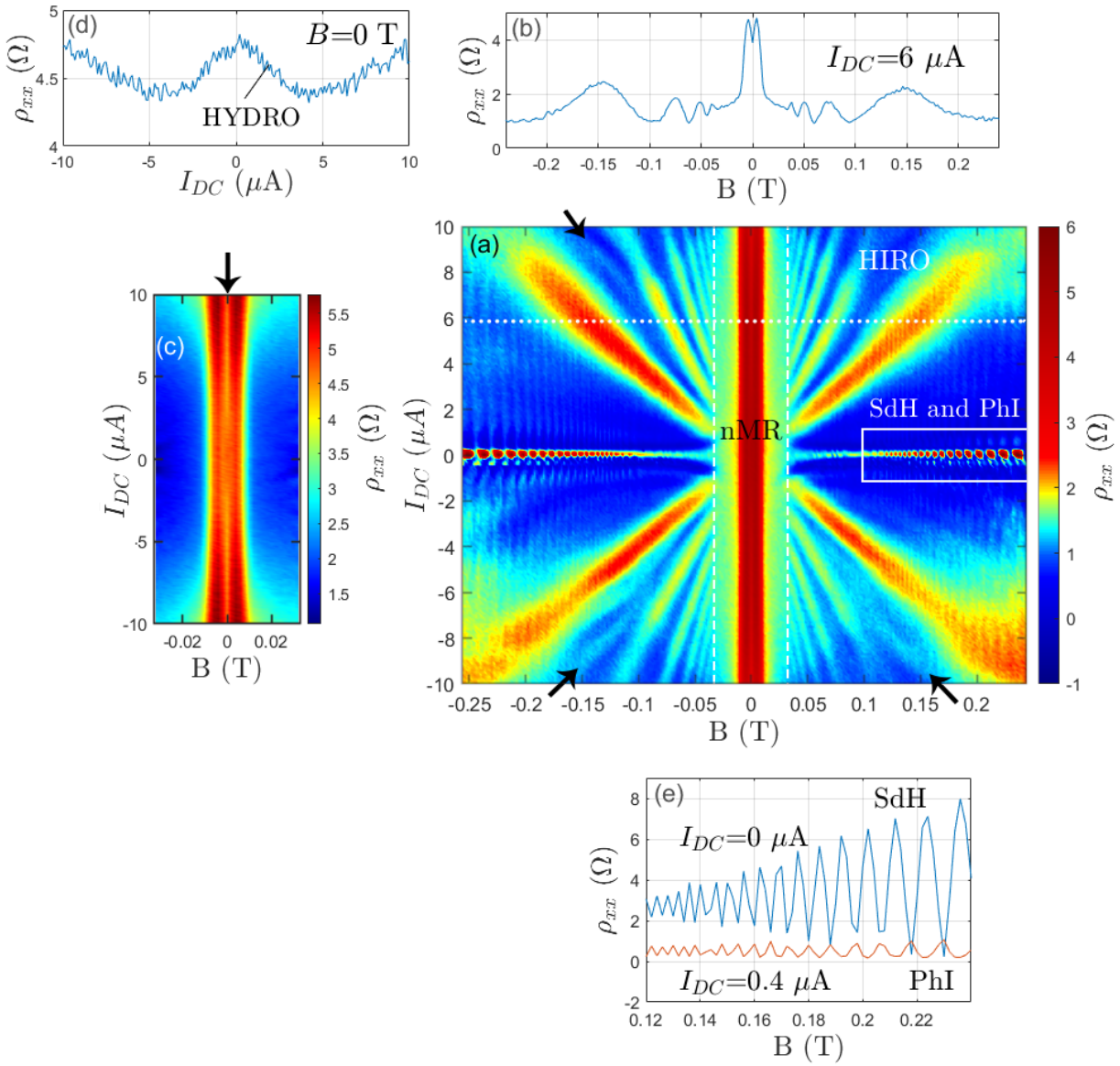

Figure 1.1: a) Phase diagram of differential resistivity ρ_{xx} vs B and I_{DC} (A background parabolic dependence with I_{DC} and a small uniform linear dependence with B-field are subtracted from the raw data to emphasize the features of interest in the phase diagram). b) Horizontal cross section of the phase diagram at I_{DC}=6 μA, where HIROs and nMR can be observed. c) Expanded view of the phase diagram around B=0 T (raw data). A double peak can be observed on top of the nMR. The background parabolic dependence can be observed at ∼0.2 T. d) Vertical cross section of the phase diagram at B=0 T. A decrease in ρ_{xx} with increasing current is a sign of a hydrodynamic effect [25]. e) ρ_{xx} vs B at I_{DC}=0 μA and I_{DC}=0.4 μA, where SdH oscillations and a phase inversion (PhI) of the SdH oscillations can be observed.

(SdH), phase inversion of the SdH oscillations, negative magnetoresistance around B=0 T (nMR), Hall-field induced resistance oscillations (HIROs), and evidence of DC current-induced electron hydrodynamics (HYDRO). The phases are identified in Fig. 1.1. In this thesis, we will mainly focus on the topic of HIROs which is a spectacular manifestation of non-linear behavior. Nonetheless, we also introduce and report on the findings from the four other phenomena of the phase diagram, in order to give a general picture to the reader. The phase diagram analysis approach is motivated by a lack of a comprehensive experimental analysis of more than one low B-field non-linear phenomenon in the literature. This method has merits, as we will see later, when parameters obtained from the analysis of one phase can be relevant or compared to parameters obtained from the analysis of another phase.

1.2 Shubnikov-de Hass Oscillations

SdH oscillations are $1/B$ oscillations in the resistivity in the presence of a small magnetic field at low temperature [26–29]. In the phase diagram presented in Fig 1.1(a), these oscillations can be identified as horizontal waves for $|B| > 0.1$ T, although the theoretical formulation does not take into account DC current. SdH oscillations are best observed at zero DC current, where they have the largest amplitudes [see Fig. 1.1(e) and Fig. 1.2]. Analysis of SdH oscillations is useful to extract parameters, notably the quantum lifetime and the effective mass.

SdH oscillations arise from the magneto-oscillation of the density of states (DOS) in a small magnetic field. At zero magnetic field, the DOS of a 2DEG is constant and equal to $\nu_0 = m^*/\pi\hbar^2$, where m^* is the effective mass. In a magnetic field perpendicular to the sample, taking into account disorder and temperature, the DOS can be approximated by the overlap of a series of Gaussian functions at each Landau level. An approximation of

the DOS takes the form of [7]:

$$\nu(\epsilon) = 1 - 2\lambda cos\left(\frac{2\pi\epsilon}{\hbar\omega_c}\right) \tag{1.1}$$

where $\lambda = exp(-\pi/\omega_c\tau_q)$ is the Dingle factor, $\omega_c = eB/m^*$ is the cyclotron frequency, τ_q is the quantum lifetime. When a magnetic field is applied to a solid state material, the charge carrier's energy spectrum is quantized because of the quantization of the cyclotron orbits, which are characterized by Landau levels separated to the next immediate energy level by the cyclotron energy $\hbar\omega_c$. The Landau level separation increases with increasing B-field, and the oscillatory nature of the DOS affects the conductivity. The resistivity peaks when a Landau level crosses the Fermi energy, which is the source of the SdH oscillations. In the small B-field regime, we can analytically describe the SdH oscillations in the resistance $R_{xx} = V_{xx}/I$ (which is equivalent to the differential resistance in the limit of zero DC current) by the conventional Ando formula [30,31]:

$$\Delta R_{xx} = 4R_0 D_T \cos\left(\frac{2\pi E_F}{\hbar\omega_c} - \pi\right) \exp\left(-\frac{\pi}{\omega_c\tau_q}\right), \tag{1.2}$$

where ΔR_{xx} is the SdH oscillation resistance amplitude, R_0 is the zero field resistance, and D_T is the thermal damping factor:

$$D_T = \frac{X_T}{\sinh(X_T)}, \quad X_T = \frac{2\pi^2 k_B T}{\hbar\omega_c}. \tag{1.3}$$

Here k_B is the Boltzman constant and T is the temperature. From the Dingle factor in Eq. (1.2), we can conclude that SdH oscillations are observable for $\omega_c\tau_q \gg 1$, which defines the SdH boundary B_q, the B-field value where $\omega_c\tau_q = 1$. This condition effectively means that the separation of the Landau levels ($\hbar\omega_c$) must be greater than the broadening of each level equal to $\hbar/\tau_q$. For SdH oscillations to be observed, $\hbar\omega_c \gg k_B T$ must also be

satisfied, which states that the separation between Landau levels must be greater than the thermal broadening. This condition is described in the thermal damping factor. Finally, oscillations appear for $E_F \gg \hbar\omega_c$, where there is degeneration of the 2DEG, which sets an upper B-field limit for SdH oscillations. For an extensive review of SdH oscillations see Refs. [6,7].

1.3 Phase Inversion of The SdH Oscillations

In the phase diagram, SdH oscillations can be observed to persist at non-zero DC current. Their amplitude decreases exponentially away from I_{DC}=0 μA. Interestingly, the SdH oscillations become phase inverted around $I_{DC} \sim 0.3\ \mu A$, meaning the peaks and troughs of the oscillations are inverted, or shifted by a phase π. Beyond $I_{DC} \sim 0.3\ \mu A$, the SdH oscillations are entirely inverted [see Fig. 1.1(e)]. This phenomenon has been observed previously in the differential resistance of SdH oscillations in graphene [32] and in InGaAs/InP quantum well [33]. A model by Studenikin *et al.* [33] describes a phase inversion of SdH oscillations in differential resistance by a DC current-induced electron temperature dependence. Specifically, the phase inversion emerges from a conversion of the SdH oscillations correction in resistance ΔR_{xx}^{SdH} in Eq. 1.2 to differential resistance Δr_{xx}^{SdH}, taking into account a temperature dependent on DC current, such that

$$r_{xx} = \frac{\partial V_{xx}}{\partial I} = R_{xx} + I_{DC}\frac{\partial \Delta R_{xx}^{SdH}}{\partial T_e}\frac{\partial T_e}{\partial I}, \tag{1.4}$$

where T_e is the electron temperature, V_{xx} is the potential across the probe, $r_{xx} = R_0 + \Delta r_{xx}^{SdH}$, $R_{xx} = R_0 + \Delta R_{xx}^{SdH}$, R_0 is the bulk resistance. The derivative of ΔR_{xx}^{SdH} with respect to T is negative and introduces a phase inverted oscillatory component (see D_T versus $\partial D_T/\partial T$ versus B-field in Fig. 1.2). From this model, at large enough DC current,

a phase inversion occurs when the second term of the right side of Eq. (1.4) is larger than R_{xx}. This model also accounts for the decreasing amplitude of SdH oscillations with increasing I_{DC}, explained by an increase in electron temperature due to DC current. The parameter of interest is $T_e(I_{DC})$. In Studenikin *et al.* [33], the electron temperature was calibrated to I_{DC}, which had the form:

$$T_e = T_0 + \alpha I_{DC}^{\beta} \tag{1.5}$$

where I_{DC} is in μA, T_0 is the bath temperature, α and β are constants. α and β were found to be 0.487 and 2/3, respectively. The $2/3$ dependence was explained by a power dissipation related to T^3, which is consistent with previous experimental works on 2DEG [34,35]. In our phase diagram, the phase inversion happens at ~ 0.3 μA around 0.2 T. The boundary of the phase inversion is dependent on B-field, which we will refer to as I_{PhI}.

1.4 Negative Magnetoresistance

Around zero magnetic field, a strong negative magnetoresistance can be observed [see Fig. 1.1(a), (c)]. At zero DC current, the nMR has a sharp change of slope around 10mT and also has a double peak feature at $\sim$ 5 mT. As the DC current increases, the nMR feature persists and the double peak feature widens. Both are signs of ballistic transport [36–38], which is a regime where the width of the sample is smaller than the transport mean free path and the electron-electron scattering length. In this regime, electron transport is dominated by scattering events with the 2DEG boundaries (see Fig. 1.3). In a theoretical work by Scaffidi *et al.* [36], a sharp change of slope at $W_{eff} = 2r_c$ and a peak at $W_{eff} \simeq 0.55r_c$ in the magnetoresistance were both attributed to be signs of ballistic transport in a 2DEG. In general, the resistivity of a material is caused by scattering of the charge

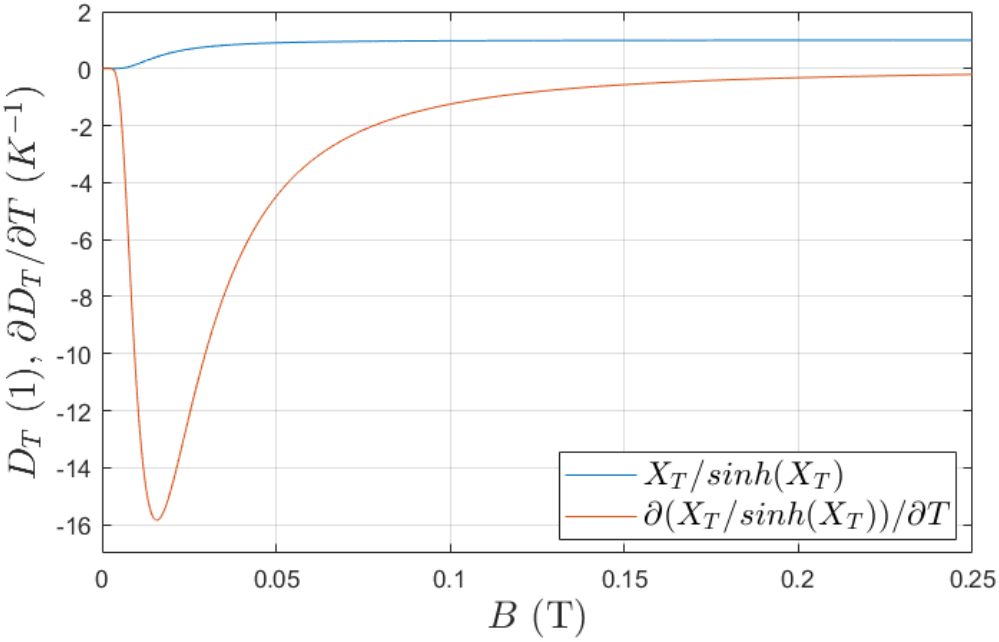

Figure 1.2: Thermal damping factor D_T in Eq. (1.3) versus its derivative with respect to T, evaluated at $T = 40$ mK and plotted versus B-field. The derivative of D_T with respect to the temperature T is negative, which introduces a phase inversion at large enough I_{DC} in Eq. (1.4), given that the electron temperature depends on current.

carriers inside of the material. In the ballistic transport regime, the resistance is mainly affected by charge carriers scattering off the boundaries of the 2DEG. When $W_{eff} = 2r_c$, the diameter of the cyclotron orbit of an electron is equal to the width of the 2DEG. In a stronger B-field ($W_{eff} > 2r_c$), an electron cannot scatter from one side of the 2DEG to the other side, except by scattering off impurities in the material. This results in a decrease of the resistivity and the sharp change of slope of the magnetoresistance at $W_{eff} = 2r_c$. Physically, the double peak feature can be explained by interactions of the charge carriers with the side contacts under a magnetic field, which results in an increase in magnetoresistance. In an experimental work by Gusev *et al.* [39], it was shown that the configuration of measurement of the voltage across the length of the Hall bar has a significant effect on the double peak feature. The double peak feature has also been observed experimen-

tally in previous works [37, 40–43]. In general, nMR has been observed in high-mobility 2DEG Hall bar devices [44–55], quantum wires and quantum point contacts [40, 56–59]. In Refs. [46, 60, 61], the nMR was associated with weak localization. For our sample, the mean free path is larger than the Hall bar width, and coherent backscattering is negligible, so we can rule out weak localization.

1.5 Hall-Field Induced Resistance Oscillations

Hall field-induced resistance oscillations (HIROs) are I_{DC}/B oscillations in the resistivity observable in the presence of a DC current. In our phase diagram, these oscillations are the sharp diagonal resonances at non-zero magnetic field and DC current. The first order resonance is the one closest to the B-field axis [see Fig. 1.1(a)]. Subsequent resonance orders approach the DC current axis. In our sample, we observe up to 7 resonances in all four quadrants. HIROs were first observed in 2002 by Yang *et al.* [4] and were attributed to a Zener tunneling effect between Landau levels tilted by the electric field. The origin of the Landau level transition is elastic scattering of electrons off impurities. A detailed literature review of HIROs is presented in Chapter 2.

1.6 DC Current-Induced Electron Hydrodynamic Transport

In our phase diagram, at zero magnetic field, the differential resistivity ρ_{xx} first decreases with increasing DC current, and then increases at around 4 μA [see Fig. 1.1(d)]. We attribute the decrease in ρ_{xx} at zero B-field to be a sign of DC current-induced electron hydrodynamic transport. We can exclude umklapp processes and weak electron phonon coupling because we use an ultra-high mobility 2DEG in a GaAs/AlGaAs heterostructure [25]. We can also exclude weak localization because of our sample's long mean free

path ($l_{mfp} = 145$ μm). Thus, electrons in the 2DEG interact with the boundaries and/or potentially with each other. This phenomenon was previously reported in high-mobility 2DEG of (Al,Ga)As electron wires under DC current by Molenkamp and De Jong [25,62], which was attributed to be hydrodynamic in nature.

Electron hydrodynamic transport has become a reemerging topic of significant interest recently. The possibility of viscous electronic flow was originally theorized by Gurzhi [63, 64] in the 1960's. Conventionally, electronic transport is determined by momentum relaxing (MR) collision of electrons (electron-impurity for instance). On the other hand, electron-electron collisions are momentum conserving, and should not affect the conductivity. When the electron-boundary collisions are more frequent than MR collisions of electrons, the electron transport is ballistic in nature [36]. Gurzhi suggested that electrons flow differently in a system when the MC electron-electron collisions are more frequent than both the momentum relaxing electron-impurity collisions and boundary collisions, at low temperatures. As a result, electrons away from the boundaries undergo many fewer collisions with the boundaries due to collisions with each other before reaching the boundaries. Additionally, if the width of the electronic system is also less than the mean free path, the electrons are much less likely to undergo momentum relaxing collisions. Under these conditions, the electrons flow through the channel like a hydrodynamic fluid (see Fig. 1.3). In summary, there are three relevant length scales: sample width W, classical mean free path l_{mfp} (MR) and electron-electron scattering length l_{ee} (MC). The three length scales define three limiting transport regimes: Ohmic ($l_{mfp} \ll W$), ballistic ($W \ll l_{ee}, l_{mfp}$) and hydrodynamic ($l_{ee} \ll W \ll l_{mfp}$). Effectively, the validity of the hydrodynamic regime can be determined by the detection of a hydrodynamic correction to the resistivity of a material.

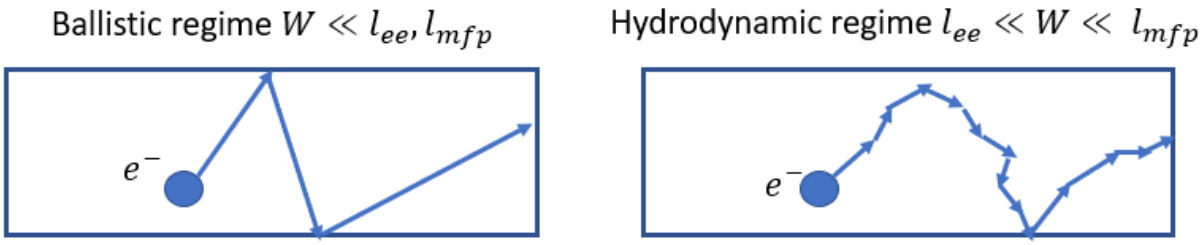

Figure 1.3: Cartoon simplifying the difference between an electron in the ballistic regime versus hydrodynamic regime. In the hydrodynamic regime, the electron undergoes momentum-conserving scattering collisions.

Since the proposition by Gurzhi, there has been numerous theoretical studies on the topic of electron hydrodynamic transport [25, 65–74]. Experimental studies in the 1990s used high-mobility GaAs/AlGaAs hetero-structure wires to report on the Knudsen and Poiseuille (Gurzhi) transport regimes in the differential resistance [25, 62, 68]. In recent years, following the development of high mobility materials with high transport mean free path, there has been a renewed interest in electron hydrodynamics. New theoretical works [36, 75–82] furthered our understanding of the viscous contribution in semiconductor 2DEG. New experimental works studied hydrodynamic effects in the 2D systems of graphene [43, 83–91], high-mobility semiconductor 2DEGs [39, 42, 47, 52, 82, 92–99], 2D metals [42], and semi-metal micro-ribbons [92].

Commonly used methods of reaching the hydrodynamic regime are temperature-induced suppression of l_{ee} and reduction of the channel width in steps [42]. The temperature-induced suppression of l_{ee} is a theoretical prediction by Giuliani and Quinn [65]. A similar prediction with DC current was also made by the same author, which is the basis of current-induced viscous transport in our work.

1.7 Thesis Overview

The thesis is organized in 7 chapters.

With HIROs being the principle topic of this thesis, in Chapter 2, we review the experimental and theoretical works on HIROs. Specifically, we present the theoretical framework developed to understand nonequilibrium corrections of the magnetoresistance under DC current. The theory presented in this section will be used extensively in Chapter 4 for the analysis of the experimental data of HIROs.

The data presented in this thesis are from measurements of a Hall bar under magnetic field and DC current. The experimental setup and relevant details about the instrumentation are presented in Chapter 3. Following this chapter, the next chapters describe the analysis of each phase observable from the experimental data.

Chapter 4 presents the analysis of HIROs with the theoretical models presented in Chapter 2. From the analysis, we extract parameters of interest, namely the effective width of the Hall bar, the backscattering lifetime, the quantum lifetime τ_q and the inelastic relaxation lifetime. Our study shows a DC current dependence of τ_q and a discrepency between τ_q extracted from HIROs and extracted from SdH oscillations. We also report on an unexpected "fractional" HIRO-like feature between the first and second order maxima.

In Chapter 5, we present our analysis of the SdH oscillations. We compare our data to a model of SdH oscillations under DC current in differential resistivity based on a DC current-induced electron temperature dependence, which is described in Sec. 1.3. This model explains both the decreasing amplitude of SdH oscillations with increasing DC current and the phase inversion.

Chapter 6 describes our observation of the negative magnetoresistance at zero magnetic field. The main topic of this chapter is to characterize this phenomenon and investigate its origin. The noticeable double peak feature's dependence with DC current is also explored.

Lastly, in Chapter 7, we present evidence of DC current-induced electron hydrodynamic transport. first, we present evidence of DC current-induced suppression of the electron-electron scattering length, which is an essential condition for the hydrodynamic regime. Then, we identify the contributions in the deviation of the magnetoresistance with DC current in the near-zero magnetic field. Following the background information presented in Sec. 1.6, we compare the data to theoretical hydrodynamic models.

The concluding Chapter 8 summarizes the findings from the analysis of all the phases observable from the phase diagram. We also discuss the significance of our work and detail possible directions for experiment and analysis in the future.

2. Literature Review of HIROs

Hall field-induced resistance oscillations (HIROs) are a type of $1/B$ magnetoresistance oscillations observable in the presence of a DC current. These oscillations are observed in the resistivity at high filling factors in a 2DEG system. In this case, the DC current is applied along the length of the Hall bar and the B-field is applied perpendicularly to the Hall bar. An example of HIROs obtained from our sample are presented in Fig. 2.1. HIROs were first observed in 2002 by Yang *et al.* [4]. The origins of the HIRO oscillation frequency with respect to B-field and DC current were explained by a Zener tunneling process between Landau orbits [4]. The discovery of HIROs gained interest and led to various experimental works [8–21] and theoretical studies [6, 7, 100–103] in the last two decades to gain better understanding of this type of oscillations. Experimental works have helped characterize more properties of this non-linear effect such as the near zero DC current dip. Theoretical studies have suggested two mechanisms to explain HIROs, which are elastic scattering of electrons off of impurities, and inelastic correction to the electron distribution function induced by DC current [101, 102].

In this chapter, we review the experimental and theoretical development of HIRO in the last two decades. Alongside a presentation of the experimental works, we also review the Zener tunneling process originally proposed by Yang *et al.* [4] and the elastic and

inelastic theory model by Vavilov et al. [102]. Lastly, we discuss details of the methods to compare the theoretical framework to the experimental data.

2.1 Theoretical Framework

In 2002, Yang *et al.* [4] found oscillations in the differential resistivity ρ_{xx} of a Hall bar at high filling factors and under high DC current I_{DC}. The experiment was conducted in a 2DEG system in a high mobility ($\mu = 3 \times 10^6$ cm/V s) GaAs/AlGaAs heterostructure at T=0.33 K, up to a current density of ~ 1.2 A/m. The oscillations were observed to displace with increasing DC current, following a period of $B \propto I_{DC}/WM$ linear relationship, where M is an integer representing the N^{th} order of the oscillation maxima, and W is the width of the Hall bar. This relation was found to occur strictly in the derivative of ρ_{xx} with respect to B, where maxima of the oscillations plotted versus B-field and I_{DC} extrapolate to zero. This non-linear phenomenon was attributed to Zener tunneling between Landau levels in a strong electric field.

The following explanation follows Yang *et al.* [4]. In a 2DEG in a Hall bar, with a DC current along the length of the Hall bar and a perpendicular B-field, a Hall electric field E_Y along the width of the Hall bar (y-direction) is induced by the DC current. The resulting Landau levels are tilted spacially in the y-direction due to E_Y, such that:

$$E_N(Y) = (N + \frac{1}{2})\hbar\omega_c - eE_Y Y + \frac{1}{2}m^* v_d^2; \tag{2.1}$$

where v_d is the electron drift velocity, current density is related to v_d by $I_{DC}/W = nev_d$, W is the sample width, n is the electron concentration and N is the Landau level index. Similarly, the Fermi energy level is also tilted along the y-direction [104]. This results in the lifting of degeneracy Landau level with respect to the y-direction, which allows

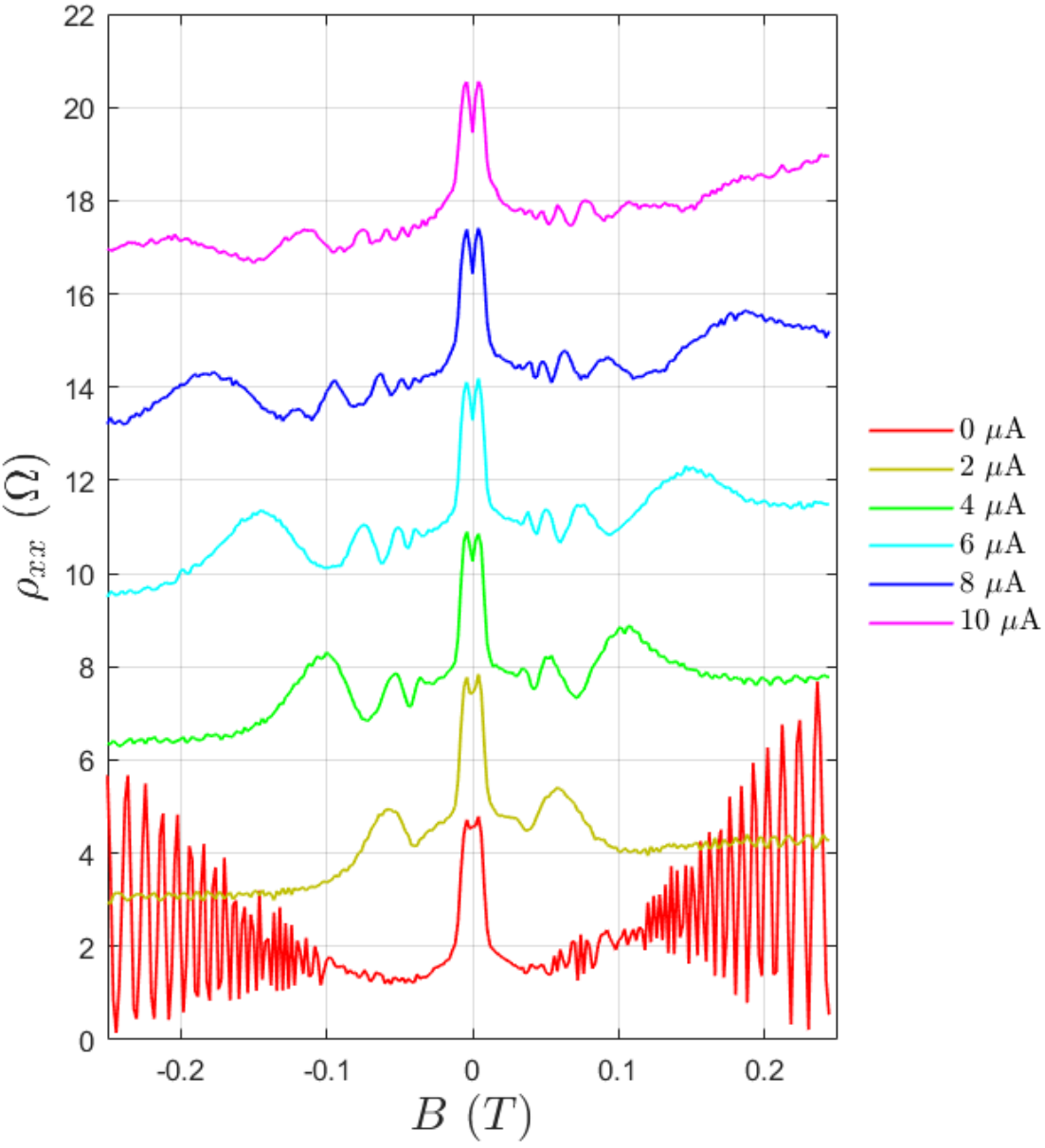

Figure 2.1: Differential resistivity ρ_{xx} versus B-field at different DC current showing HIROs. HIRO harmonics evolve linearly with DC current, and inversely proportional to B-field. At zero current, there is no HIRO, only SdH oscillations. Traces are shift up by 2 Ω for clarity.

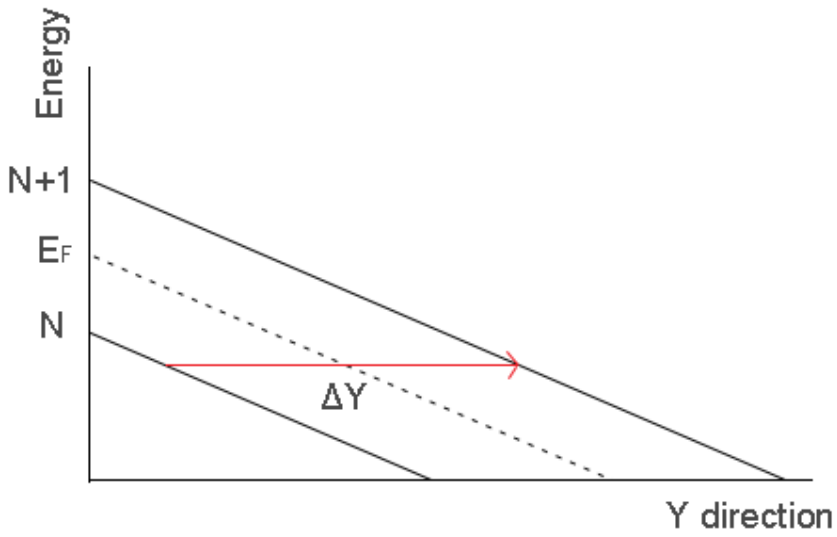

Figure 2.2: Sketch of Landau level transition between spatially tilted Landau levels in a 2DEG under magnetic field and in an electric field. N and $N+1$ refers to the index of Landau levels. The hopping distance ΔY is bounded by energy conservation, and the transition rate is maximized when $\Delta Y \simeq 2r_c$.

for transitions between the occupied Landau levels below the Fermi energy E_F and the empty ones above the E_F. The HIRO correction in the resistivity is minimal when the transition terminates between two Landau levels, and reaches its maximum when the transition terminates at the center of a Landau level. The hopping occurs during elastic short-range scattering with impurities. A hopping along the Y-direction causes a transition between Landau levels (see Fig. 2.2). By conservation of energy, the transition must satisfy $eE_Y\Delta Y = M\hbar\omega_c$, where $eE_Y\Delta Y$ is the work between the two spatially separated Landau levels, $M = N' - N$ is and index difference between involved Landau levels, $\hbar\omega_c$ is the difference between involved Landau levels, and ΔY is the distance between two Landau levels. Simplifying ΔY gives:

$$\Delta Y = \frac{M\hbar\omega_c}{eE_Y} = M\frac{e\hbar nW}{m^* I_{DC}}. \tag{2.2}$$

Scattering depends on the probability of finding an impurity at the overlap of the wave functions of the two Landau level states. The authors found that the transition rate is maximal at $\Delta Y = \gamma r_c$, where $r_c = v_F/\omega_c = m^* v_F/eB$ is the cyclotron radius, and $\gamma \approx 2.0$. γr_c is associated with a momentum transfer of $\approx 2k_F$, where k_F is the Fermi wave vector. When $\Delta Y > 2r_c$, the initial and final electron wave function do not overlap and there is no hopping. The distance $\approx 2r_c$ is the maximal as well as the most optimal distance for overlap of the wave function, which maximizes the hopping probability. By combining this condition with Eq. (2.2), we obtain:

$$\gamma r_c = \frac{M\hbar\omega_c}{eE_Y} \quad \Rightarrow \quad B = \gamma\sqrt{\frac{2\pi}{n}}\frac{m^*}{e^2}\frac{I_{DC}}{MW} \tag{2.3}$$

which is the linear relationship observed in $B \propto I_{DC}/WM$. Yang *et al.* found experimental confirmation of $\gamma \approx 2.0$. In their sample, HIRO oscillations were also observed up to order $M = 4$. For HIROs to be observed, there must be a significant amount of short range scatterers. Three short range elastic scatterers were discussed as possible processes for HIROs: residual background ionized impurities, interface roughness and neutral impurities in the GaAs quantum well. Lastly, unlike SdH oscillations, the oscillations were observed to persist in high temperature ($\sim$4 K).

The observation of HIROs drew significant attention and prompted various experimental [8, 10, 11] and theoretical studies [101–103]. Notably, in the regime of very small applied DC current, an unusual sharp drop in the differential resistivity was observed by J.-Q. Zhang *et al.* [10] and by W. Zhang *et al.* [11]. This effect was attributed to a correction of the electron energy distribution function under DC current [101]. Examples of this phenomenon in our sample are presented in Fig. 2.3. The drop is for I_{DC} smaller than the first order resonance of HIROs. In 2007, to address all the the characteristics of HIROs, namely the I_{DC}/B oscillatory correction to the resistance, HIRO persisting at higher

temperature and the low DC current dip feature, Vavilov *et al.* [102] developed a theory of non-linear response of electronic magnetotransport of a 2DEG with respect to an electric field and in high Landau levels. The authors took a quantitative approach using a standard Boltzmann kinetic formalism for a weakly disordered 2DEG under both electric and magnetic field. This theory describes HIROs by two separate physical mechanisms. The first mechanism is the large-angle scattering off of short-range disorder, which is related to the elastic-impurity scattering previously explained. This mechanism explains the oscillatory behavior of HIROs. The second mechanism is an inelastic contribution that originates from the nonequilibrium correction to the electron distribution function under DC current. At weak fields, this correction causes the suppression of electron transitions normally contributing to the conductivity, which reduces the magnetoresistance. The inelastic mechanism explains the low current correction in the form of a dip in the differential resistivity. Effectively, this theory builds on the mechanism suggested by Yang *et al.* and incorporates other processes to explain the low current correction in the ρ_{xx}. Functionally, by taking a quantitative approach, Vavilov *et al.* found an analytical expression for the correction in the differential resistivity, which can describe both the amplitude and the oscillation frequency in terms of quantum parameters.

Here, we follow Vavilov *et al.* [102] to summarize the relevant equations to use in practice for experimental data. The analytical expression found for the non-linear current density j in the limit of high temperatures $k_B T \geq \hbar\omega_c/2\pi^2$ and magnetic fields $\omega_c\tau_0 \leq 1$ is:

$$j(E) = \sigma_D E\left(1 + 2\lambda^2 F\left(\zeta\right)\right); \quad F(\zeta) = 2\Gamma_1(\zeta, \tau_{in}) + \Gamma_2(\zeta) \tag{2.4}$$

where σ_D is the Drude conductivity, τ_0 is the quantum scattering time, τ_{in} is the inelastic relaxation time, $\lambda = exp(-\pi/\omega_c\tau_q)$ is the Dingle factor, $\zeta = 2\pi e E r_c/\hbar\omega_c$ is the frequency $\propto I_{DC}/B$, equivalent to πM in Eq. (2.3). Effectively, $2\lambda^2 F(\zeta)$ is the correction in the

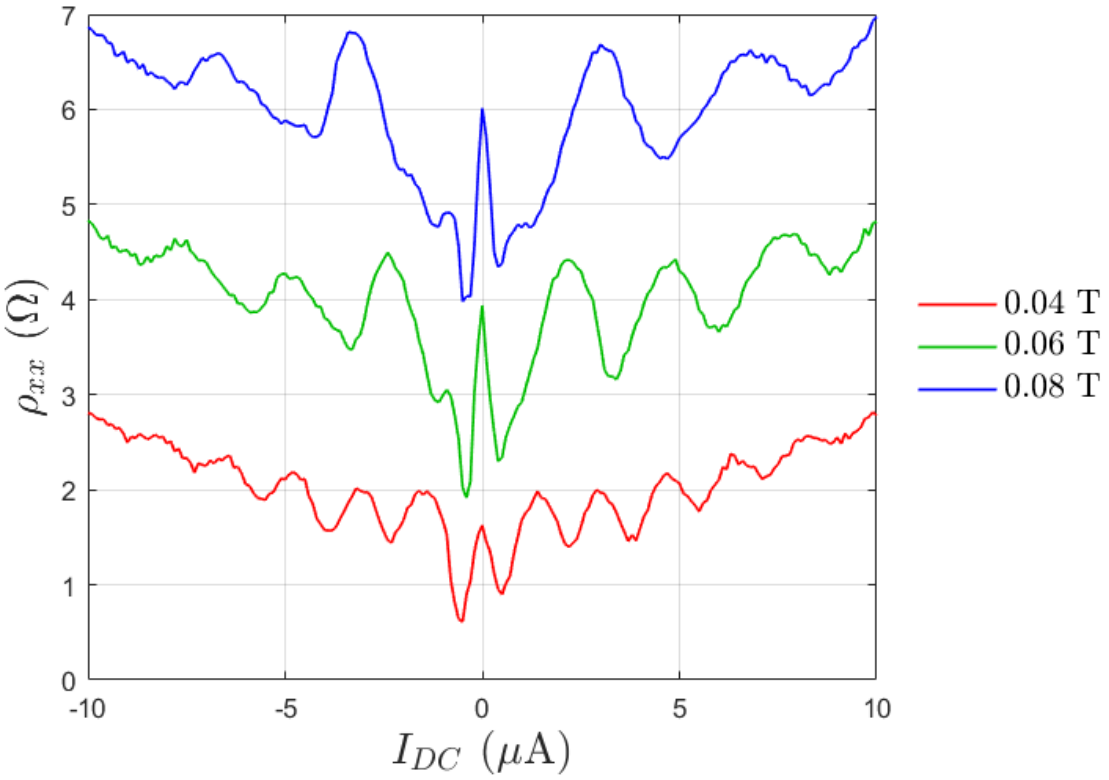

Figure 2.3: ρ_{xx} versus I_{DC} at various fixed B-fields. A sharp drop in the differential resistivity can be observed in the small I_{DC} regime. Traces are shift up by 2 Ω for clarity.

conductivity that describes HIROs. The expression $\Gamma_1(\zeta)$ and $\Gamma_2(\zeta)$ are defined as the following:

$$\frac{\Gamma_1(\zeta, \tau_{in})}{\tau_{tr}} = -\frac{[d\kappa(\zeta)/d\zeta]^2}{\tau_{in}^{-1} + \tau_0^{-1} - \kappa(\zeta)} \tag{2.5}$$

$$\frac{\Gamma_2(\zeta)}{\tau_{tr}} = -\frac{d^2\kappa(\zeta)}{d\zeta^2} \tag{2.6}$$

where τ_{tr} is the transport relaxation time, and $\kappa(\zeta) = \sum_n J_n^2(\zeta)/\tau_n$, $J_n(\zeta)$ are the Bessel functions, $1/\tau_n$ are harmonics of the elastic electron scattering rate. Effectively, this expression can only be fully evaluated given a disorder model for $1/\tau_n$. However, in the

strong-field limit where $\zeta \gg 1$, the authors find

$$\frac{\Gamma_1(\zeta, \tau_{in})}{\tau_{tr}} \propto -\frac{\tau_0}{\tau_\pi^2}\frac{cos^2(\zeta)}{\zeta^2}, \qquad \frac{\Gamma_2(\zeta)}{\tau_{tr}} = \frac{1}{\tau_\pi}\frac{sin(2\zeta)}{\zeta} \tag{2.7}$$

where $1/\tau_\pi = \sum_n e^{i\pi n}/\tau_n$ is the backscattering rate. The Γ_2 contribution is larger than the Γ_1 contribution, which is the source of the oscillations.

To fully evaluate Eq. (2.4), a disorder model was proposed by the authors. In a high-mobility structure, there are two types of disorder. The first type of disorder is from the defects in the quantum well caused by interface roughness and defects in the lattice during growth. Although defects are minimized with a structure growth method like MBE, they are still present. This type of defects causes short range large-angle scattering events [105].

The second type of disorder origins from the remote donors of a quantum well which causes short range small-angle scattering. A quantum well is formed from a doped layer with charge carriers that migrate over to the undoped layer which is the 2DEG. However, the remote donors' electric field can still affect the charge carriers in the quantum well. Usually, in AlGaAs/GaAs hetero-structures, the two layers are separated by a neutral undoped AlGaAs spacer layer, which controls the density of migrating charge charriers, and reduces the effect of the donor region on the electrons in the quantum well. The reduced effect is a disorder that causes small-angle scattering events.

The authors proposed a mixed disorder model that considered both the "smooth" and the "sharp" components of the disorder potential:

$$\frac{1}{\tau_n} = \frac{1}{\tau_{sm}}\frac{1}{1+\chi n^2} + \frac{\delta_{n,0}}{\tau_{sh}}, \quad \chi \ll 1 \tag{2.8}$$

where $1/\tau_{sh}$ is the "sharp" scattering off of impurities inside of a 2DEG and $1/\tau_{sm}$ is the small-angle ($\theta < \sqrt{\chi} \ll 1$) "smooth" scattering off of charged impurities in the proximity of the 2DEG. $\chi \sim (\lambda_F/\xi)$ is related to the the Fermi wavelengthλ_F and ξ is the correlation length of the disorder potential. Given the definition of $\kappa(\zeta)$ and Eq. (2.8), $\kappa(\zeta)$ was obtained to be:

$$\kappa(\zeta) = \frac{J_0^2(\zeta)}{\tau_{sh}} + \frac{1}{\tau_{sm}\sqrt{(1+\chi\zeta^2)}}. \tag{2.9}$$

Note that the transport relaxation time is defined as $\tau_{tr} = \tau_0 - \tau_1$. In Eq. (2.4), $F(\zeta)$ can be separated into two regimes. At weak DC current $\zeta \ll 1$, the term $\Gamma_1(\zeta)$ is the dominant contribution, which describes the decrease of the resistance. At strong DC current $\zeta \gg 1$, the term $\Gamma_2(\zeta)$ dominates and contribute to the oscillatory behavior in the non-linear response.

In experimental studies, HIROs are generally measured in differential resistance. The non-linear correction in differential resistivity ρ becomes:

$$\frac{\delta\rho(j)}{\rho_D} = 2\lambda^2 \frac{d[jF(\pi j/j_B)]}{dj}, \quad j_B = \frac{v_F e^2 B}{4\pi\hbar} \tag{2.10}$$

where $\rho_D = m^*/e^2 n\tau_{tr}$ is the resistivity at zero magnetic field. The full non-linear effect can be directly calculated via Eq. (2.10) for different variables. In Fig. 2.4, we present calculations of Eq. (2.4) versus current for a combination of variables τ_{sh}, τ_{sm}, χ and τ_{in} at fixed $B = 0.05$ T. This theory effectively explains the drastic dip at small DC current and calculates the amplitude of HIROs. One of the findings of the authors is that the HIRO oscillation amplitude in differential resistivity does not decrease with increasing I_{DC} at a fixed B-field. At strong DC current $\zeta \gg 1$, the correction to the differential resistivity is approximately:

$$\frac{\delta\rho(j)}{\rho_D} = \frac{16\tau_{tr}}{\pi\tau_\pi}\lambda^2 cos(2\zeta) \tag{2.11}$$

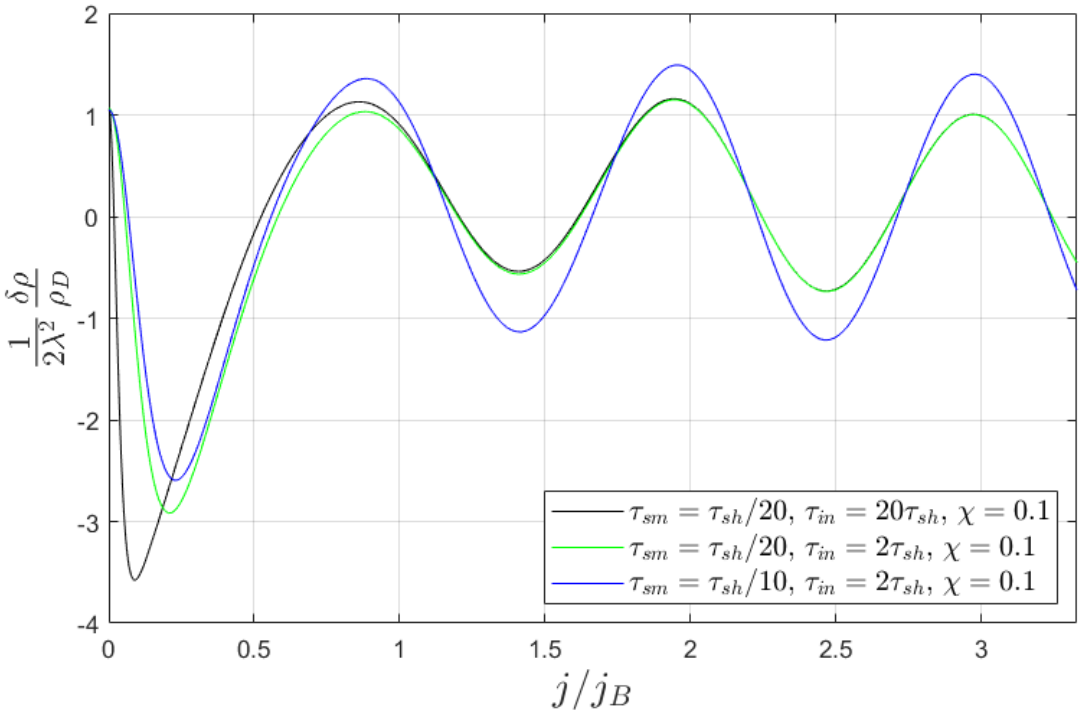

Figure 2.4: Normalized differential resistivity calculated from theory Eq. (2.10) of HIROs versus current density j, for different set of parameters described in the text. This figure is a reproduction of Fig. 3 from Ref. [102], recalculated to extend the current range. At small current, there is a noticeable dip in the resistivity. At higher current, the oscillation amplitude is constant w.r.t. j.

where $1/\tau_\pi$ is the backscattering rate off disorder by scattering angle π. Generally, this equation is the more commonly used in experimental studies to understand HIROs due to its simplicity [14–16,19,20]. However, when the low current range must be considered, the whole theory presented in Equation (2.10) should be used. The theory Eq. (2.11) for HIROs has no thermal damping factor which explains why HIROs were observed to persist at high temperatures unlike SdH oscillations (up to ~ 4 K) [4,8,10]. This theory has also been expanded to include effects under microwave radiation and DC current [103].

2.2 Experimental Studies

An experimental investigation of the HIRO's temperature dependence was performed by Hatke et al. [14], from 2 to 5 K. The authors found a decrease in HIRO amplitude versus increasing temperature. This was explained by a decrease of τ_q versus increasing DC current, where they found a T^2 dependence of $1/\tau_q$ in the form:

$$\frac{1}{\tau_q(T)} = \frac{1}{\tau_q^{im}} + \frac{\lambda T^2}{E_F}, \tag{2.12}$$

where τ_q^{im} is the temperature independent contribution to τ_q and $\lambda \simeq 4.1$. A T^2 dependence was associated to be a signature of electron-electron interaction such that $1/\tau_q = 1/\tau_q^{im} + 1/\tau_q^{ee}$, where $1/\tau_q^{ee}$ is the electron-electron scattering contribution. This was also found to be the case in double quantum wells [106], microwave-induced resistance oscillations [107] and phonon-induced resistance oscillations [108]. The form $1/\tau_q^{ee} = \lambda T^2/E_F$ is consistent with theory equation by Chaplik [109] and Giuliani and Quinn [65].

In terms of oscillation order, HIRO oscillations have been observed up to 10 orders in very high mobility samples [10, 14, 110]. HIRO has also been observed in other materials and other structures. Namely, Dai *et al.* [13] observed HIROs in a two-dimensional hole system in a GaAs/AlGaAs quantum well, which has a higher effective mass ($m^* \approx 0.4m_e$. Bykov *et al.* [17] observed HIROs in a 2DEG in a corbino structure. Shi *et al.* [19] observed HIROs in MgZnO/ZnO heterostructure, which has a much lower mobility ($\mu \sim 10^4$ cm^2/Vs) and a higher effective mass ($m^* \approx 0.3m_e$). The universality of HIROs is useful to extract understand low temperature two-dimensional systems.

In terms of the experimental methods, to better resolve orders of HIROs, examining the differential resistivity ρ_{xx} by performing I_{DC}-sweeps at a fixed B is prefered to per-

forming B-sweeps at a fixed I_{DC} value. Higher orders of HIROs approaches the I_{DC} axis in the phase diagram, which makes it far easier to detect higher orders of HIROs by taking a horizontal fixed B-field trace than a vertical fixed B-field trace [see phase diagram in Fig 1.1(a)]. For analysis, the commonly used approach to extract τ_q is the Dingle plot, which is a plot of the oscillation extrema in a semi-log plot of ρ_{xx} versus $1/B$, where the slope is $\propto \tau_q$. τ_q is extracted for each current value as it has been reported that τ_q can vary with I_{DC} [19]. However, at small I_{DC} ranges, traces versus B-field may show no more than one order of HIRO maxima, which cannot be used in a Dingle plot to extract τ_q. Instead, the method of direct fitting can be used. Contrary to the data collection method, the analysis is more meaningful when applied to ρ_{xx} vs B-field traces at fixed DC current, as quantum parameters could vary with increasing DC current.

3. Experimental Setup

All experimental data of 2DEG presented in this document were obtained from measurements performed on a single Hall bar structure. The 2DEG investigated is in the quantum well (QW) region of a GaAs/AlGaAs hetero-structure grown by molecular beam epitaxy. The 2DEG is located in a 30 nm wide GaAs QW at a depth ∼200 nm below the surface. The QW has barriers on either side composed of $Al_{0.30}Ga_{0.70}As$ and contains QW doping regions. The method of growth and the specific layers are presented in Appendix A. The effective mass of an electron in the 2DEG is $0.067m_e$ where m_e is the electron mass. From a large area Van der Pauw device measured in a dilution refrigerator at base temperature and after illumination, the mobility μ was measured to be 20×10^6 cm^2/V s, equivalent to a mean free path l_{mfp} of 145 μm. The 2DEG electron density n was measured to be 2.0×10^{11} cm^{-2}. The corresponding Fermi velocity and Fermi energy E_F respectively are 1.9×10^7 cm/s and 7.2 meV. A summary of the 2DEG parameters are presented in Table 3.1.

The central region of the Hall bar structure used to acquire all electronic transport data is presented in Fig. 3.1. The Hall bar device is made by standard fabrication techniques where the geometry is lithographically defined and etched from a larger quantum well sample. The Hall bar has nominal width 15 μm, which was chosen such that the Hall bar's width is much smaller than the mean free path. Three pairs of potential probes separated

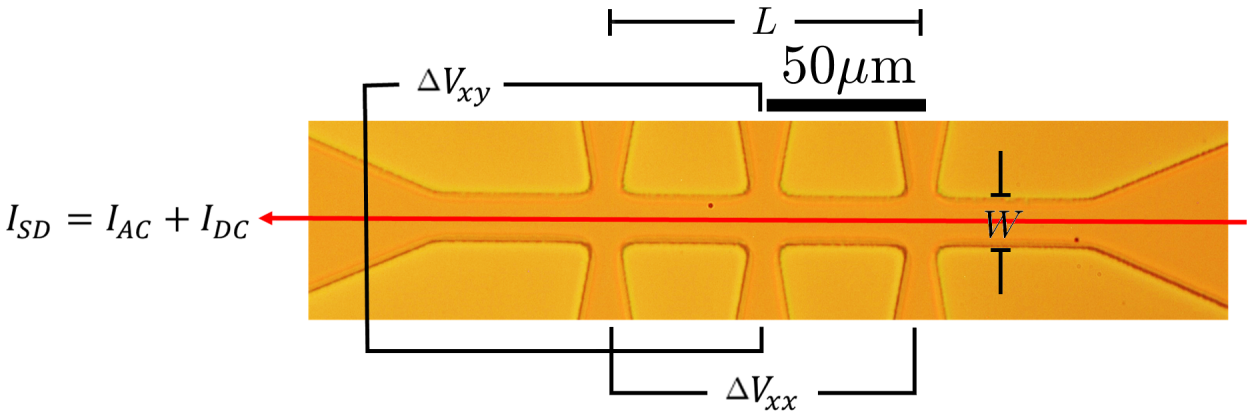

Figure 3.1: Central region of the Hall bar device used for the measurements presented in this thesis. V_{xx} is measured from the bottom left and right voltage probes, separated by a distance L=100 μm, and V_{xy} is measured from the middle top and bottom voltage probes. The lithographic width of the Hall bar is W=15 μm.

by 50 μm were placed along the Hall bar. ΔV_{xx}, the voltage drop along the Hall bar, is measured from the bottom left and right voltage probes, separated by a length of 100 μm, which is referred to as the length L of the Hall bar. ΔV_{xy}, the voltage drop across the Hall bar, is measured from the middle top and bottom voltage probes, as indicated in Fig. 3.1. A DC current combined with a small AC current of 20 nA is passed through the Hall bar from the source to the drain Ohmic contacts. ΔV_{xx} and ΔV_{xy} are measured using standard lock-in technique [33] at 148 Hz. The data obtained from the potential probes are differential resistances, where $r_{xx} = \Delta V_{xx}/I_{AC} = dV_{xx}/dI$ and $r_{xy} = \Delta V_{xy}/I_{AC} = dV_{xy}/dI$. The Hall resistance is presented in Sec. 7.9 of the electron hydrodynamic transport chapter.

The device is maintained in the dark in a dilution refrigerator at base temperature where the mixing chamber temperature is ∼15 mK, where measurements were performed with a B-field applied out of plane. The electron temperature T_e is estimated to be ∼40 mK. Measurements were obtained with a DC current up to 10 μA and a B-field up to 0.25 T.

L	W	n	μ	v_F	E_F	l_{mfp}
(μm)	(μm)	(cm^{-2})	(cm^2/V s)	(cm/s)	(meV)	(μm)
100	15	2.0×10^{11}	20×10^6	1.9×10^7	7.2	145

Table 3.1: Key parameters of the Hall bar and the 2DEG material system. The parameters given are determined from a large area Van der Pauw device measured in a dilution refrigerator at base temperature and after illumination.

Note that the 2DEGs were grown at Princeton University, and the measurements were made in collaboration with the National Research Council Canada, in which I did not participate. My contribution to the research project is focused on the analysis of the experimental data.

Part II

Analysis of Experimental Data

4. Hall-Field Induced Resistance Oscillations

Sharp HIRO resonances can be observed in the phase diagram presented in Fig. 1.1(a). We observe up to 7 HIRO orders from the phase diagram. In this chapter, we compare the experimental data to the theory presented in Sec. 2.1, and extract relevant parameters of interest, namely the quantum lifetime, the backscattering lifetime, the effective width and the inelastic relaxation lifetime. We also detail our observation of a novel "fractional" HIRO-like feature between the $M = 1$ and $M = 2$ HIRO maxima [see black arrows in the phase diagram in Fig. 1.1(a)].

4.1 I_{DC}/B Dependence

We start by analyzing the experimental HIRO data with the model by Yang *et al.* [4]. In their model, the position of the maxima of HIROs in $\partial\rho_{xx}/\partial|B|$, the derivative of the differential resistivity ρ_{xx} with respect to B-field and DC current, satisfies $B \propto I_{DC}/W$. In Fig. 4.1(a), we plot the B-field versus I_{DC} position of maxima of HIRO $\partial\rho_{xx}/\partial|B|$ for each HIRO order M. The position of the maxima can be collapsed onto a single line, essentially that of the first-order HIRO peak, following the relation $B \cdot M \propto I_{DC}/W$. The slope of the

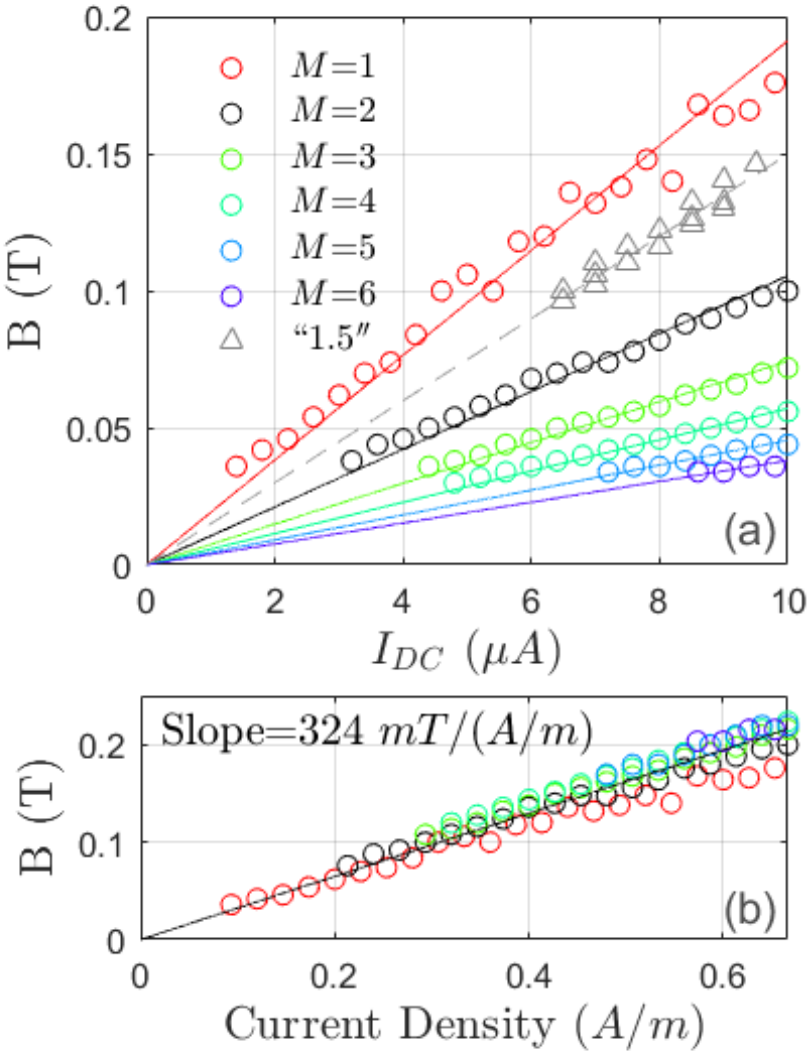

Figure 4.1: (a) Fan diagram of HIRO maxima in $\partial\rho_{xx}/\partial|B|$ for each peak up to the sixth order. Triangles: Maxima in $\partial\rho_{xx}/\partial|B|$ of the "1.5" features. Fitting through points yields M=1.44. (b) HIRO maxima collapsed on a single line by multiplying each maxima by the HIRO peak order M. The slope is used to extract γ. See more details in the text.

single line in Fig. 4.1(b) is found to be 324 mT/(A/m). From Eq. (2.3), we can calculate $\gamma = 2.4$. This result is consistent with the theoretical value of $\gamma \approx 2.0$ reported in the work of Yang *et al.* [4], and their experimental γ values for Hall bars with a 2DEG density close to that for our Hall bar device. It is to note that we used $W = 15$ μm, the physical width of the sample, to calculate the current density. In the next section, we obtained an effective width of the Hall bar W_{eff} equal to 11 μm. Had we used $W_{eff} \sim 11\mu$m to calculate the nominal current density, we would obtain γ=2.1.

4.2 Quantum Parameters Extracted from HIROs

After analyzing the HIRO frequency, we now proceeds to analyze the HIRO amplitude with the model by Vavilov *et al.* [102]. Given the possibility for quantum parameters to vary with increasing DC current, we perform fitting to B-field traces using the model described in Eq. (2.11). From Eq. (2.11), the amplitude of the HIROs depends on the backscattering lifetime τ_π and the quantum lifetime τ_q. The HIRO frequency depends on the effective mass of the electron, electron concentration n and width of the sample W, where W is a fitting parameter. Effectively, we obtain $\tau_\pi \sim 5$ ns, τ_q ranging from 18 to 40 ns decreasing with DC current, and an effective width $W_{eff} = 11$ μm of the Hall bar.

We now discuss the details of the fitting method. The HIRO frequency depends on the effective mass of the electron, electron concentration n and width of the sample W. The effective mass and electron concentration are well-known quantities extracted from SdH oscillations and Hall resistivity, respectively. Therefore, rather than assuming W is fixed and equal to the nominal lithographic width of the Hall bar, W is a fitting parameter, which we refer to as W_{eff}, the effective width extracted from HIROs. We fit individual ρ_{xx} versus B traces to Eq. (2.11) for each value of I_{DC} to obtain τ_q, W_{eff} and τ_π. Furthermore, we choose to fit the $\partial\rho_{xx}/\partial B$ [see Fig. 4.2(a)], the partial derivative of Eq. (2.11) with

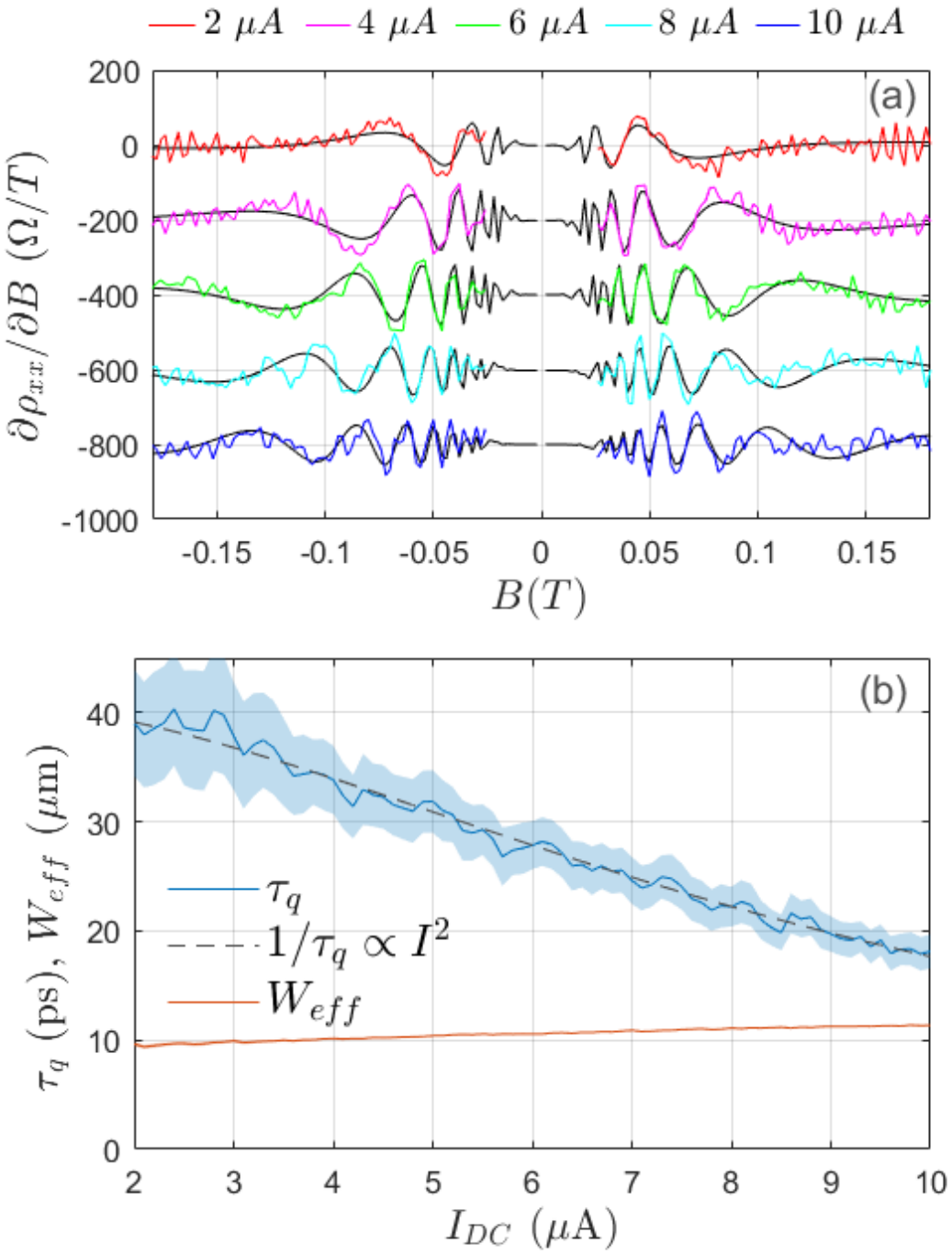

Figure 4.2: (a) HIRO amplitudes in $\partial\rho_{xx}/\partial|B|$ vs B-field (colored lines) fitted to theory Eq. (2.11) (black lines), for different DC current. Curves are shifted downwards by 200 Ω/T. (b) Parameters τ_q and W_{eff} versus I_{DC} extracted from fits. Dashed line: $1/\tau_q$ is proportional to I_{DC}^2, a relation previously reported by Shi *et al.* [19].

respect to B, instead of ρ_{xx}, to remove the background linear B dependence in the data, and to reduce fitting errors, although fits to either are equivalent and give nearly identical fitting parameters. The fitting parameters τ_q and W_{eff} obtained are presented in Fig. 4.2(b). τ_q is discussed extensively in the following paragraph. The value of the effective electronic width, W_{eff}, is found to be ~ 11 μm over the 10 μA current range. Parameter W_{eff} is obtained from the HIRO frequency and is extremely accurate as it is independent of the amplitude of the HIROs. The effective electronic width is smaller than the lithographic width of the Hall bar of 15 μm. We attribute the difference to a combination of undercut during the wet etching step in the fabrication of the Hall bar, and sidewall depletion. For the backscattering lifetime τ_π, we obtained $\tau_\pi \approx 5$ ns with no significant current dependence.

The extracted values of the quantum lifetime τ_q in Fig. 4.2(b) are notable for two reasons. First, τ_q decreases with increasing DC current, and second, τ_q extracted from the HIROs far exceeds the value of τ_q=11.5 ps extracted from the SdH oscillations in Sec 5.1. Concerning the first point, in model of Vavilov *et al.* [102], the HIROs amplitude should not depend on DC current, whereas our data shows that the HIROs amplitude decreases with increasing DC current (see Fig. 2.3). This has also been observed in another experiment featuring MgZnO/ZnO [19], and was attributed to enhanced electron-electron scattering with increasing electron temperature, where $1/\tau_q \propto I_{DC}^2$. Using the same analysis for our Hall bar, we obtain

$$\frac{\tau_q(I_{DC})}{\tau_q(0)} = 1 + \left(\frac{I_{DC}}{I_0}\right)^2 \tag{4.1}$$

where $\tau_q(0)$=41.2 ± 0.7 ps and I_0=8.66 ± 0.04 μA [see Fig. 4.2(b)]. Note that we used the strong field ($\zeta \gg 1$) approximation of the theory equation by Vavilov *et al.*, which may

not accurately reflect the theory for the HIRO correction below the first HIRO order. To offset this issue, we only performed fitting for traces above 2 μA.

Concerning the difference between τ_q and τ_q^{HIRO}, the extracted value of τ_q from fitting HIROs, τ_q^{HIRO} varies from $\sim$40 ps at 2 μA to $\sim$18 ps at 10 μA. On the other hand, τ_q^{SdH}, the extracted value of τ_q from fitting the SdH oscillations at zero DC current, is $\sim$11 ps. The extrapolated value to zero DC current of τ_q^{HIRO} is 41.2 ps, which is almost 4 times τ_q extracted from SdH oscillations. An alternate method to extract τ_q from HIROs is to use an Arrhenius plot, which is to plot the logarithm of HIRO extrema as a function of inverse B-field as shown in Fig. 4.3. From Eq. (2.11), the slope is equal to $-2\pi m^*/e\tau_q^{HIRO}$. At $I_DC = 5$ μA, we obtain $\tau_q^{HIRO} = 29$ ps, which is consistent with the direct fitting methodology. For our data, the Arrhenius method is only effective for $I_{DC} > 4$ μA, where there are enough oscillation extrema, and for $I_{DC} < 7$ μA, before the fractional HIRO feature which correlates with a decrease in amplitude from the nearby extrema (described in Sec. 4.4). In Fig. 4.3, we also plot the SdH oscillation extrema. The Dingle factor in HIRO Eq. (2.11) is squared, therefore the slope of HIRO extrema in an Arrhenius plot should be twice that of SdH extrema. However, this is clearly not the case as can be seen in Fig. 4.3. For the 5 μA data, the slope for the HIROs is in fact even less than the slope for the SdH oscillations, and illustrates well why we obtain a value for τ_q^{HIRO} that is a factor of two to four times larger than the value for τ_q^{SdH}. Looking closer at the theory, which assumes that τ_q for HIROs and SdH oscillations are the same, we recall that in the derivation of Eq. (2.4) it is also assumed that $k_BT \gg \hbar\omega_c$. This corresponds to a temperature exceeding 0.5 K at 0.025 T, which clearly does not hold for our experimental situation. This may explain the observed discrepancy between τ_q^{SdH} and τ_q^{HIRO}, and suggests that a theory for HIROs extended to the low temperature regime is needed in order to correctly explain the observed amplitudes of the HIROs. Usually, the quantum lifetime is normally taken to

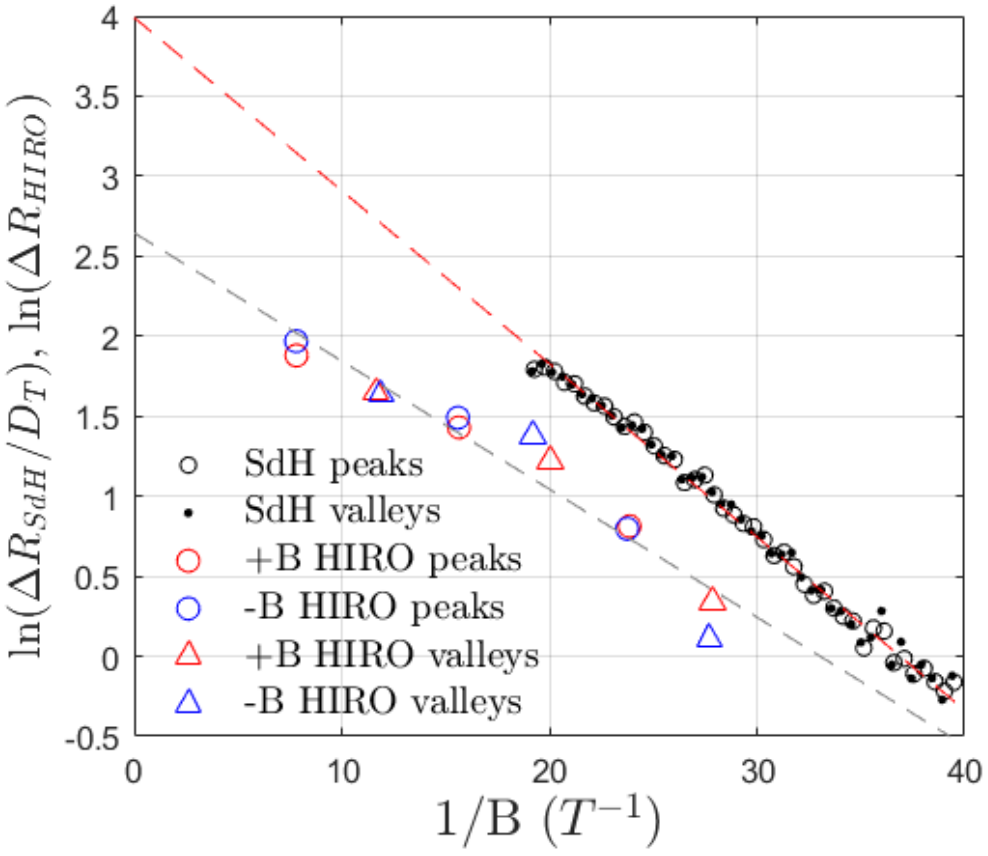

Figure 4.3: Arrhenius plot versus $1/B$ of SdH oscillations extrema amplitudes (at I_{DC} = 0 μA) and HIRO extrema amplitudes at I_{DC}=5 μA, in R_{xx}. Red dashed line for SdH oscillations: fit to Eq. (1.2) where D_T is the thermal damping factor, and τ_q^{SdH} is determined from the slope (τ_q^{SdH}=11 ps). The intercept is $ln(4R_0)$. Grey dashed line for HIROs: fit to Eq. (2.11) where τ_q^{HIRO} at 5 μA is determined from the slope (τ_q^{HIRO}=29 ps). The intercept is $ln(R_\pi)$=$ln(\frac{L}{W}\frac{16m}{\pi ne^2\tau_\pi})$.

be a value determined from the SdH oscillations (τ_q^{SdH}) at zero DC current. Inferring this quantum lifetime is the same as the quantum lifetime determined from measurement of HIROs (τ_q^{HIRO}), a non-linear transport phenomenon observed at finite DC current, therefore has to be done with caution [20]. The difference could also be explained by noting that the τ_q^{SdH} are sensitive to macroscopic density fluctuations, and τ_q^{HIRO} is not, which results in smaller values of τ_q^{SdH} compared to τ_q^{HIRO} in the same sample [14, 111].

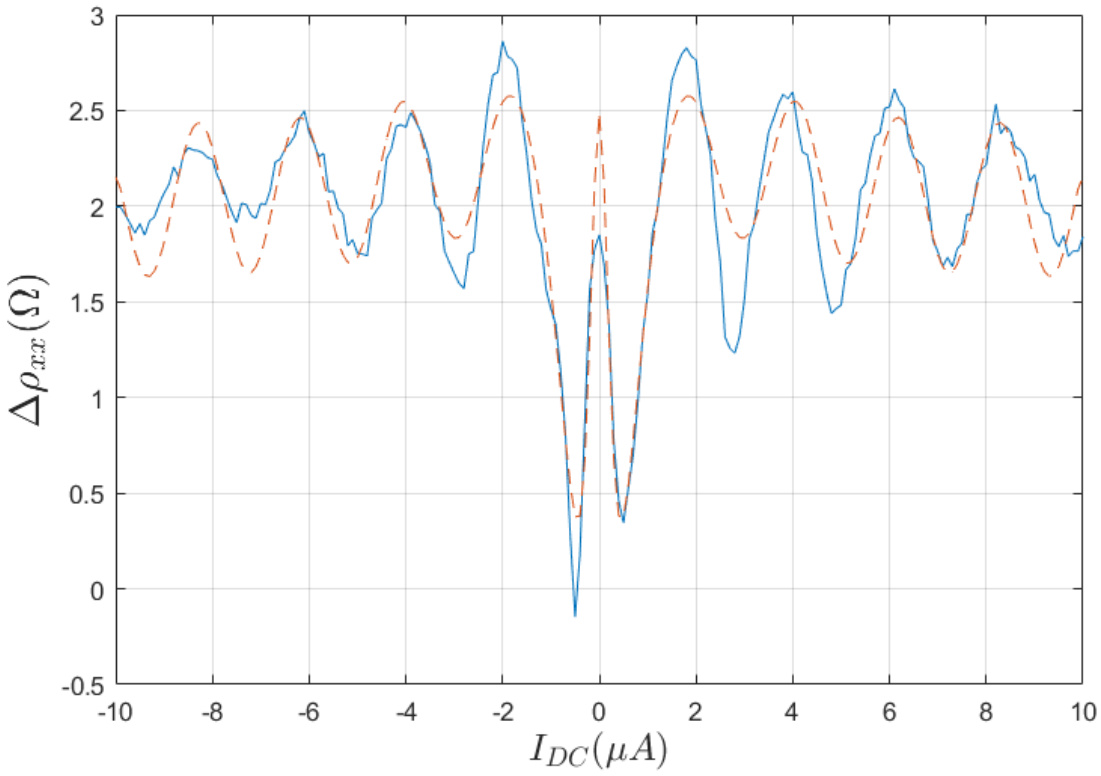

Figure 4.4: HIROs amplitude $\Delta\rho_{xx}$ at B=0.06T plotted versus I_{DC}, experimental data (solid line, with background parabolic dependence removed) compared to theory (dashed line). The dip at small I_{DC} ($I_{DC} \sim 1\mu$A) agrees with the theoretical model by Vavilov *et al.* [102]. However, the experimental data shows decreasing amplitude of HIROs with increasing DC current, which is not in agreement with the theory.

4.3 Small DC Current Dip

At small DC current ($I_{DC} < 1\ \mu$A), we observe a drastic dip in the ρ_{xx} at non-zero B-field, a characteristic of HIROs previously observed in Refs. [10,11]. This non-linear phenomenon is described theoretically in Eq. (2.10) by Vavilov *et al.* [102] in Sec. 2.1. In Fig. 4.4, we present the ρ_{xx} versus I_{DC} trace at B=0.06 T and the fit of Eq. (2.10) to the data. In the process of fitting, we considered the mixed disorder model presented in Eq. (2.8). We obtain parameters $\chi = 0.1$, $\tau_{sh} = 289$ ps, $\tau_{sm} = 13$ ps and $\tau_{in} = 580$ ps. We recall that $1/\tau_{sh}$

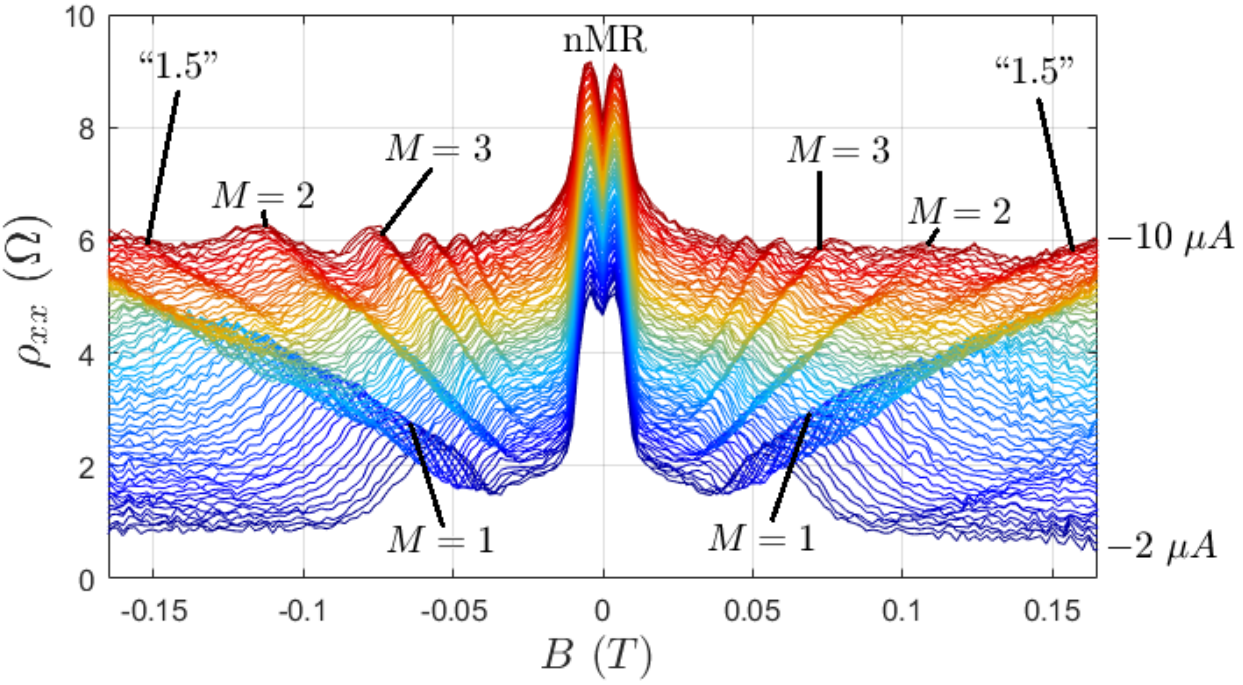

Figure 4.5: Differential resistivity ρ_{xx} versus B-field traces for a range of I_{DC} values offset from each other by 0.06 Ω, starting from the I_{DC}=-1μA trace. The "1.5" feature can be observed around $|B|$=0.12 T.

is the scattering off of impurities inside of a 2DEG, $1/\tau_{sm}$ is the small-angle scattering off of charged impurities in the proximity of the 2DEG, χ is related to the scattering angle for τ_{sm}, and τ_{in} is the inelastic relaxation time.

4.4 Fractional HIROs

Lastly, we report on a "fractional" HIRO-like feature observed between the $M = 1$ order and $M = 2$ order of HIROs observed in the phase diagram. This phenomenon, which we refer to as the "1.5" feature, can be observed in three of the four quadrants in Fig. 1.1(a) for a DC current exceeding 6 μA and a B-field above 0.1 T (see Fig. 4.5). The positions of the maxima of the "1.5" feature in the I_{DC} vs B-field plane are plotted in Fig. 4.1. Specifically, we find that the "1.5" feature at M=1.44$\pm$0.04.

In terms of amplitude, we observe a decrease in amplitude of the $M = 1$ and $M = 2$ HIRO maxima coinciding with the onset of the "1.5" feature. In Fig. 4.6, we present ρ_{xx} versus I_{DC} for each HIRO order M, where the B-field is parameterized as a linear function of I_{DC} following Fig. 4.1(b). We selected the negative B-field and negative I_{DC} quadrant of the phase diagram, where the "1.5" feature is most prominent. At $M = 1.44$, an increase in ρ_{xx} can be observed around -7 μA. Around $I_{DC} = -7$ μA, a drop in the amplitude of both $M = 1$ and $M = 2$ HIRO maxima is observed. The origin of the "1.5" feature is currently unknown. We speculate that it may be related to the lifting of the spin degeneracy which is observed in the Hall bar measured in the SdH oscillations at a similar B-field ($\sim$ 0.15 T). "Fractional" HIROs have been been observed previous by Hatke *et al* [110], where a HIRO-like feature was reported at $M = 0.5$. However, in their case, the feature was observed under microwave illumination, which is a different regime than what we observed.

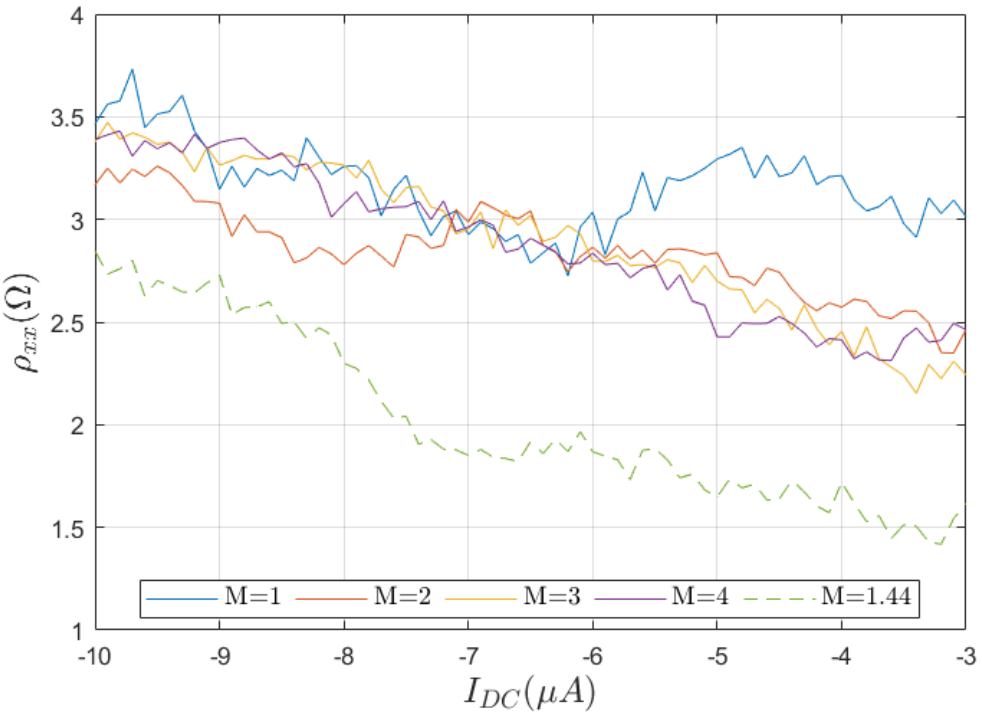

Figure 4.6: Differential resistivity ρ_{xx} at HIRO maxima in the $-$B-field and $-I_{DC}$ quadrant of the phase diagram in Fig. 1.1, extracted by peak order M and plotted versus I_{DC}. Dashed line: ρ_{xx} near the HIRO minima at $M = 1.5$ (specifically at M=1.44, following 4.1). Around I_{DC} $\sim$-6 μA, the M=1 and M=2 HIRO maxima amplitudes decrease, and coincide with the onset of the "1.5" feature.

5. Shubnikov-de Haas Oscillations

SdH oscillations are most clearly observed at zero DC current. We begin by presenting a SdH oscillation trace at zero DC current and with an AC current of 40 nA in Fig. 5.1. At $\omega_c\tau_q > 1$ (or $B > B_q$), SdH oscillations are clearly visible. In this section, we compare the SdH oscillation to theory Eq. (1.2) to extract parameters τ_q and R_0. Recall R_0 is the zero

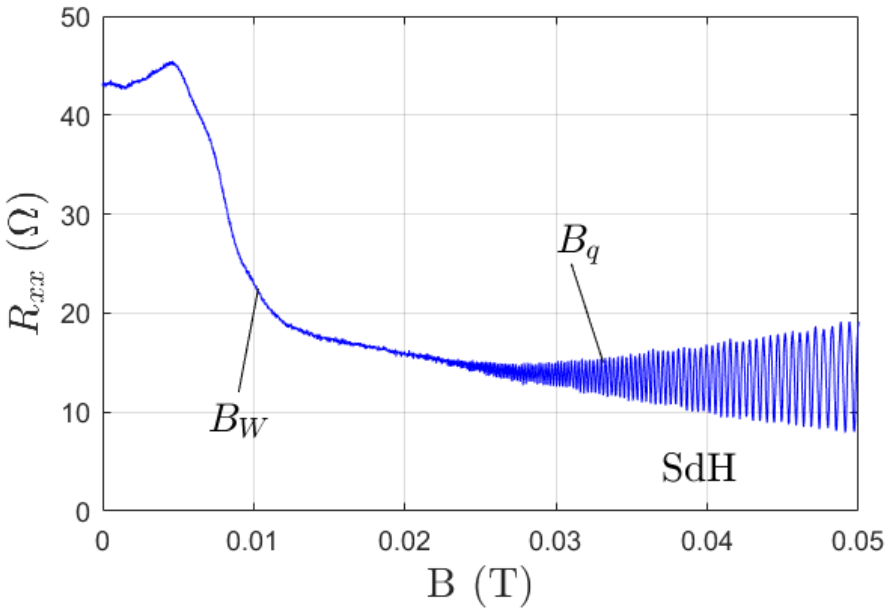

Figure 5.1: Resistivity R_{xx} versus B-field at I_{DC}=0 μA and AC current equal to 40 nA. Near B=0 T, there is a negative magnetoresistance, bounded by a sudden change in slope at B_W=2r_c. SdH oscillations become significant for $B > B_q$, where B_q is related to τ_q.

B-field resistance. However, in the case of our sample, at zero B-field, a nMR alters the zero B-field resistance. We aim to detect whether nMR is related to SdH oscillations.

5.1 Extraction of τ_q and R_0

Our first method of fitting is the direct fit of Eq. (1.2) to the oscillations. This method has the advantage of considering all experimental data points instead of only the peaks, which offers greater accuracy for the parameters. We obtain R_0=$11.4 \pm 0.6\ \Omega$, τ_q=11.5 ± 0.3 ps. A useful conversion of B-field is the filling factor of Landau levels, which is equal to $\nu = 2E_F/\hbar\omega_c = 2\pi\hbar n/eB$. SdH oscillations are extracted from the resistance trace and plotted over ν. Figure 5.2 presents the SdH oscillation (in black) and the fit (in red). The value of R_0 is four times smaller than the zero field resistance. The bulk resistance calculated from $1/\rho = en\mu$ is equal to 14 Ω. The electron concentration $n = 2.0 \times 10^{11}$ cm^{-2} and mobility $\mu = 20 \times 10^6$ cm^2/V s were obtained from a Van der Pauw sample. We conclude that the value of R_0 is not related to the nMR phase.

Alternatively, we can extract R_0 and τ_q from a Dingle plot, which is the more common way to obtain τ_q. The method is as follows: extract the SdH oscillation amplitude extrema; take the natural logarithmic of each extrema divided by D_T from Eq. (1.3) and plot against 1/B; perform a linear fit. Essentially, the amplitude of Eq. (1.2) is transformed into:

$$log(\frac{\Delta R_{xx}}{D_T}) = log(4R_0) - \frac{\pi m^*}{e\tau_q}\frac{1}{B}, \tag{5.1}$$

where the intercept is a function of R_0 and the slope is a function of τ_q. From fitting the data, we obtain R_0=$13.5 \pm 0.6\ \Omega$, τ_q=11.0 ± 0.2, which are consistent with the values obtained from direct fitting. The advantage of this method is the ability to separate R_0 and τ_q accurately. The disadvantage of this method is the possible under-fitting when

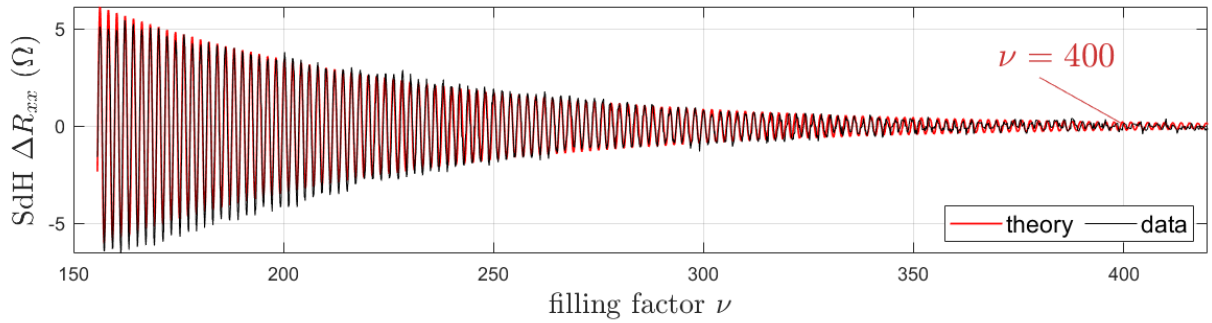

Figure 5.2: SdH oscillations amplitude ΔR_{xx} at I_{DC}=0 μA and AC current equal to 40 nA plotted versus filling factor ($\nu \propto 1/B$), theory (red line) fitted to experimental data (black line). We obtain parameters R_0=11.4 $\pm$ 0.6 Ω, τ_q=11.5 $\pm$ 0.3 ps. SdH oscillations are observable up to ν=400 (B=21 mT).

considering only the SdH oscillation extrema; i.e. the data may not have captured the true resistance and B-field of a maxima, and only a near peak value. This may explain the slight difference in parameter R_0 obtained from the two different methods.

5.2 Phase Inversion

In the phase diagram presented in Fig. 1.1(a), SdH oscillations persist at non-zero DC current. Their amplitude decreases rapidly with increasing I_{DC}, and a phase inversion occurs around $I_{DC} \sim 0.3$ μA. The low I_{DC} positive B-field phase diagram is presented in Fig. 5.3(a). Assuming the electron temperature T_e changes with DC current, we can use to theoretical model presented in Sec. 1.3 to fit our data. Although we do not have an experimental relation for I_{DC} vs T_e, it is possible to extract a relation from fitting and compare to results from previous work.

Recall from Sec. 1.3 that the theory model of phase inversion in differential resistance r_{xx} is

$$r_{xx} = \frac{\partial V_{xx}}{\partial I} = R_{xx} + I_{DC} \frac{\partial \Delta R_{xx}^{SdH}}{\partial T_e} \frac{\partial T_e}{\partial I}, \tag{5.2}$$

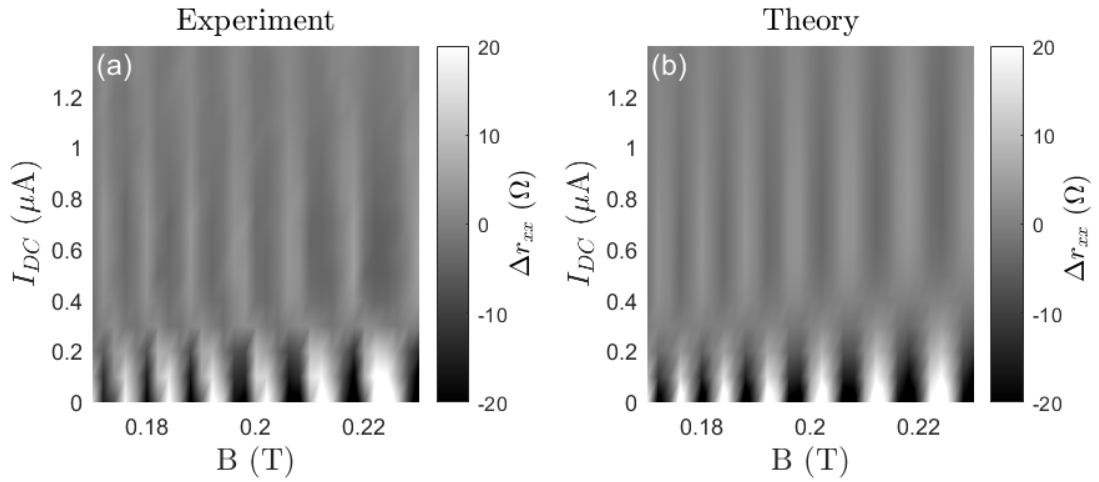

Figure 5.3: Grayscale plots showing phase inversion of SdH oscillation amplitude Δr_{xx} in differential resistance vs B and I_{DC}, experimental data (a) compared to theory (b). The phase inversion occurs at $\sim$0.3 μA around B=0.2 T.

where T_e is the electron temperature. Fitting the theory to the experimental data is non-trivial, due to the nature of Eq. (5.2). Given an unknown function $T_e(I_{DC})$, Eq. (5.2) is a differential equation with temperature T_e and its derivative w.r.t. $\partial T_e/\partial I_{DC}$, which cannot be readily used to fit the experimental data. A solution is to assume the electron temperature is of form $T_e = T_0 + \alpha I_{DC}^{\beta}$ as presented in Eq. (1.5). This relation was obtained from a similar experimental work by Studenikin *et al.* [33]. $T_0 = 15$ mK is the bath temperature in our experimental setup. We use a brute force Monte Carlo approach to find parameters α and β. The method of fitting is as follows: 1. Choose a pair of values for α and β (starting order of values are taken from relation in Studenikin *et al.* [33]); 2. Compute T_e for all traces by I_{DC}. 3. Find curve of best fit by comparing Eq. (5.2) to data using dT_e/dI_{DC} as a fitting parameter. 4. Compare $dT_e/dI_{DC}(I_{DC})$ obtained from fitting to the empirical $(dT_e/dI_{DC})_{theory}$ obtained from the pre-selected values of α and β. 5. Repeat 1 to 4 for a range of α and β to find the pair of parameters where dT_e/dI_{DC} self-consistently matches best with $(dT_e/dI_{DC})_{theory}$.

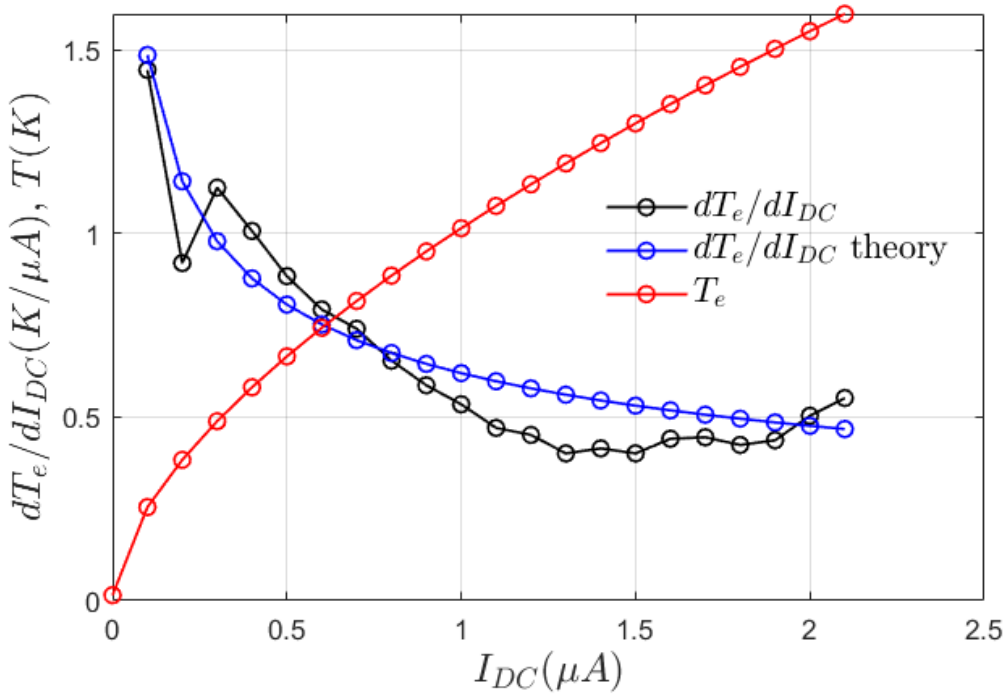

Figure 5.4: Electron temperature T_e and $\partial T/\partial I$ plotted versus I_{DC}. theory and from fitting. A current dependence is extracted for the electron temperature $T_e(I_{DC})$=T_0 + $\alpha(I_{dc})^{\beta}$=T_0+$1.0(I_{dc})^{0.62}$, where T_0=0.015 K is the bath temperature and I_{DC} is in μA. $\partial T/\partial I$ from fit matches the theory, which is the self-consistency condition for the Monte Carlo simulation to find the values for α and β.

Using the method outlined above, we obtain $T_e = T_0 + 1.0I_{DC}^{0.62}$ for our data. The fitting parameter dT_e/dI_{DC} self-consistently matches with dT_e/dI_{DC} theory obtained from $\alpha = 1.0$ and $\beta = 0.62$ (see Fig. 1.5). We find β=0.62 consistent with the value of $\beta = 2/3$ reported in previous work by Studenikin *et al.* [22], further suggesting electron heating is important for phase inversion. The theoretical phase diagram of phase inversion is presented in Fig. 5.3(b), which matches the experimental data.

6. Negative Magnetoresistance at Zero Magnetic Field

6.1 Origin of Negative Magnetoresistance

In the phase diagram presented in Fig. 1.1(a), a strong negative magnetoresistance can be observed around zero magnetic field. The sudden change in slope and the double peak feature are both signs of ballistic transport of electrons in a 2DEG [36], which is presented in Fig. 6.1. The magnetoresistance persists at non-zero DC current. However, after removing the background parabolic increase in the resistance with I_{DC}, as presented in Fig. 7.5(b), we observe a decrease in the amplitude of the magnetoresistance.

6.2 Double Peak

We now focus on the topic of double peaks, which we observe on top of the negative magnetoresistance in ρ_{xx} [see Fig. 6.2(a)]. For our Hall bar device, we infer $W_{eff} \simeq 0.65 r_c$, using W_{eff} = 11 μm, from the position of the two peaks in the double-peak feature at $I_{DC} = 0$ (B = 4.6 mT and B = -4.8 mT), presented in Fig. 6.1. Note that a double-peak

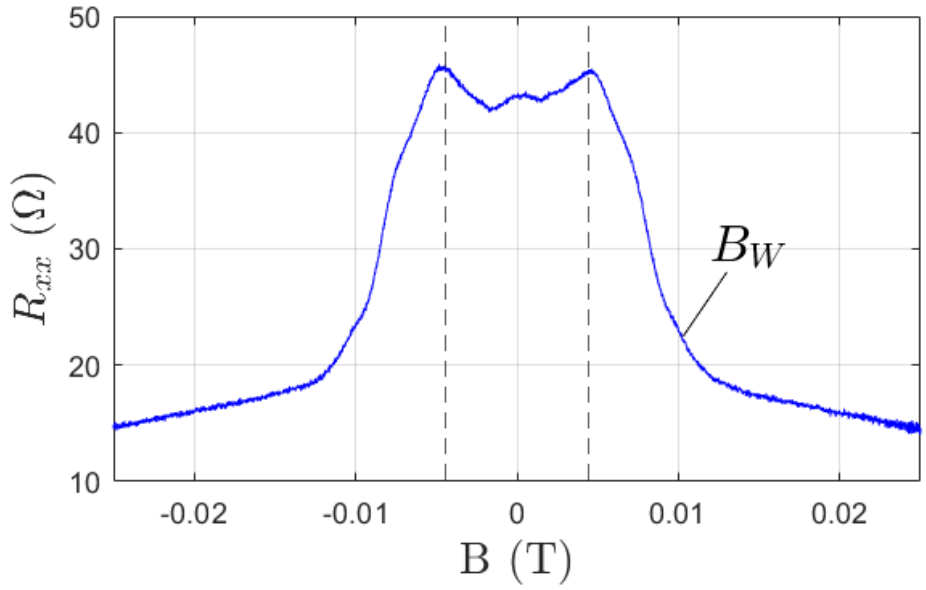

Figure 6.1: Resistivity R_{xx} versus B-field at I_{DC}=0 μA and AC current equal to 40 nA. Near B=0 T, there is a negative magnetoresistance, bounded by a sudden change in slope at B_W=2r_c. Dashed lines: the double peak of the nMR feature can be identified at W_{eff} $\simeq$0.65r_c.

is more prominent with diffuse scattering on the edge along the Hall bar channel [40], which would need to be taken into account in numerical simulations.

From the phase diagram in Fig. 6.2(a), we also observe that the double peak separation increases with DC current. The $+B$ and $-B$ peak positions are presented in Fig. 6.2(b), and were extracted with Gaussian peak fitting. The parabolic behavior of the double peak position can be fitted to $(B_{dp} - B_{dp}(0))/B_{dp} = (I_{dp}/I_{dp,0})^2$ (after averaging both $+B$ and $-B$ positions), where we obtain $B_{dp}(0)$ = 4.5 mT and $I_{dp,0}$ = 0.27 μA [see Fig. 6.2(c)]. At I_{DC} = 0, the double peak is a sign of ballistic transport, with $W_{eff} \simeq 0.55r_c$. If we assume $W_{eff} \simeq 0.55r_c$ for $I_{DC} > 0$, we would obtain a W_{eff} that decreases with increasing DC current. However, from HIROs analysis in Sec. 4.2, we obtained the electronic width W_{eff} w.r.t. I_{DC} in Fig. 4.2(b), which slightly increases with I_{DC}. Thus, we

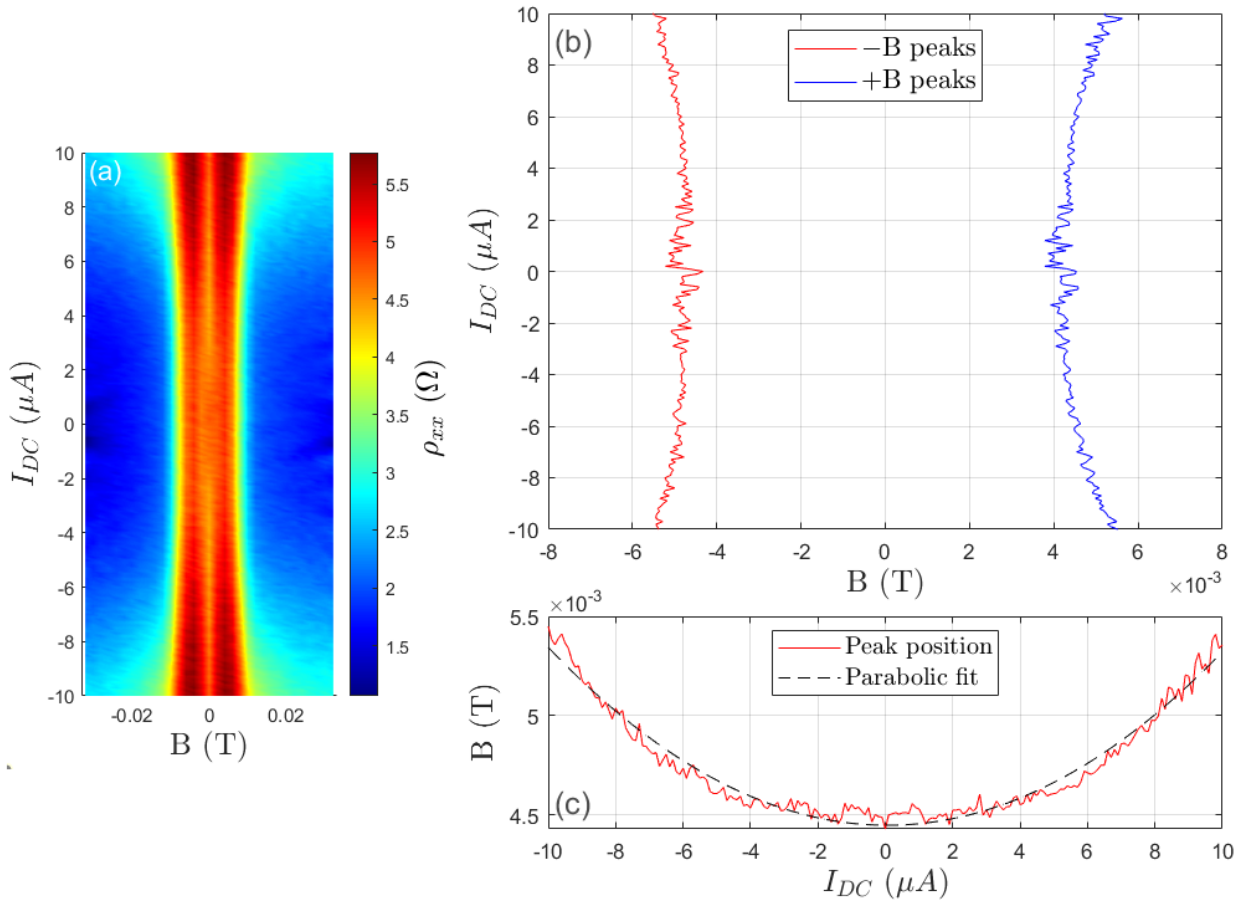

Figure 6.2: a) Phase diagram of the differential resistivity ρ_{xx} vs I_{DC} and B, centered around B=0 T, where a nMR can be observed. On top of the nMR, a double peak feature can also be observed. b) Double peak positions for both $+B$ and $-B$ sides in B vs I_{DC}. The symmetrical noise pattern from $+B$ and $-B$ peak positions is an artifact from Gaussian peak fitting. c) Averaged peak position from $-B$ and $+B$ sides. Parabolic dependence w.r.t. I_{DC} is obtained to be $(B_{dp} - B_{dp}(0))/B_{dp} = (I_{dp}/I_{dp,0})^2$, where $B_{dp}(0)$ = 4.5 mT and $I_{dp,0}$ = 0.27 μA.

cannot attribute the phenomenon of parabolic increasing peak separation with increasing I_{DC} to a ballistic model. We currently do not know the origin of this phenomenon and further investigation is needed.

7. Hydrodynamic Electron Transport

In this section, we analyze ρ_{xx} in the small B-field regime ($B < 0.01$ T) in the context of electron hydrodynamic transport. From the phase diagram, we observe that ρ_{xx} decreases with DC current at zero B-field, which is a sign of electron hydrodynamic transport [25]. To have a better understanding of this phenomenon, first we present evidence of the DC current-induced suppression of electron-electron mean free path. Next, we analyze the DC current evolution of ρ_{xx} with B-field data, which can be compared to the form of the theoretical hydrodynamic correction with magnetic field. Finally, we look for evidence of electron hydrodynamic in the Hall resistivity ρ_{xy}.

7.1 Current-Induced Suppression of Electron-Electron Scattering Mean Free Path

One of the conditions for electron hydrodynamic transport requires the electron-electron scattering length l_{ee} to be much smaller than the width of the sample. Commonly, this condition is achieved through a temperature change. In an ideal 2DEG, the relation between the electron-electron scattering rate τ_{ee}^{-1} and DC current at zero temperature, instead of the usual temperature dependence, was derived by Chaplik [109] and Giuliani

and Quinn: [65]

$$\tau_{ee}^{-1} = \frac{E_F}{4\pi\hbar}\left(\frac{\Delta}{E_F}\right)^2\left[\ln\left(\frac{E_F}{\Delta}\right) + \ln\left(\frac{2Q_{TF}}{k_F}\right) + \frac{1}{2}\right], \tag{7.1}$$

where Δ is the excitation (or excess) energy relative to the Fermi energy E_F (satisfying $\Delta \ll \hbar^2 k_F Q_{TF}/m^*$), Q_{TF}=$2m^*e^2/4\pi\epsilon_r\epsilon_0\hbar^2$ is the 2D Thomas-Fermi screening wave vector, k_F is the Fermi wavevector, ϵ_r is the dielectric constant (∼13.1 for GaAs), and ϵ_0 is the vacuum permittivity. Our sample's bath temperature is 15 mK. For a sufficiently small excess energy, Eq. (7.1) is approximately quadratic with respect to DC current. The excess energy Δ is equal to eV_{DC}, where V_{DC} is the voltage drop across the Hall bar. $\Delta \simeq eV_{DC}$ is an experimental result by Yacoby *et al.* [112] where theory Eq. (7.1) was validated using quantum interference. For our sample, $\Delta \sim 0.4$ meV, which satisfies the condition $\Delta \ll \hbar^2 k_F Q_{TF}/m^*$ where $\hbar^2 k_F Q_{TF}/m^*$=24.7 meV. However, we note that in the work by Yacoby *et al.*, it is suggested that Δ is only proportional to eV_{DC} and the actual excess energy is smaller than the applied voltage.

Using $\Delta = eV_{DC}$, the electron-electron scattering length l_{ee} under DC current can be calculated by Eq. (7.1). We take the voltage across the horizontal probes $V_{DC} = I_{DC} \times R_{xx}$, where R_{xx} is approximately 40 Ω. In Fig. 7.1, the predicted l_{ee} is plotted versus DC current. At ~ 9.5 μA, l_{ee} is equal to W. According to Eq. (7.1), our sample should be transitioning from a ballistic regime to a hydrodynamic regime (recall ballistic regime is when $W \ll l_{ee}, l_{mfp}$ and hydrodynamic $l_{ee} \ll W \ll l_{mfp}$, where $W \ll l_{mfp}$ is trivially satisfied).

Here, we present evidence of l_{ee} decreases by increasing the DC current flowing through the Hall bar device. First, we present ρ_{xx} versus I_{DC} traces for low B-field values in Fig. 7.2. At zero B-field, ρ_{xx} first decreases with current, and increases after I_{DC} ∼4 μA. Away

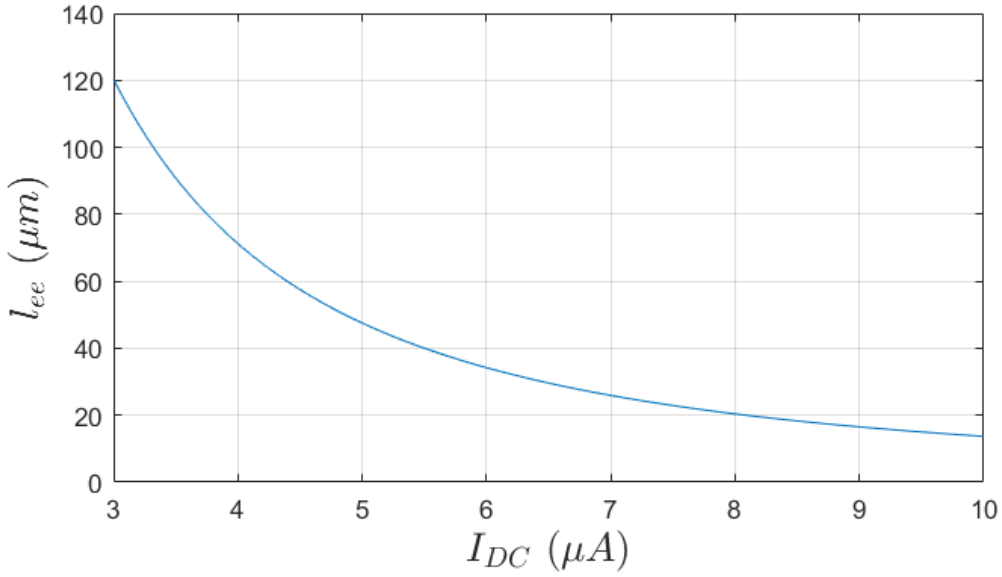

Figure 7.1: Electron-electron scattering mean free path l_{ee} versus I_{DC}, predicted by Eq. (7.1) using $\Delta = eV_e = eI_{DC}R_{xx}$. R_{xx}=43 Ω was used in the calculation (a l_{ee} decreases with increasing I_{DC} and reaches 15 μm at $I_{DC} \sim 9.5\ \mu A$.

from B=0 T, we identify a clear parabolic increase of ρ_{xx} with increasing current. This dependence can be observed even at higher B-fields when SdH and HIROs are present (see gray traces in Fig. 7.2). The transition between the B=0 T to a parabolic dependence occurs within ~8 mT. From analysis of ρ_{xx} traces between 12 mT and 24 mT in Fig. 7.2, we find that the quadratic background dependence follows the relationship:

$$\frac{\Delta\rho_{xx}^{bg}(I_{DC})}{\rho_{xx}(0)} = \left(\frac{I_{DC}}{I_0}\right)^2, \tag{7.2}$$

where $\rho_{xx}(0)$=$1.81 \pm 0.01\ \Omega$, and I_0=$11.4 \pm 0.1\ \mu$A. We attribute this quadratic dependence to a DC current induced increase of the electron-electron scattering rate τ_{ee}^{-1}. Note that the value of I_0 here is comparable to that obtained from the τ_q dependence to I_{DC} discussed in Sec. 4.2, specifically in Eq. (4.1).

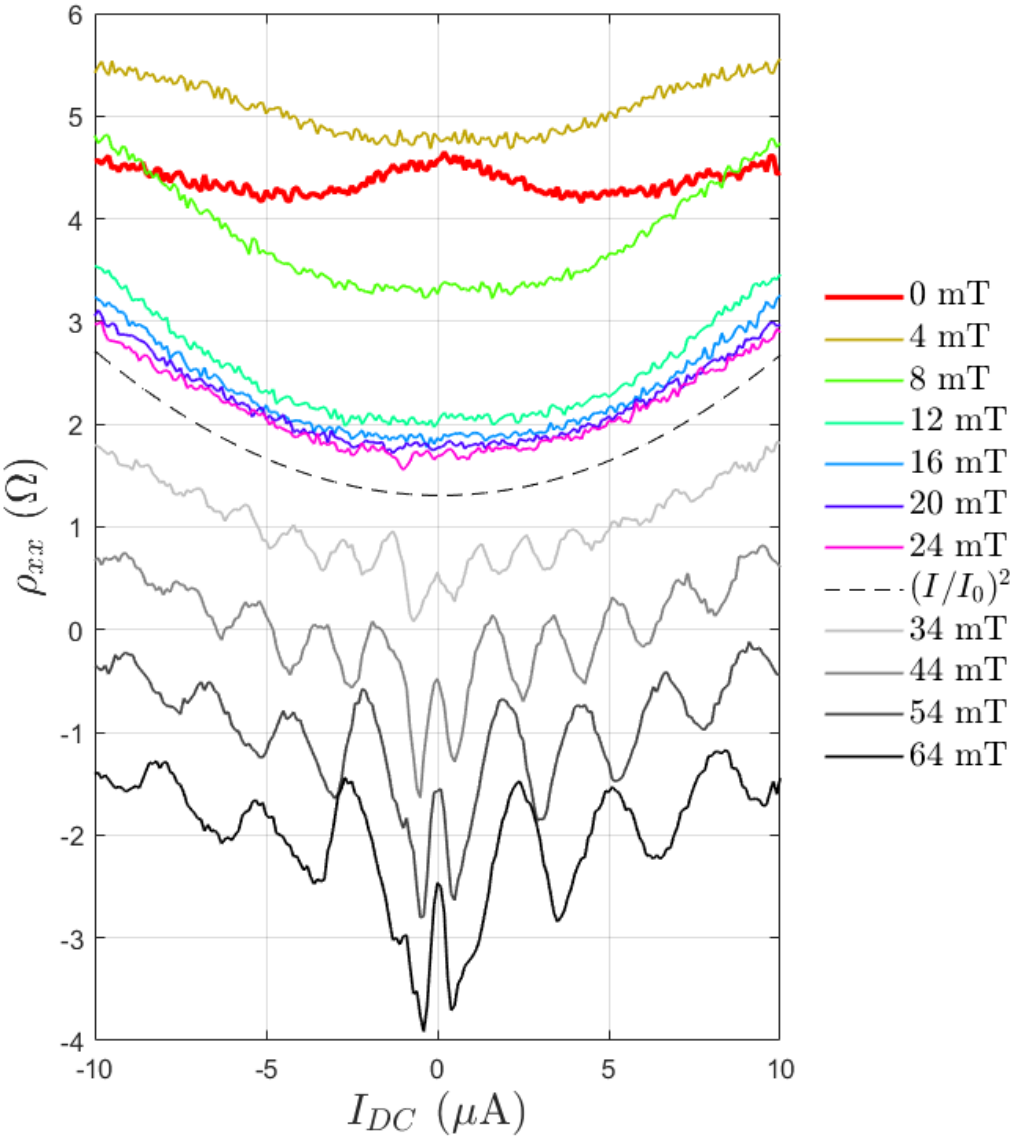

Figure 7.2: Differential resistivity ρ_{xx} versus I_{DC} for different B-fields. At B=0 T, ρ_{xx} initially decreases with increasing current, and starts increasing around $I_{DC} \sim 4\ \mu A$. Away from B=0 T, ρ_{xx} exhibits a quadratic dependence with respect to I_{DC}, which is observable even Above $B \sim 30$ mT, where HIROs start to appear. The dashed line is a quadratic fit of the average ρ_{xx} from 12 mT to 24 mT, shifted down by 0.5 Ω for clarity. This B-field range is selected because it is clear SdH and HIROs, and the hydrodynamic effects are suppressed. The quadratic dependence is found to follow the relationship $\frac{\Delta\rho_{xx}^{bg}}{\rho_{xx}(0)}=(I/I_0)^2$ where $\rho_{xx}(0)$=1.81 $\pm$ 0.01 Ω, and I_0=11.4 $\pm$ 0.4 μA. Traces for $B > 30$ mT are shifted down progressively by 1 Ω each for clarity.

In general, the resistivity of a material is proportional to the sum of the scattering rates from different sources such that ρ_{xx}=$\frac{m^*}{e^2n}\sum_i \tau_i^{-1}$, where n is the carrier concentration, and τ_i^{-1} are independent scattering rates for different sources of scattering [113]. A DC current induced increase in the electron-electron scattering rate τ_{ee}^{-1} results in a correction to the resistivity on the order of τ_{ee}^{-1}. Although electron-electron interactions are momentum conserving, contributions by electron-electron scattering have been known to affect the resistivity observable in non-linear phenomena in 2DEG systems [14,20,107,108,114] (see discussion in Sec. 1.6). A DC current induced quadratic increase in τ_{ee}^{-1} should result in a quadratic change in the resistivity on the order of $\frac{m^*}{e^2n}\tau_{ee}^{-1}$, which follows the same trend, and is the same order of magnitude as the quadratic dependence we observe for our experimental data. In Fig. 7.3, we present the correction from electron-electron scattering from $\frac{m^*}{e^2n}\tau_{ee}^{-1}$ and the parabolic background $\Delta\rho_{xx}^{bg}$ extracted from experimental data. τ_{ee}^{-1} is calculated from Eq. (7.1), with $\Delta = eV_e = eI_{DC}R_{xx}$. Given that Δ is only proportional to eV_{DC} [112], $\Delta = aeV_e$ is obtained from the curve of best fit, where $a = 0.88 \pm 0.01$ which is consistent with the values of $\Delta = 0.82eV_e$ and $\Delta = 0.67eV_e$ reported by Yacoby *et al.* [112]

Lastly, we focus again on the ρ_{xx} vs DC current trace at zero B-field. By subtracting the parabolic dependence $\Delta\rho_{xx}^{bg}$ from ρ_{xx}, it is interesting that we obtain a linear dependence with I_{DC} (see Fig. 7.4). We attribute this DC current-dependent deviation as a hydrodynamic contribution to ρ_{xx}. In the next section, we analyze this contribution in detail by also taking into account the nearby non-zero B-field DC current-induced change in ρ_{xx}.

7.2 Hydrodynamic Magnetoresistance

In the previous section, we established that increasing I_{DC} suppresses l_{ee}, which is one of the conditions for electron hydrodynamic transport. Evidence of DC current-induced hydrodynamic effects can already be observed without B-field from the ρ_{xy} versus I_{DC}

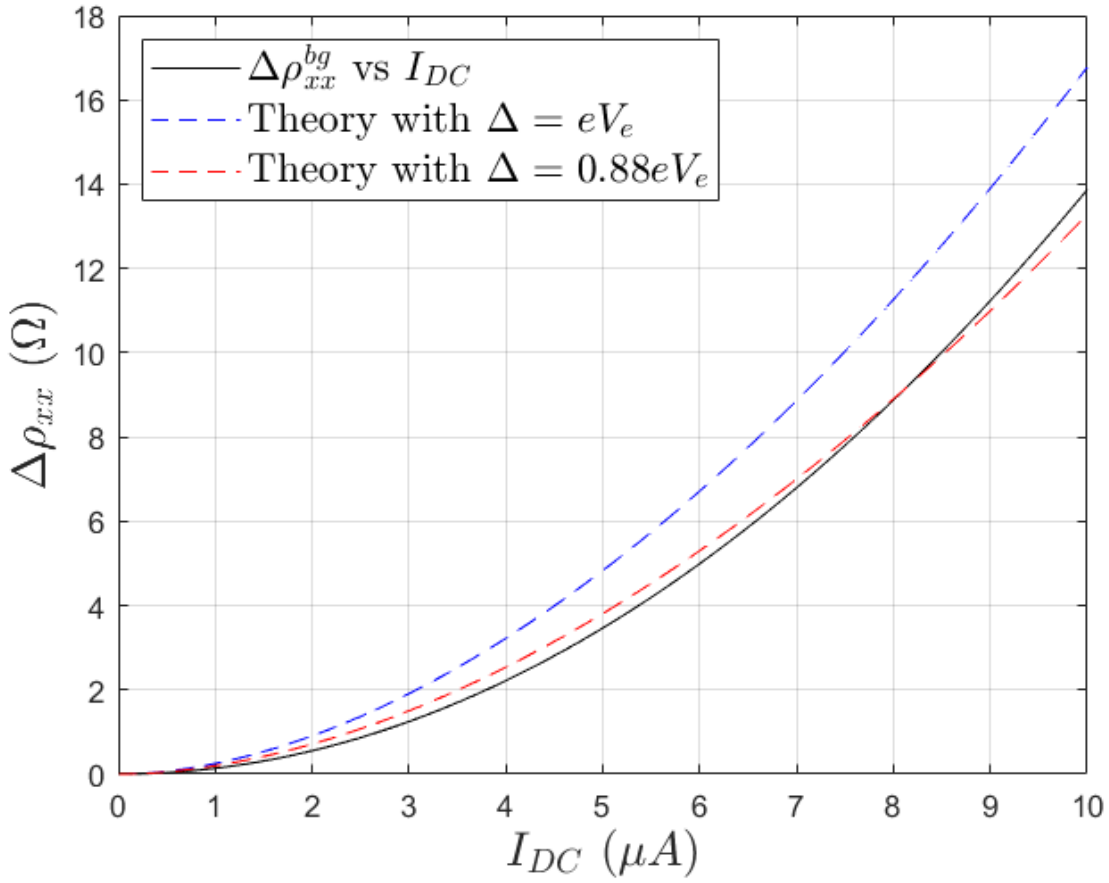

Figure 7.3: $\Delta\rho_{xx}$, the change in differential resistivity ρ_{xx} versus increasing I_{DC}, experiment compared to theory. Black line: parabolic dependence $\Delta\rho_{xx}^{bg}$ vs I_{DC} obtained from experimental data [see Fig. 7.2 and Eq. (7.2)]. Dashed lines: $\Delta\rho_{xx}$ predicted by theory Eq. (7.1) using $\Delta = eV_e$ (in blue). With a correction to the excitation energy Δ such that $\Delta = aeV_e$, we obtain $a = 0.88 \pm 0.01$ from a best fit to $\Delta\rho_{xx}^{bg}$ (in red).

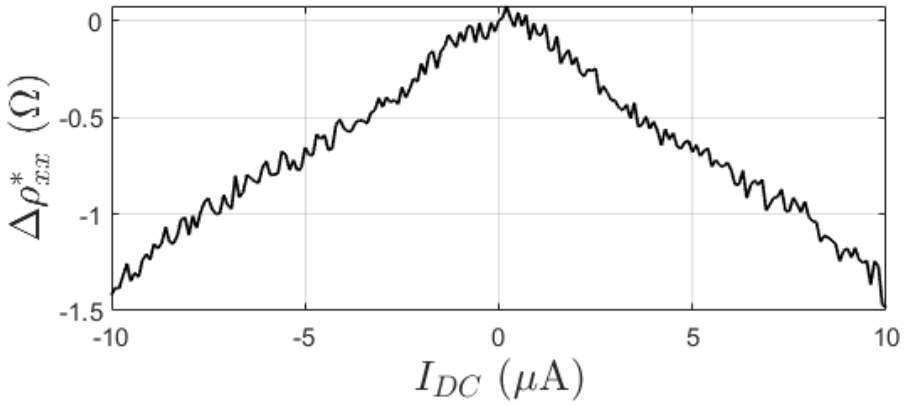

Figure 7.4: $\Delta\rho^*_{xx}$=$\rho_{xx}-\Delta\rho^{bg}_{xx}$ at $B = 0$ T plotted versus DC current, effectively ρ_{xx} (red trace in Fig. 7.2) minus the background quadratic dependence found in Eq. (7.2). We attribute this as a hydrodynamic contribution to ρ_{xx}. From a linear fit we find $\Delta\rho^*_{xx}$=$-0.155|I_{DC}|$). This component has a negative sign.

trace at B=0 T (see Fig. 7.2). In this section, we analyze the evolution of ρ_{xx} versus B-field with increasing DC current. Our goal is to identify the components of ρ_{xx} which evolves with I_{DC} in the small B-field regime ($B < 0.01$ T), and isolate the hydrodynamic contribution. Next, this contribution can be compared to the theoretical viscous correction for ρ_{xx}.

7.2.1 Isolating The Hydrodynamic Contribution

We begin by presenting the ρ_{xx} versus B-field traces for different DC currents up to 10 μA in Fig. 7.5(a). With increasing DC current, the background quadratic dependence $\Delta\rho^{bg}_{xx}$ established in Sec. 7.1 can be readily observed away from B=0 T. Figure 7.5(b) shows $\rho^*_{xx} = \rho_{xx} - \Delta\rho^{bg}_{xx}$, the ρ_{xx} after removing the background parabolic dependence over the entire B-range. We find that for $|B| \lesssim$0.01 T, the ballistic peak decreases with increasing current, meaning there is an additional negative component to ρ_{xx} with increasing I_{DC}. This component can be isolated by computing the deviation of ρ^*_{xx} from ρ^*_{xx} at zero current, $\Delta\rho^*_{xx}$=$\rho^*_{xx} - \rho^*_{xx,I=0}$, which is presented in Fig. 7.5(c) in solid lines. We attribute

this deviation to be evidence of of a transition between the ballistic regime to the hydrodynamic regime. The deviation share similar to the purely hydrodynamic viscous correction [36], showing a growing amplitude with increasing DC current and a rapid decay with increasing B-field. In Fig. 7.5(c), the dips at $|B| \sim 5$ mT and $|B| \sim 8$ mT are artifacts of the methodology due to the subtraction of the zero current trace $\rho^*_{xx,I=0}$. From Fig. 7.5(a), we highlight that the double peak feature is smoother as I_{DC} increases, which leaves a dipping residue when substracting the zero current trance. The double peak is ballistic in origin, discussed in the nMR Sec. 6.1.

Alternatively, we can also directly compute the deviation of ρ_{xx} from the zero current trace, $\rho_{xx} - \rho_{xx}^{I=0}$, which is presented in Fig. 7.6. From this figure, we observe both the background parabolic dependence $\Delta\rho_{xx}^{bg}$ and the hydrodynamic correction $\Delta\rho^*_{xx}$. Clearly, an increasingly strong dip with current is observed for $B < 0.1$ T. Next, we discuss our method to compare $\Delta\rho^*_{xx}$ to the theoretical viscous correction.

7.2.2 Comparison to Theory Using a Perturbative Method

In the purely hydrodynamic regime, following Scaffidi *et al.* [36], the viscous correction to the magnetoresistance can be expressed as:

$$\Delta\rho_{xx}^{hyd} = \frac{m^*}{e^2 n}\frac{v_F l_{ee}}{W^2}\frac{3}{1+\left(\frac{2l_{ee}}{r_c}\right)^2}. \tag{7.3}$$

Equation (7.3) describes the viscous correction in the purely hydrodynamic regime for a 2DEG when $l_{ee} \ll W \ll l_{mfp}$. For our Hall bar device, $W_{eff} \sim W \ll l_{mfp}$ is trivially satisfied since l_{mfp}=145 μm. l_{ee} has been established in Sec. 7.1 to decrease with increasing DC current. The 2DEG is initially in the ballistic regime and with increasing current, l_{ee} decreases and the 2DEG transitions into the hydrodynamic regime. The transitional

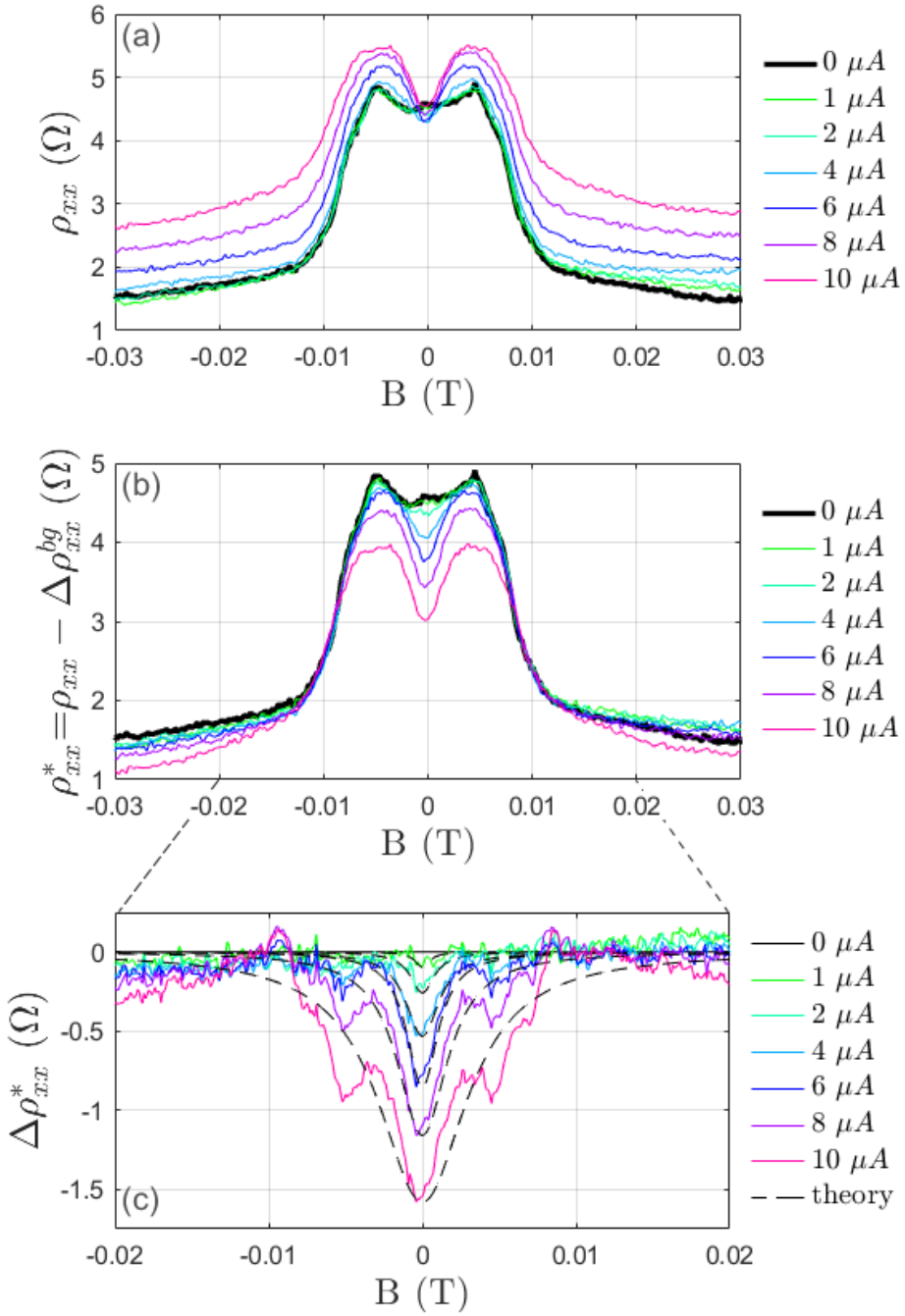

Figure 7.5: (a) Differential resistivity ρ_{xx} plotted versus B-field for different DC currents. (b) ρ^*_{xx}=$\rho_{xx} - \Delta\rho^{bg}_{xx}$, the differential resistivity after removing the quadratic background dependence $\Delta\rho^{bg}_{xx}$, plotted versus B-field. Around B=0 T, an increasingly strong decrease in ρ^*_{xx} with increasing I_{DC} can be observed. (c) Isolated hydrodynamic component, $\Delta\rho^*_{xx}$=$\rho^*_{xx} - \rho^*_{xx,I=0}$ is DC current-dependent deviation of ρ^*_{xx} from the zero current trace. Dashed lines: $r_H\Delta\rho^{hyd}_{xx}$ fit to the data in a perturbative approach. See more details in text.

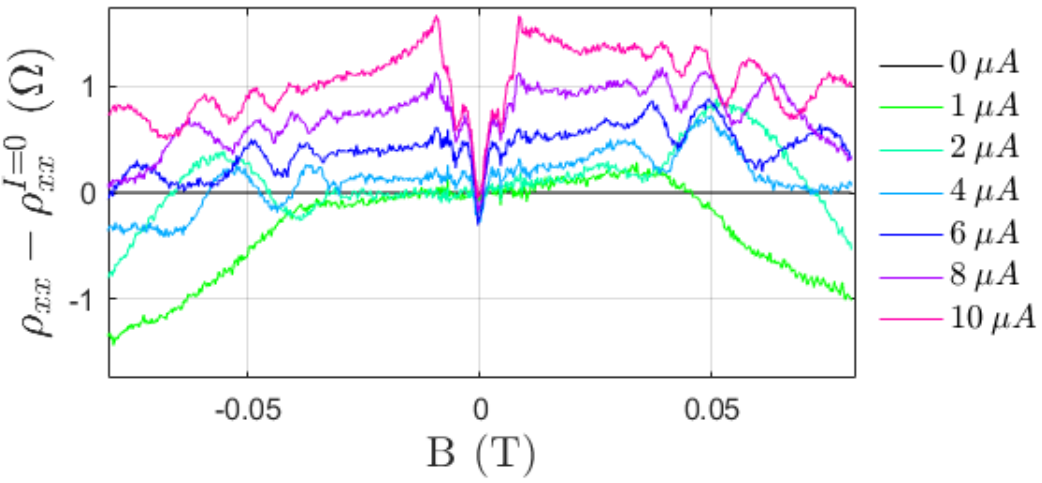

Figure 7.6: ρ_{xx}-$\rho_{xx}^{I=0}$, deviation of differential resistivity ρ_{xx} from ρ_{xx} at I_{DC}=0 μA. Away from B $\sim$0 T, before HIROs, a background parabolic increase in ρ_{xx} with I_{DC} can be observed. Around B=0 T, an increasingly strong negative contribution with increasing I_{DC} is observed, which is signs of hydrodynamic electron transport.

deviation from the ballistic regime is the negative contribution given in Fig. 7.5(c). To examine the experimental data, we use a perturbative approach assuming that the 2DEG is initially in a ballistic regime, and that the change in ρ_{xx} with increasing DC current near zero field is solely hydrodynamic in origin, and that the change is proportional to the viscous correction described in Eq. (7.3). Specifically, our fitting model to the hydrodynamic correction ρ_{xx}^{*} with increasing DC current is equal to:

$$\Delta\rho_{xx} = \rho_{xx} - \rho_{xx}^{I=0} = \Delta\rho_{xx}^{bg} + r_H \Delta\rho_{xx}^{hyd}, \tag{7.4}$$

where $\Delta\rho_{xx}^{bg}$ is the background quadratic increase in ρ_{xx} due to the DC current induced decrease in l_{ee}, and r_H is a dimensionless parameter describing the relative strength of the viscous correction at different DC currents. The fits are presented in Fig. 7.5(c) in dashed lines. The fitting parameters are r_H and l_{ee}, and their dependencies with DC current are presented in Fig. 7.7. l_{ee} decreases exponentially with DC current, which is consistent

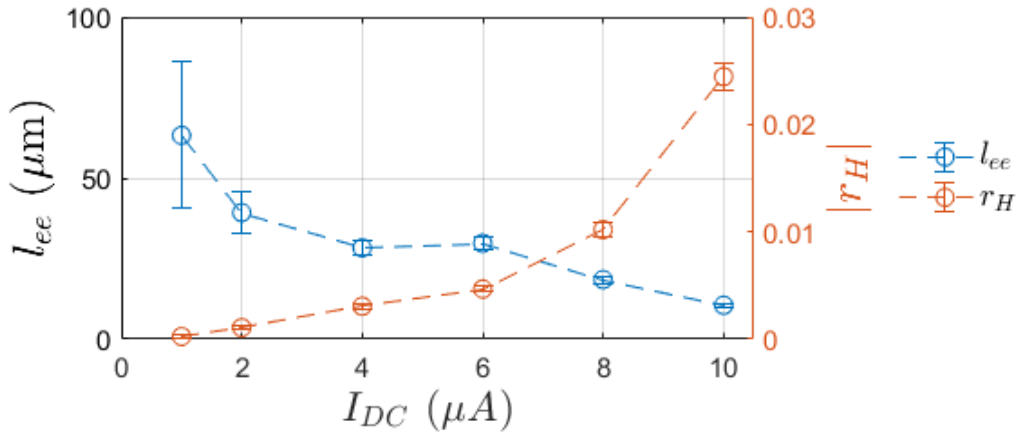

Figure 7.7: Electron-electron scattering length l_{ee} and $|r_H|$ extracted from fits of the traces in Fig. 7.5(c) versus DC current. As I_{DC} increases, l_{ee} decreases and the hydrodynamic component becomes stronger as expected.

with the results obtained from theory Eq. (7.1): at 10 μA, Eq. (7.1) predicts l_{ee}=14 μm and we obtain $l_{ee} \sim 11$ μm. $|r_H|$ increases exponentially with DC current which is reflective of the growing contribution of the hydrodynamic component.

Lastly, we estimate the electron shear viscosity [64] η, defined as η=$\frac{1}{4}v_F^2\tau_{ee}$, to be 0.7 m^2/s at 10 μA. In comparison, in the work of a temperature-induced hydrodynamic regime, with no DC current, η=0.3 m^2/s at T=1.4 K is found by Gusev *et al* in Ref. [39]).

7.3 Hydrodynamic Hall Resistivity

In the previous section, we discussed the increasing hydrodynamic contribution to ρ_{xx} with increasing I_{DC} near zero B-field. Similarly, the growing influence of hydrodynamics affects the differential Hall resistivity ρ_{xy}. ρ_{xy} was measured from the voltage across the Hall bar system, and the data for $I_{DC} = 0$ μA, $I_{DC} = 4$ μA and $I_{DC} = 8$ μA versus B-field are presented in Fig. 7.8. In the small magnetic field regime ($\sim$ 10 mT), the resistivity ρ_{xy} diverges from the well-known Hall resistivity linear relation $\rho_{xy}^{bulk} = B/en$. To better

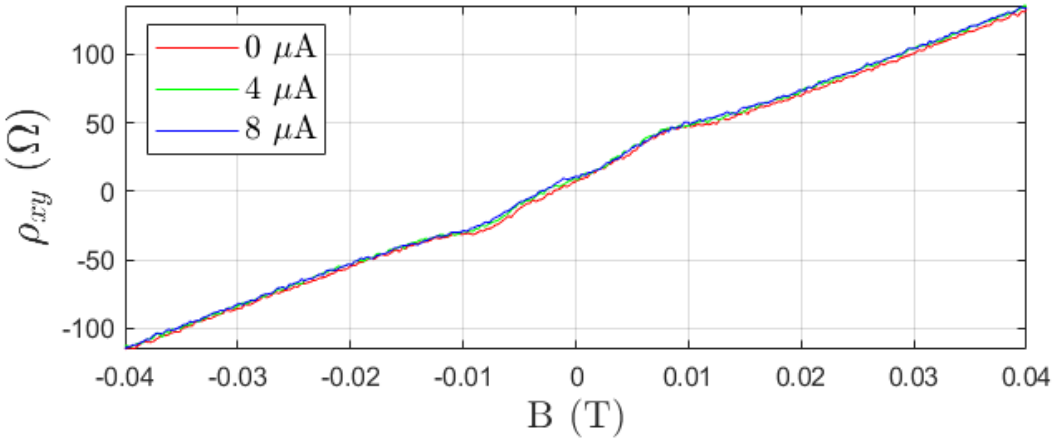

Figure 7.8: Hall resistivity ρ_{xy} plotted versus B-field for I_{DC}=0 μA, 4 μA, 8 μA. For $|B| \lesssim$0.01 T, ρ_{xy} stray away from the linear bulk Hall resistivity.

understand this phenomenon, we compute the deviation from the conventional Hall resistivity $\Delta\rho_{xy} = \rho_{xy} - \rho_{xy}^{bulk}$, presented in Fig. 7.9(a). The sharp peaks near $|B| \sim 8$ mT arise from ballistic transport [36,39,115]. At zero B-field, The change in the slope from positive to negative with increasing DC current is a signature of hydrodynamics.

Similarly to ρ_{xx}, our objective is to compare the viscous correction in ρ_{xy} to theory in a perturbative method. In the purely hydrodynamic regime, the viscous Hall correction to ρ_{xy} was derived by Alekseev [75] and Scaffidi *et al.* [36] and found to be:

$$\frac{\Delta\rho_{xy}^{hyd}}{\rho_{xy}^{bulk}} = -\left[\frac{6}{1+(2l_{ee}/r_c)^2}\left(\frac{l_{ee}}{W}\right)^2\right], \tag{7.5}$$

where ρ_{xy}^{bulk}=$-B/en$ is the bulk Hall resistivity, and $\Delta\rho_{xy}^{hyd}$=$\rho_{xy} - \rho_{xy}^{bulk}$ is the hydrodynamic contribution to the bulk Hall resistivity. The DC current-induced hydrodynamic contribution to $\Delta\rho_{xy}$ can be better visualized by taking the ratio $\Delta\rho_{xy}/\rho_{xy}^{bulk}$, following the approach of Gusev *et al.* [39] [see Fig. 7.9(b)]. To take the ratio $\Delta\rho_{xy}/\rho_{xy}^{bulk}$ of the experimental data is non-trivial, as $\rho_{xy}^{bulk} = 0$ at zero B-field. The solution is to transform the data into a function of B, which can then be divided by ρ_{xy}^{bulk}. In our case, the function used

is a sum of polynomials times B [see black lines in Fig. 7.9(a)]. The resulting $\Delta\rho_{xy}/\rho_{xy}^{bulk}$ is presented in Fig. 7.9(b). The negative value near 0 T in the 8 μA trace is a clear sign of the growing impact of hydrodynamics. The deviation of $\Delta\rho_{xy}/\rho_{xy}^{bulk}$ from the $I_{DC} = 0$ μA trace, $\Delta\rho_{xy}^{*}$=$\rho_{xy} - \rho_{xy,I=0}$, is presented in Fig. 7.9(c) in solid lines, which is the DC current-induced hydrodynamic contribution. We fit $\Delta\rho_{xy}^{*}$ to

$$\Delta\rho_{xy}^{hyd} = r_H \Delta\rho_{xy}^{hyd} \tag{7.6}$$

in a perturbative method, where r_H is a dimensionless fitting parameter reflecting the impact of the viscous correction to ρ_{xy} at different DC currents. We find that increasing the DC current "amplifies" $\Delta\rho_{xy}^{*}/\rho_{xy}^{bulk}$ near zero field, and at I_{DC}=8 μA, the minimum value at 0 T equates to an electron-electron scattering length l_{ee} of 29 μm, with a r_H factor of 0.019. These values are consistent with those from our analysis of ρ_{xx} and theory Eq. (7.1) for l_{ee} [see also Fig. 7.5(d)].

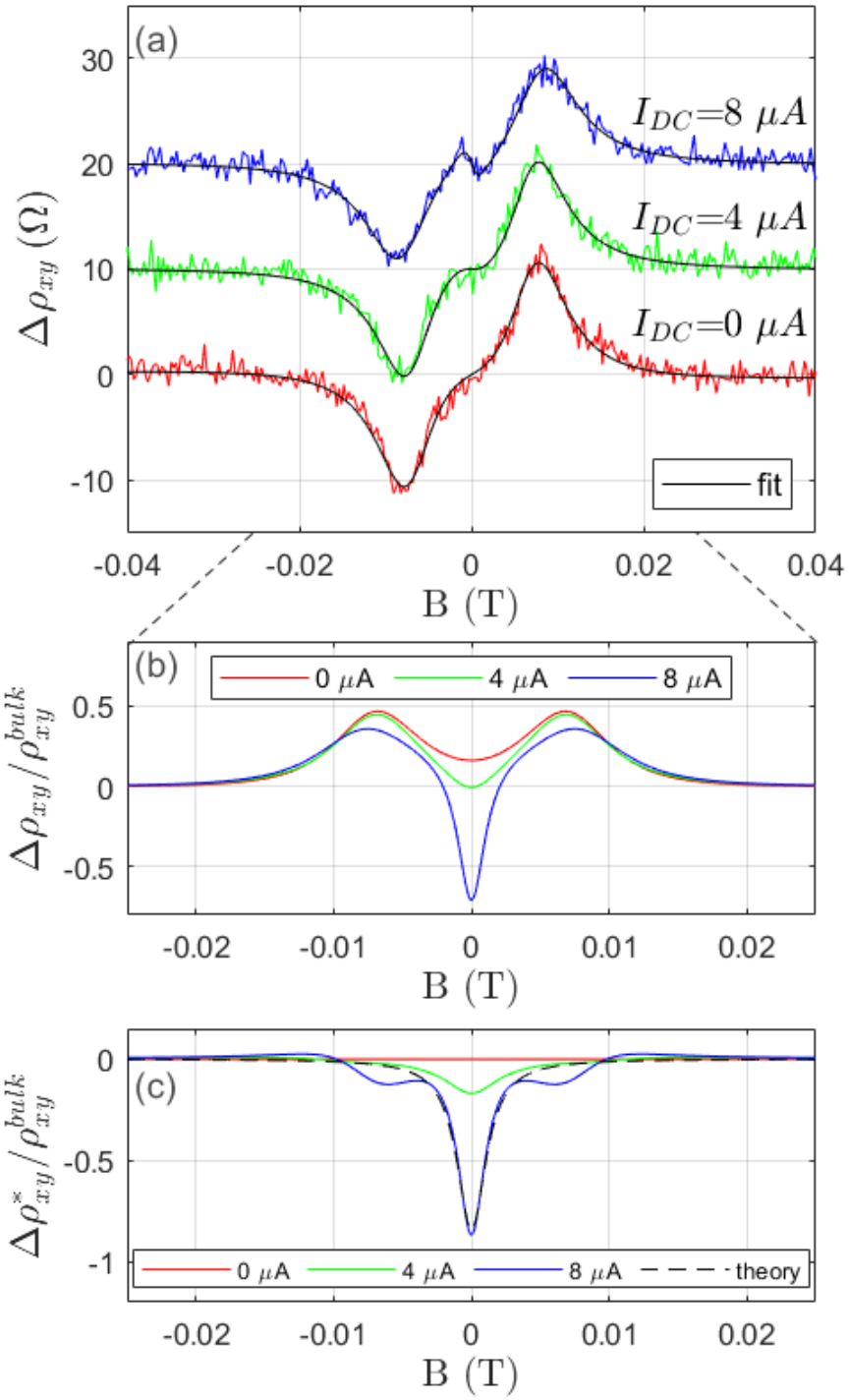

Figure 7.9: (a) Deviation from Hall resistivity $\Delta\rho_{xy}$=ρ_{xy}−ρ_{xy}^{bulk} versus B-field. Black lines: fits to a polynomial function times B, to allow for division by ρ_{xy}^{bulk}. Traces for each I_{DC} value are offset by 10 Ω for clarity. (b) $\Delta\rho_{xy}/\rho_{xy}^{bulk}$ versus B-field. The decreasing value of the ratio at B=0 T is signs of hydrodynamic electron transport. (c) Isolated hydrodynamic component $\Delta\rho_{xy}^{*}/\rho_{xy}^{bulk} = (\Delta\rho_{xy} - \Delta\rho_{xy,I=0})/\rho_{xy}^{bulk}$ versus B-field. Dashed line: hydrodynamic theory Eq. (7.5) fit to I_{DC}=8 μA trace.

8. Conclusion

In this thesis, we have presented studies of non-linear phenomena in the small B-field regime of a GaAs/AlGaAs narrow ultra-high mobility Hall bar, under DC current densities up to 0.67A/m. Our study mainly focused on analyzing our data on HIROs, which arise from elastic impurity scattering between Landau levels tilted by the Hall field. Furthermore, we have also presented our studies on the other phases found in the low B-field high DC current regime of our 2DEG, namely SdH oscillations, phase inversion of SdH oscillations, nMR and DC current-induced electron hydrodynamic transport.

8.1 Summary of Parameters Extracted

We investigated the HIRO frequency and amplitude, and compared the experimental data to both theories by Yang *et al.* [4] and Vavilov *et al.* [102]. First, we confirmed the I_{DC}/B oscillation frequency dependence described in theory Eq. (2.3). Next, by fitting theory Eq. (2.11) to data, we obtained an effective width $W_{eff} = 11$ μm of the Hall bar, a backscattering lifetime $\tau_\pi = 5$ ns and a DC current dependence to quantum lifetime τ_q^{HIRO}. The current dependence of τ_q^{HIRO} is found to be $1/\tau_q \propto I_{DC}^2$, where τ_q^{HIRO} varies from $\sim$40 ps at 2 μA to $\sim$18 ps at 10 μA. We associate this dependence with an increasing electron temperature. The τ_q^{HIRO} was also found to be several times larger than τ_q^{SdH} obtained from SdH oscillations, which requires further theoretical investigation. At low

DC current, a sharp dip in ρ_{xx} was observed. By comparing to theory, an inelastic relaxation lifetime of 580 ps was obtained. Lastly, we observe a new "fractional" HIRO-like resonance at HIRO order $M \approx 1.5$, the origin of which is currently unknown.

From SdH oscillations at zero DC current, by fitting to theory Eq. (1.2), we obtained parameters R_0=11.4 ± 0.6 Ω and τ_q=11.5 ± 0.3 ps. The value of R_0 is much closer to the bulk resistance of 14 Ω, than the actual resistance at zero B-field of 43 Ω, implying SdH oscillations are independent from nMR. At non-zero DC current, in terms of the phase inversion of SdH oscillations, we have found that the rising electron temperature with DC current model by Studenikin *et al.* [33] match with experimental data. By performing a Monte Carlo approach on the parameters given in the form of the DC current dependence of electron temperature T_e in Eq. (1.5), it is possible to fit the theory Eq. (1.4) to the experimental data to obtain T_e. We have obtained a dependence $T_e = T_0 + 1.0 I_{DC}^{0.6}$, which is in agreement with the previous work [33]. Thus, we confirm that electron heating is a viable explanation for phase inversion of the SdH oscillations.

From the negative magnetoresistance around zero B-field, we extracted $W = 0.65 r_c$ from the double peak feature, which is in agreement with the $W \sim 0.55 r_c$ theoretical value. We also report a positional parabolic dependence of B versus I_{DC} for the double peak, which requires further investigation.

Lastly, we report signs of DC current-induced hydrodynamic effect in both ρ_{xx} and ρ_{xy}. At zero B-field, we observe a decrease in ρ_{xx} versus I_{DC}, which is a known signature of hydrodynamics [25]. We extracted the current-dependent hydrodynamic contribution at small B-fields for both ρ_{xx} and ρ_{xy} and compared to the purely hydrodynamic viscous correction in a perturbative method. From the comparison, we extract l_{ee} which is con-

W_{eff} (μm)	l_{ee} (μm)	η (m^2/s)	τ_q^{SdH} (ps)	τ_q^{HIRO} (ps)	τ_π (ns)
11	11	0.7	11.5	18 - 40	5

Table 8.1: Summary of key extracted parameters from Chapters 4 to 7. The value of l_{ee} is for I_{DC}=10 μA determined in Sec. 7.2.2. The value of η is for I_{DC}=10 μA determined in Sec. 7.2.2. τ_q^{HIRO} depends on I_{DC} hence a range of values is given (see Sec. 4.2).

sistent with the theoretical prediction of l_{ee} versus DC current from Eq. 7.1. All the key parameters obtained from the analysis are presented in Table 8.1.

8.2 Summary of The Phase Diagram

In this thesis, we performed detailed analysis for five non-linear phenomena identifiable from the phase diagram of differential resistivity ρ_{xx} presented in Fig. 1.1. Each phase appears in its own region delimited by its own boundaries, which can be summarized in a schematic of the low B-field high DC current regime, presented in Fig. 8.1. SdH oscillations at zero current can be observed at $B > B_q$, where B_q is related to the quantum lifetime τ_q by $\omega_c\tau_q = 1$. SdH oscillations can still be observed at non-zero current, although their amplitude decay significantly with increase I_{DC}. At $I_{DC} = I_{PhI}$, there is phase inversion of the SdH oscillations, where maxima become minima and vice versa. Around B=0 T, there is a nMR phase, which is a sign of ballistic transport. The nMR is bounded by $B_{W_{eff}}$, where $B_{W_{eff}}$ can be evaluated from $W_{eff} = 2r_c$. With increasing DC current, a contribution to ρ_{xx} can be identified as evidence of DC current-induced electron hydrodynamic transport. Lastly, HIROs can be observed at $B > B_q^{HIRO}$ and $I_{DC} > I_{HIRO}$, where B_q^{HIRO} can be evaluated from $\omega_c\tau_q^{HIRO} = 1$. B_q^{HIRO} is related to the quantum lifetime τ_q^{HIRO} extracted from HIROs, as there is a discrepancy between τ_q extracted from

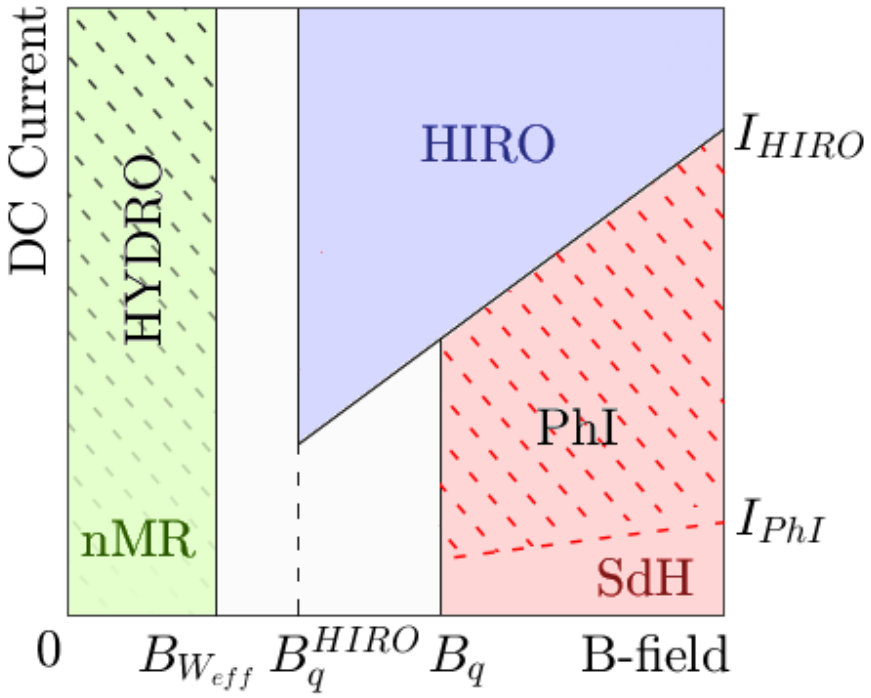

Figure 8.1: Summary of the observed nonlinear phenomena regions and boundaries in a phase diagram of ρ_{xx} vs B and I_{DC}. SdH oscillations and phase inversion of SdH oscillations are observable at $B > B_q$; nMR is observable at low B-fields bounded by $B_{W_{eff}}$; Hydrodynamic effects are observable at low B-fields and high DC current; HIROs are observable at $B > B_q^{HIRO}$ and $I > I_{HIRO}$, which is delimited by the first HIRO maxima. Boundaries are defined in the text.

SdH oscillations and HIROs. I_{HIRO} is simply the DC current as a function of B-field of the first HIRO maxima.

8.3 Outline for Future Research

Although we understand the non-linear phenomena presented in the phase diagram in Fig. 1.1, there are still many unanswered questions that can be topics of research for the future. From an experimental point of view, the obvious path for experiments in the future is to use higher DC current on a similar sample. This process can possibly give

us hints for the origin of the "1.5" HIRO-like feature, and more concrete evidence of DC current-induced hydrodynamics.

In terms of analysis, we reiterate that the unresolved problems are: 1. the discrepancy between quantum lifetime τ_q^{HIRO} extracted from HIROs compared to SdH oscillations 2. the decreasing nature of τ_q^{HIRO} with respect to DC current 3. DC current induced hydrodynamic at higher DC current. For points 1 and 2, we suggest doing a full analysis of HIROs oscillation with the Vavilov *et al.* [102] full Eq. (2.10) to check for the validity of theory. τ_q^{HIRO} and τ_π in our work were extracted u using the approximate Eq. (2.11), which is only a sinusoidal function and doesn't take into account small I_{DC} effects, which may influence the fitting for the quantum lifetime. For point 3, we suggest a Boltzmann theory analysis similar to theoretical study from Molenkamp and De Jong [25,68], Scaffidi *et al.* [36], Raichev *et al.* [81].

8.3.1 Boltzmann Transport Theory Analysis for DC Current-Induced Hydrodynamic Electron Transport

Recent electron hydrodynamic theories [25, 36, 42, 68, 81] for effects on the magnetotransport in a 2DEG are based on a Boltzmann transport formalism. For the analysis of our sample, a perturbative method was used instead, because our sample is transitioning from the ballistic regime to the hydrodynamic regime ($l_{ee} \sim W_{eff}$). However, given further experiments at even higher DC current, the perturbative approach could be inaccurate as l_{ee} decreases well below the sample width W_{eff}. Using an existing and more complete theory to analyze higher DC current experimental data, as well as the data presented in this thesis, could help us further our understanding of DC current-induced electronic transport. It would also be an opportunity to validate the Boltzmann equation formulation of electronic hydrodynamic transport.

More specifically, the Boltzmann transport formulation of electron hydrodynamics predicts the magneto-resistivity given relevant length scales l_{ee}, l_{mfp} and W. This can be used to compare with our experimental data. This method could also validate Eq. (7.1) given the DC current relationship with l_{ee}.

A. GaAs/AlGaAs Hetero-Structure Fabrication Process

The 2DEG investigated is in the quantum well region of a GaAs/AlGaAs hetero-structure grown by molecular beam epitaxy. The material was provided by L. N. Pfeiffer, and K. W. West from the Pfeiffer Group at Princeton University. The growth method consists of thin-film deposited in an ultra-high vacuum to produce high purity of the grown films (see review in Ref. [105]). The relevant layers of the quantum well doping are presented Fig. A.1. The 2DEG is a 30 nm GaAs layer. On each side of the 2DEG, there is a barrier composed of $Al_{0.30}Ga_{0.70}As$ with a quantum well doping region. From the 2DEG, in order, the barrier consists of a 78 nm layer of $Al_{0.30}Ga_{0.70}As$, a 57 nm layer of AlAs, a 5.7 nm layer of GaAs, a layer of SiAs, a 23 nm of GaAs, a 57 nm layer of AlAs, a 100 nm layer of $Al_{0.30}Ga_{0.70}As$.

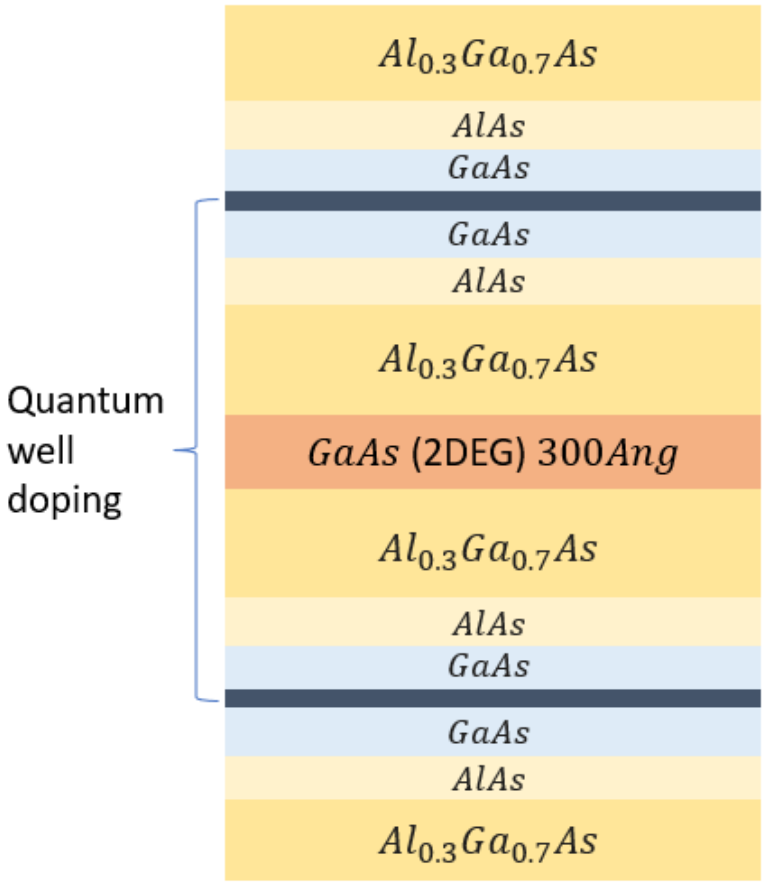

Figure A.1: Schematic of the layers surrounding the 2DEG. The AlGaAs barrier on either side of the 2DEG has a quantum well doping region. The layer thicknesses are presented in the text.

B. Hall Resistivity Under Illumination

We have also measured the Hall resistivity under illumination with $V_{LED} = 3$ V, up to 230 seconds. The objective is to determine the effect of illumination on the hydrodynamic contribution at B=0 T presented in Sec. 7.3. At different duration during the illumination process, the Hall resistivity was measured under zero DC current and at $I_{DC} = 8$ μA. The electron concentration n decreased linearly with increasing illumination time t (see Fig. B.1), from $n = 2.0 \times 10^{11}$ cm^{-2} without illumination to $n = 1.7 \times 10^{11}$ cm^{-2} at $t = 230$ s.

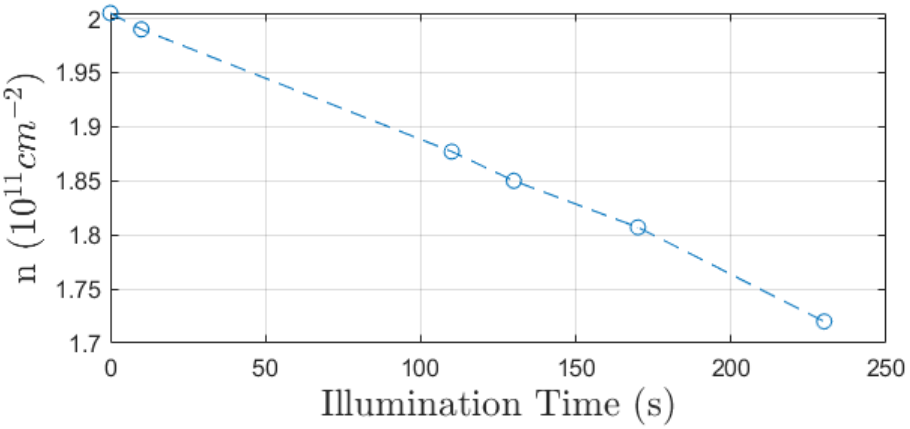

Figure B.1: Electron concentration n obtained from Hall resistivity plotted versus illumination time under a 3V LED. The electron concentration decreases linearly with illumination time, down $\sim 10\%$ over $t = 230$ s.

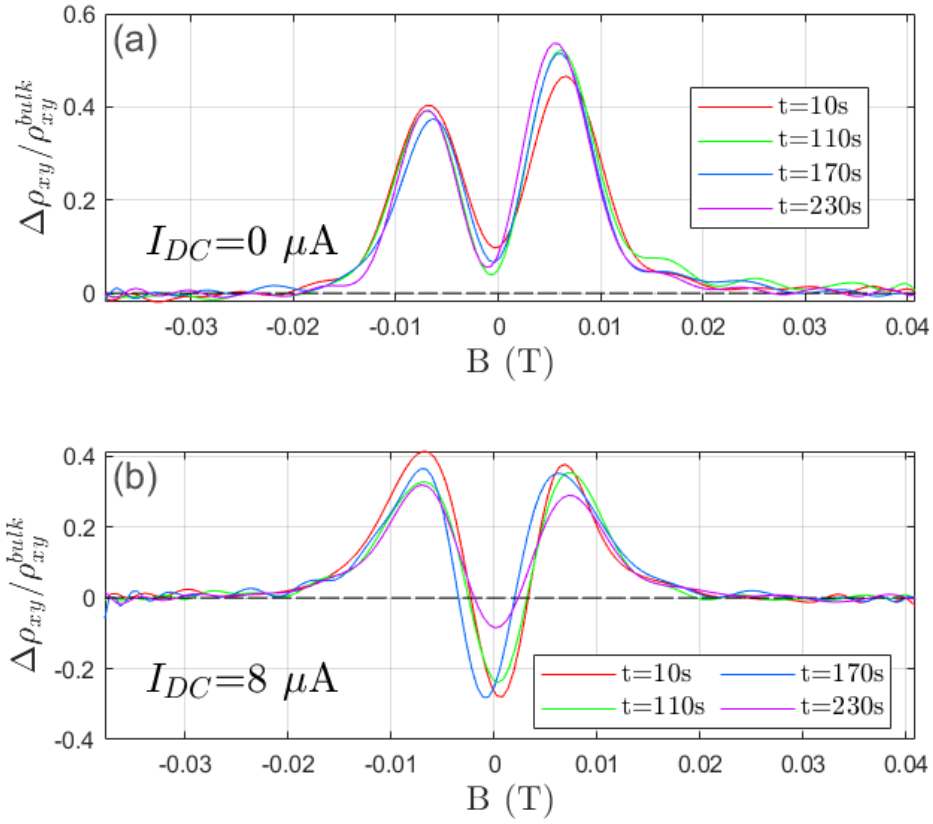

Figure B.2: $\Delta\rho_{xy}/\rho_{xy}^{bulk}$ plotted versus B-field after different illumination time, without DC current (a) and with DC current of 8 μA (b). There is no correlation between illumination time and hydrodynamic component.

It is possible to apply the same methods from Sec. 7.3 to determine whether a change of illumination affects the hydrodynamic contribution $\Delta\rho_{xy}^{*}/\rho_{xy}^{bulk}$. To obtain $\Delta\rho_{xy}^{*} = \rho_{xy}^{DC>0} - \rho_{xy}^{DC=0}$ at each t_{illum}, $\Delta\rho_{xy}^{*} = \Delta\rho_{xy}^{DC>0} - \Delta\rho_{xy}^{DC=0}$ is used where $\Delta\rho_{xy} = \rho_{xy} - \rho_{xy}^{Bulk}$, to account for the slight concentration change between the setup with and without DC current. $\Delta\rho_{xy}$ for each t_{illum} and current setup can be fitted from the method outlined in Sec. 7.3. The hydrodynamic contribution $\Delta\rho_{xy}^{*}/\rho_{xy}^{bulk}$ for each t_{illum} can be calculated using $\rho_{xy}^{bulk} = B/en_s$. The results are presented in Fig. B.2, and show no significant correlation between $\Delta\rho_{xy}^{*}/\rho_{xy}^{bulk}$ and illumination duration t_{illum}.

References

[1] Z. T. Wang, M. Hilke, N. Fong, D. G. Austing, S. A. Studenikin, K. W. West, and L. N. Pfeiffer, "Non-linear transport phenomena and current-induced hydrodynamics in ultra-high mobility two-dimensional electron gas." unpublished, N.D.

[2] K. v. Klitzing, G. Dorda, and M. Pepper, "New method for high-accuracy determination of the fine-structure constant based on quantized hall resistance," *Phys. Rev. Lett.*, vol. 45, pp. 494–497, Aug 1980.

[3] D. C. Tsui, H. L. Stormer, and A. C. Gossard, "Two-dimensional magnetotransport in the extreme quantum limit," *Phys. Rev. Lett.*, vol. 48, pp. 1559–1562, May 1982.

[4] C. Yang, J. Zhang, R. Du, J. Simmons, and J. Reno, "Zener tunneling between landau orbits in a high-mobility two-dimensional electron gas," *Phys. Rev. Lett.*, vol. 89, no. 7, p. 076801, 2002.

[5] M. A. Zudov, R. R. Du, J. A. Simmons, and J. L. Reno, "Shubnikov–de haas-like oscillations in millimeterwave photoconductivity in a high-mobility two-dimensional electron gas," *Phys. Rev. B*, vol. 64, p. 201311, Oct 2001.

[6] S. Vitkalov, "Nonlinear transport of 2d electrons in crossed electric and quantizing magnetic fields," *Int. J. Mod. Phys. B*, vol. 23, no. 23, pp. 4727–4753, 2009.

[7] I. Dmitriev, A. Mirlin, D. Polyakov, and M. Zudov, "Nonequilibrium phenomena in high landau levels," *Rev. Mod. Phys.*, vol. 84, no. 4, p. 1709, 2012.

[8] A. A. Bykov, J.-q. Zhang, S. Vitkalov, A. K. Kalagin, and A. K. Bakarov, "Effect of dc and ac excitations on the longitudinal resistance of a two-dimensional electron gas in highly doped gaas quantum wells," *Phys. Rev. B*, vol. 72, p. 245307, Dec 2005.

[9] W. Zhang, M. A. Zudov, L. N. Pfeiffer, and K. W. West, "Resistance oscillations in two-dimensional electron systems induced by both ac and dc fields," *Phys. Rev. Lett.*, vol. 98, p. 106804, Mar 2007.

[10] J.-q. Zhang, S. Vitkalov, A. Bykov, A. Kalagin, and A. Bakarov, "Effect of a dc electric field on the longitudinal resistance of two-dimensional electrons in a magnetic field," *Phys. Rev. B*, vol. 75, no. 8, p. 081305, 2007.

[11] W. Zhang, H.-S. Chiang, M. Zudov, L. Pfeiffer, and K. West, "Magnetotransport in a two-dimensional electron system in dc electric fields," *Phys. Rev. B*, vol. 75, no. 4, p. 041304, 2007.

[12] A. A. Bykov, "Zener tunneling between landau levels in a double quantum well at high filling factors," *Sov. Phys. JETP*, vol. 88, no. 6, pp. 394–397, 2008.

[13] Y. Dai, Z. Yuan, C. Yang, R. Du, M. Manfra, L. Pfeiffer, and K. West, "Magnetotransport in zener tunneling regime in a high-mobility two-dimensional hole gas," *Phys. Rev. B*, vol. 80, no. 4, p. 041310, 2009.

[14] A. T. Hatke, M. A. Zudov, L. N. Pfeiffer, and K. W. West, "Role of electron-electron interactions in nonlinear transport in two-dimensional electron systems," *Phys. Rev. B*, vol. 79, p. 161308, Apr 2009.

[15] A. T. Hatke, H.-S. Chiang, M. A. Zudov, L. N. Pfeiffer, and K. W. West, "Zero differential resistance in two-dimensional electron systems at large filling factors," *Phys. Rev. B*, vol. 82, p. 041304, Jul 2010.

[16] A. T. Hatke, M. A. Zudov, L. N. Pfeiffer, and K. W. West, "Resistance oscillations induced by the hall field in tilted magnetic fields," *Phys. Rev. B*, vol. 83, p. 081301, Feb 2011.

[17] A. Bykov, D. Dmitriev, I. Marchishin, S. Byrnes, and S. Vitkalov, "Zener tunneling between landau orbits in two-dimensional electron corbino rings," *Appl. Phys. Lett.*, vol. 100, no. 25, p. 251602, 2012.

[18] S. Wiedmann, G. Gusev, O. Raichev, A. Bakarov, and J. Portal, "Nonlinear transport phenomena in a two-subband system," *Phys. Rev. B*, vol. 84, no. 16, p. 165303, 2011.

[19] Q. Shi, M. A. Zudov, J. Falson, Y. Kozuka, A. Tsukazaki, M. Kawasaki, K. von Klitzing, and J. Smet, "Hall field-induced resistance oscillations in mgzno/zno heterostructures," *Phys. Rev. B*, vol. 95, p. 041411, Jan 2017.

[20] M. A. Zudov, I. A. Dmitriev, B. Friess, Q. Shi, V. Umansky, K. von Klitzing, and J. Smet, "Hall field-induced resistance oscillations in a tunable-density gaas quantum well," *Phys. Rev. B*, vol. 96, p. 121301, Sep 2017.

[21] J. Mi, H. Liu, J. Shi, L. N. Pfeiffer, K. W. West, K. W. Baldwin, and C. Zhang, "Quantum oscillations in a two-dimensional electron system under low-frequency microwave irradiation," *Phys. Rev. B*, vol. 100, p. 235437, Dec 2019.

[22] S. A. Studenikin, G. Granger, A. Kam, A. S. Sachrajda, Z. R. Wasilewski, and P. J. Poole, "Nonlinear magnetotransport phenomena in high-mobility two-

dimensional electrons in ingaas/inp and gaas/algaas," *Phys. Rev. B*, vol. 86, p. 115309, Sep 2012.

[23] S. Baer, C. Rössler, S. Hennel, H. C. Overweg, T. Ihn, K. Ensslin, C. Reichl, and W. Wegscheider, "Nonequilibrium transport in density-modulated phases of the second landau level," *Phys. Rev. B*, vol. 91, p. 195414, May 2015.

[24] V. Yu, M. Hilke, P. J. Poole, S. Studenikin, and D. G. Austing, "Phase diagram of quantum hall breakdown and nonlinear phenomena for ingaas/inp quantum wells," *Phys. Rev. B*, vol. 98, p. 165434, Oct 2018.

[25] L. W. Molenkamp and M. J. M. de Jong, "Electron-electron-scattering-induced size effects in a two-dimensional wire," *Phys. Rev. B*, vol. 49, pp. 5038–5041, Feb 1994.

[26] T. Ando, "Theory of quantum transport in a two-dimensional electron system under magnetic fields ii. single-site approximation under strong fields," *J. Phys. Soc. Jpn.*, vol. 36, no. 6, pp. 1521–1529, 1974.

[27] T. Ando, "Theory of quantum transport in a two-dimensional electron system under magnetic fields. iv. oscillatory conductivity," *J. Phys. Soc. Jpn.*, vol. 37, no. 5, pp. 1233–1237, 1974.

[28] T. Ando, "Theory of cyclotron resonance lineshape in a two-dimensional electron system," *J. Phys. Soc. Jpn.*, vol. 38, no. 4, pp. 989–997, 1975.

[29] T. Ando, "Self-consistent results for a gaas/al x ga1-x as heterojunciton. ii. low temperature mobility," *J. Phys. Soc. Jpn.*, vol. 51, no. 12, pp. 3900–3907, 1982.

[30] P. T. Coleridge, "Small-angle scattering in two-dimensional electron gases," *Phys. Rev. B*, vol. 44, pp. 3793–3801, Aug 1991.

[31] A. Isihara and L. Smrcka, "Density and magnetic field dependences of the conductivity of two-dimensional electron systems," *J. Phys. C: Solid State Phys.*, vol. 19, pp. 6777–6789, dec 1986.

[32] Z. Tan, C. Tan, L. Ma, G. T. Liu, L. Lu, and C. L. Yang, "Shubnikov-de haas oscillations of a single layer graphene under dc current bias," *Phys. Rev. B*, vol. 84, p. 115429, Sep 2011.

[33] S. A. Studenikin, G. Granger, A. Kam, A. S. Sachrajda, Z. R. Wasilewski, and P. J. Poole, "Nonlinear magnetotransport phenomena in high-mobility two-dimensional electrons in ingaas/inp and gaas/algaas," *Phys. Rev. B*, vol. 86, p. 115309, Sep 2012.

[34] D. Leadley, R. Nicholas, J. Harris, and C. Foxon, "Cyclotron phonon emission and electron energy loss rates in gaas-gaalas heterojunctions," *Semiconductor science and technology*, vol. 4, no. 10, p. 879, 1989.

[35] Y. Ma, R. Fletcher, E. Zaremba, M. D'Iorio, C. T. Foxon, and J. J. Harris, "Energy-loss rates of two-dimensional electrons at a $gaas/\mathrm{Al}_x\mathrm{ga}_{1-x}$as interface," *Phys. Rev. B*, vol. 43, pp. 9033–9044, Apr 1991.

[36] T. Scaffidi, N. Nandi, B. Schmidt, A. P. Mackenzie, and J. E. Moore, "Hydrodynamic electron flow and hall viscosity," *Phys. Rev. Lett.*, vol. 118, no. 22, p. 226601, 2017.

[37] E. Ditlefsen and J. Lothe, "Theory of size effects in electrical conductivity," *Philos. Mag.*, vol. 14, no. 130, pp. 759–773, 1966.

[38] C. Beenakker and H. van Houten, "Quantum transport in semiconductor nanostructures," in *Solid state physics*, vol. 44, pp. 1–228, Elsevier, 1991.

[39] G. Gusev, A. Levin, E. Levinson, and A. Bakarov, "Viscous transport and hall viscosity in a two-dimensional electron system," *Phys. Rev. B*, vol. 98, no. 16, p. 161303, 2018.

[40] T. Thornton, M. Roukes, A. Scherer, and B. Van de Gaag, "Boundary scattering in quantum wires," *Phys. Rev. Lett.*, vol. 63, no. 19, p. 2128, 1989.

[41] S. Masubuchi, K. Iguchi, T. Yamaguchi, M. Onuki, M. Arai, K. Watanabe, T. Taniguchi, and T. Machida, "Boundary scattering in ballistic graphene," *Phys. Rev. Lett.*, vol. 109, p. 036601, Jul 2012.

[42] P. J. W. Moll, P. Kushwaha, N. Nandi, B. Schmidt, and A. P. Mackenzie, "Evidence for hydrodynamic electron flow in pdcoo¡sub¿2¡/sub¿," *Science*, vol. 351, no. 6277, pp. 1061–1064, 2016.

[43] J. A. Sulpizio, L. Ella, A. Rozen, J. Birkbeck, D. J. Perello, D. Dutta, M. Ben-Shalom, T. Taniguchi, K. Watanabe, T. Holder, R. Queiroz, A. Principi, A. Stern, T. Scaffidi, A. K. Geim, and S. Ilani, "Visualizing poiseuille flow of hydrodynamic electrons," *Nature*, vol. 576, no. 7785, pp. 75–79, 2019.

[44] L. Bockhorn, A. Hodaei, D. Schuh, W. Wegscheider, and R. J. Haug, "Magnetoresistance in a high mobility two-dimensional electron system as a function of sample geometry," *J. Phys. Conf. Ser.*, vol. 456, p. 012003, Aug. 2013.

[45] A. Hatke, M. Zudov, J. Reno, L. Pfeiffer, and K. West, "Giant negative magnetoresistance in high-mobility two-dimensional electron systems," *Phys. Rev. B*, vol. 85, no. 8, p. 081304, 2012.

[46] R. G. Mani, A. Kriisa, and W. Wegscheider, "Size-dependent giant-magnetoresistance in millimeter scale GaAs/AlGaAs 2d electron devices," *Sci. Rep.*, vol. 3, p. 2747, Sept. 2013.

[47] Q. Shi, P. D. Martin, Q. A. Ebner, M. A. Zudov, L. N. Pfeiffer, and K. W. West, "Colossal negative magnetoresistance in a two-dimensional electron gas," *Phys. Rev. B*, vol. 89, p. 201301, May 2014.

[48] Z. Wang, R. L. Samaraweera, C. Reichl, W. Wegscheider, and R. G. Mani, "Tunable electron heating induced giant magnetoresistance in the high mobility GaAs/AlGaAs 2d electron system," *Sci. Rep.*, vol. 6, p. 38516, Dec. 2016.

[49] R. L. Samaraweera, H.-C. Liu, Z. Wang, C. Reichl, W. Wegscheider, and R. G. Mani, "Mutual influence between current-induced giant magnetoresistance and radiation-induced magnetoresistance oscillations in the GaAs/AlGaAs 2des," *Sci. Rep.*, vol. 7, p. 5074, July 2017.

[50] R. L. Samaraweera, H.-C. Liu, B. Gunawardana, A. Kriisa, C. Reichl, W. Wegscheider, and R. G. Mani, "Coherent backscattering in quasi-ballistic ultra-high mobility GaAs/AlGaAs 2des," *Sci. Rep.*, vol. 8, p. 10061, July 2018.

[51] R. L. Samaraweera, B. Gunawardana, T. R. Nanayakkara, R. C. Munasinghe, A. Kriisa, C. Reichl, W. Wegscheider, and R. G. Mani, "Study of narrow negative magnetoresistance effect in ultra-high mobility gaas/algaas 2des under microwave photoexcitation," *Sci. Rep.*, vol. 10, p. 781, jan 2020.

[52] B. Horn-Cosfeld, J. Schluck, J. Lammert, M. Cerchez, T. Heinzel, K. Pierz, H. W. Schumacher, and D. Mailly, "Relevance of weak and strong classical scattering for

the giant negative magnetoresistance in two-dimensional electron gases," *Phys. Rev. B*, vol. 104, p. 045306, Jul 2021.

[53] M. A. Zudov, I. V. Ponomarev, A. L. Efros, R. R. Du, J. A. Simmons, and J. L. Reno, "New class of magnetoresistance oscillations: Interaction of a two-dimensional electron gas with leaky interface phonons," *Phys. Rev. Lett.*, vol. 86, pp. 3614–3617, Apr. 2001.

[54] L. Bockhorn, P. Barthold, D. Schuh, W. Wegscheider, and R. J. Haug, "Magnetoresistance in a high-mobility two-dimensional electron gas," *Phys. Rev. B*, vol. 83, p. 113301, Mar 2011.

[55] L. Bockhorn, I. V. Gornyi, D. Schuh, C. Reichl, W. Wegscheider, and R. J. Haug, "Magnetoresistance induced by rare strong scatterers in a high-mobility two-dimensional electron gas," *Phys. Rev. B*, vol. 90, p. 165434, Oct 2014.

[56] K. K. Choi, D. C. Tsui, and S. C. Palmateer *Phys. Rev. B*, vol. 33, pp. 8216–8227, Jun 1986.

[57] P. Van Loosdrecht, C. Beenakker, H. Van Houten, J. Williamson, B. Van Wees, J. Mooij, C. Foxon, and J. Harris, "Aharonov-bohm effect in a singly connected point contact," *Phys. Rev. B*, vol. 38, no. 14, p. 10162, 1988.

[58] H. Van Houten, C. Beenakker, P. Van Loosdrecht, T. Thornton, H. Ahmed, M. Pepper, C. Foxon, and J. Harris, "Four-terminal magnetoresistance of a two-dimensional electron-gas constriction in the ballistic regime," *Phys. Rev. B*, vol. 37, no. 14, p. 8534, 1988.

[59] R. G. Mani, K. von Klitzing, and K. Ploog *Phys. Rev. B*, vol. 48, pp. 4571–4574, Aug 1993.

[60] M. Paalanen, D. Tsui, B. Lin, and A. Gossard, "Localization of 2d electrons in gaasalxga1xas heterostructures," *Surf. Sci.*, vol. 142, no. 1, pp. 29–36, 1984.

[61] B. Kramer and A. MacKinnon, "Localization: theory and experiment," *Rep. Prog. Phys.*, vol. 56, no. 12, p. 1469, 1993.

[62] L. Molenkamp and M. de Jong, "Observation of knudsen and gurzhi transport regimes in a two-dimensional wire," *Solid-State Electron.*, vol. 37, no. 4, pp. 551–553, 1994.

[63] R. Gurzhi, "Minimum of resistance in impurity-free conductors," *Sov. Phys. JETP*, vol. 44, p. 771, 1963.

[64] R. Gurzhi, "Hydrodynamic effects in solids at low temperature," *Sov. Phys. Usp*, vol. 11, p. 255, 1968.

[65] G. F. Giuliani and J. J. Quinn, "Lifetime of a quasiparticle in a two-dimensional electron gas," *Phys. Rev. B*, vol. 26, no. 8, p. 4421, 1982.

[66] R. Gurzhi, A. Kalinenko, and A. Kopeliovich, "Hydrodynamic effects in the electrical conductivity of impure metals," *Sov. Phys. JETP*, vol. 69, no. 4, pp. 863–870, 1989.

[67] R. Jaggi, "Electron-fluid model for dc size effect," *J. Appl. Phys.*, vol. 69, no. 2, pp. 816–820, 1991.

[68] M. de Jong and L. Molenkamp, "Hydrodynamic electron flow in high-mobility wires," *Phys. Rev. B*, vol. 51, no. 19, p. 13389, 1995.

[69] L. Eaves, "Quantum hall effect breakdown: analogies with fluid dynamics," *Physica B*, vol. 256-258, pp. 47–51, 1998.

[70] L. Eaves, "A hydrodynamic description of quantum hall effect breakdown," *Physica B*, vol. 272, no. 1-4, pp. 130–132, 1999.

[71] L. Eaves, S. Stoddart, R. Wirtz, A. Neumann, B. Gallagher, P. Main, and M. Henini, "Quantum hall effect breakdown in two-dimensional hole gases," *Physica E*, vol. 6, no. 1, pp. 136–139, 2000.

[72] L. Eaves, "An eddy viscosity model of the dissipative voltage steps in quantum hall effect breakdown," *Physica E*, vol. 9, no. 1, pp. 45–53, 2001.

[73] L. Eaves, "Quantum hall effect breakdown steps: evidence for an instability induced by inter-landau level scattering," *Physica B*, vol. 298, no. 1-4, pp. 1–7, 2001.

[74] A. Martin, K. Benedict, F. Sheard, and L. Eaves, "Model for breakdown of laminar flow of a quantum hall fluid around a charged impurity: comparison with experiment," *Physica E*, vol. 22, no. 1-3, pp. 205–209, 2004.

[75] P. Alekseev, "Negative magnetoresistance in viscous flow of two-dimensional electrons," *Phys. Rev. Lett.*, vol. 117, no. 16, p. 166601, 2016.

[76] H. Guo, E. Ilseven, G. Falkovich, and L. S. Levitov, "Higher-than-ballistic conduction of viscous electron flows," *Proc. Natl. Acad. Sci. U.S.A.*, vol. 114, no. 12, pp. 3068–3073, 2017.

[77] P. S. Alekseev and M. A. Semina, "Hall effect in a ballistic flow of two-dimensional interacting particles," *Phys. Rev. B*, vol. 100, p. 125419, Sep 2019.

[78] P. S. Alekseev and A. P. Alekseeva, "Transverse magnetosonic waves and viscoelastic resonance in a two-dimensional highly viscous electron fluid," *Phys. Rev. Lett.*, vol. 123, p. 236801, Dec 2019.

[79] P. S. Alekseev and A. P. Dmitriev, "Viscosity of two-dimensional electrons," *Phys. Rev. B*, vol. 102, p. 241409, Dec 2020.

[80] I. Matthaiakakis, D. Rodríguez Fernández, C. Tutschku, E. M. Hankiewicz, J. Erdmenger, and R. Meyer, "Functional dependence of hall viscosity induced transverse voltage in two-dimensional fermi liquids," *Phys. Rev. B*, vol. 101, p. 045423, Jan 2020.

[81] O. E. Raichev, G. M. Gusev, A. D. Levin, and A. K. Bakarov, "Manifestations of classical size effect and electronic viscosity in the magnetoresistance of narrow two-dimensional conductors: Theory and experiment," *Phys. Rev. B*, vol. 101, p. 235314, Jun 2020.

[82] A. N. Afanasiev, P. S. Alekseev, A. A. Greshnov, and M. A. Semina, "Ballistic-hydrodynamic phase transition in flow of two-dimensional electrons," *Phys. Rev. B*, vol. 104, p. 195415, Nov 2021.

[83] J. Zaanen, "Electrons go with the flow in exotic material systems," *Science*, vol. 351, pp. 1026–1027, Mar. 2016.

[84] D. A. Bandurin, I. Torre, R. K. Kumar, M. B. Shalom, A. Tomadin, A. Principi, G. H. Auton, E. Khestanova, K. S. Novoselov, I. V. Grigorieva, L. A. Ponomarenko, A. K. Geim, and M. Polini, "Negative local resistance caused by viscous electron backflow in graphene," *Science*, vol. 351, pp. 1055–1058, Mar. 2016.

[85] J. Crossno, J. K. Shi, K. Wang, X. Liu, A. Harzheim, A. Lucas, S. Sachdev, P. Kim, T. Taniguchi, K. Watanabe, T. A. Ohki, and K. C. Fong, "Observation of the dirac fluid and the breakdown of the wiedemann-franz law in graphene," *Science*, vol. 351, pp. 1058–1061, Mar. 2016.

[86] L. Levitov and G. Falkovich, "Electron viscosity, current vortices and negative nonlocal resistance in graphene," *Nat. Phys.*, vol. 12, pp. 672–676, Feb. 2016.

[87] A. I. Berdyugin, S. G. Xu, F. M. D. Pellegrino, R. K. Kumar, A. Principi, I. Torre, M. B. Shalom, T. Taniguchi, K. Watanabe, I. V. Grigorieva, M. Polini, A. K. Geim, and D. A. Bandurin, "Measuring hall viscosity of graphene's electron fluid," *Science*, vol. 364, pp. 162–165, Apr. 2019.

[88] P. Gallagher, C.-S. Yang, T. Lyu, F. Tian, R. Kou, H. Zhang, K. Watanabe, T. Taniguchi, and F. Wang, "Quantum-critical conductivity of the dirac fluid in graphene," *Science*, vol. 364, no. 6436, pp. 158–162, 2019.

[89] L. Ella, A. Rozen, J. Birkbeck, M. Ben-Shalom, D. Perello, J. Zultak, T. Taniguchi, K. Watanabe, A. K. Geim, S. Ilani, and J. A. Sulpizio, "Simultaneous voltage and current density imaging of flowing electrons in two dimensions," *Nat. Nanotechnol.*, vol. 14, no. 5, pp. 480–487, 2019.

[90] M. J. H. Ku, T. X. Zhou, Q. Li, Y. J. Shin, J. K. Shi, C. Burch, L. E. Anderson, A. T. Pierce, Y. Xie, A. Hamo, U. Vool, H. Zhang, F. Casola, T. Taniguchi, K. Watanabe, M. M. Fogler, P. Kim, A. Yacoby, and R. L. Walsworth, "Imaging viscous flow of the dirac fluid in graphene," *Nature*, vol. 583, pp. 537–541, July 2020.

[91] Y. A. Pusep, M. D. Teodoro, V. Laurindo, E. R. Cardozo de Oliveira, G. M. Gusev, and A. K. Bakarov, "Diffusion of photoexcited holes in a viscous electron fluid," *Phys. Rev. Lett.*, vol. 128, p. 136801, Mar 2022.

[92] J. Gooth, F. Menges, N. Kumar, V. Sü, C. Shekhar, Y. Sun, U. Drechsler, R. Zierold, C. Felser, and B. Gotsmann, "Thermal and electrical signatures of a hydrodynamic electron fluid in tungsten diphosphide," *Nat. Commun.*, vol. 9, p. 4093, Oct. 2018.

[93] A. D. Levin, G. M. Gusev, E. V. Levinson, Z. D. Kvon, and A. K. Bakarov, "Vorticity-induced negative nonlocal resistance in a viscous two-dimensional electron system," *Phys. Rev. B*, vol. 97, p. 245308, Jun 2018.

[94] G. M. Gusev, A. D. Levin, E. V. Levinson, and A. K. Bakarov, "Viscous electron flow in mesoscopic two-dimensional electron gas," *AIP Adv.*, vol. 8, p. 025318, Feb. 2018.

[95] B. A. Braem, F. M. D. Pellegrino, A. Principi, M. Röösli, C. Gold, S. Hennel, J. V. Koski, M. Berl, W. Dietsche, W. Wegscheider, M. Polini, T. Ihn, and K. Ensslin, "Scanning gate microscopy in a viscous electron fluid," *Phys. Rev. B*, vol. 98, p. 241304, Dec 2018.

[96] G. M. Gusev, A. S. Jaroshevich, A. D. Levin, Z. D. Kvon, and A. K. Bakarov, "Stokes flow around an obstacle in viscous two-dimensional electron liquid," *Sci. Rep.*, vol. 10, p. 7860, May 2020.

[97] A. C. Keser, D. Q. Wang, O. Klochan, D. Y. H. Ho, O. A. Tkachenko, V. A. Tkachenko, D. Culcer, S. Adam, I. Farrer, D. A. Ritchie, O. P. Sushkov, and A. R. Hamilton, "Geometric control of universal hydrodynamic flow in a two-dimensional electron fluid," *Phys. Rev. X*, vol. 11, p. 031030, Aug 2021.

[98] A. Gupta, J. J. Heremans, G. Kataria, M. Chandra, S. Fallahi, G. C. Gardner, and M. J. Manfra, "Hydrodynamic and ballistic transport over large length scales in GaAs/AlGaAs," *Phys. Rev. Lett.*, vol. 126, p. 076803, Feb 2021.

[99] E. Mönch, S. O. Potashin, K. Lindner, I. Yahniuk, L. E. Golub, V. Y. Kachorovskii, V. V. Bel'kov, R. Huber, K. Watanabe, T. Taniguchi, J. Eroms, D. Weiss, and S. D. Ganichev, "Ratchet effect in spatially modulated bilayer graphene: Signature of hydrodynamic transport," *Phys. Rev. B*, vol. 105, p. 045404, Jan 2022.

[100] M. G. Vavilov and I. L. Aleiner, "Magnetotransport in a two-dimensional electron gas at large filling factors," *Phys. Rev. B*, vol. 69, p. 035303, Jan 2004.

[101] I. A. Dmitriev, M. G. Vavilov, I. L. Aleiner, A. D. Mirlin, and D. G. Polyakov, "Theory of microwave-induced oscillations in the magnetoconductivity of a two-dimensional electron gas," *Phys. Rev. B*, vol. 71, p. 115316, Mar 2005.

[102] M. G. Vavilov, I. L. Aleiner, and L. I. Glazman, "Nonlinear resistivity of a two-dimensional electron gas in a magnetic field," *Phys. Rev. B*, vol. 76, no. 11, p. 115331, 2007.

[103] M. Khodas and M. G. Vavilov, "Effect of microwave radiation on the nonlinear resistivity of a two-dimensional electron gas at large filling factors," *Phys. Rev. B*, vol. 78, p. 245319, Dec 2008.

[104] C. Chaubet, A. Raymond, and D. Dur, "Heating of two-dimensional electrons by a high electric field in a quantizing magnetic field: Consequences in landau emission and in the quantum hall effect," *Phys. Rev. B*, vol. 52, pp. 11178–11192, Oct 1995.

[105] M. J. Manfra, "Molecular beam epitaxy of ultra-high-quality algaas/gaas heterostructures: enabling physics in low-dimensional electronic systems," *Annu. Rev. Condens. Matter Phys.*, vol. 5, no. 1, pp. 347–373, 2014.

[106] N. C. Mamani, G. M. Gusev, T. E. Lamas, A. K. Bakarov, and O. E. Raichev, "Resonance oscillations of magnetoresistance in double quantum wells," *Phys. Rev. B*, vol. 77, p. 205327, May 2008.

[107] A. T. Hatke, M. A. Zudov, L. N. Pfeiffer, and K. W. West, "Temperature dependence of microwave photoresistance in 2d electron systems," *Phys. Rev. Lett.*, vol. 102, p. 066804, Feb 2009.

[108] A. T. Hatke, M. A. Zudov, L. N. Pfeiffer, and K. W. West, "Phonon-induced resistance oscillations in 2d systems with a very high electron mobility," *Phys. Rev. Lett.*, vol. 102, p. 086808, Feb 2009.

[109] A. V. Chaplik, "A chaplik," *Sov. Phys. JETP*, vol. 33, no. 8, p. 997, 1971.

[110] A. T. Hatke, H.-S. Chiang, M. A. Zudov, L. N. Pfeiffer, and K. W. West, "Microwave photoresistance in dc-driven 2d systems at cyclotron resonance subharmonics," *Phys. Rev. Lett.*, vol. 101, p. 246811, Dec 2008.

[111] P. T. Coleridge, R. Stoner, and R. Fletcher, "Low-field transport coefficients in," *Phys. Rev. B*, vol. 39, pp. 1120–1124, Jan 1989.

[112] A. Yacoby, U. Sivan, C. P. Umbach, and J. M. Hong, "Interference and dephasing by electron-electron interaction on length scales shorter than the elastic mean free path," *Phys. Rev. Lett.*, vol. 66, pp. 1938–1941, Apr 1991.

[113] P. Y. Yu and M. Cardona, *Fundamentals of Semiconductors*. Springer Berlin Heidelberg, 2005.

[114] N. Mamani, G. Gusev, O. Raichev, T. Lamas, and A. Bakarov, "Nonlinear transport and oscillating magnetoresistance in double quantum wells," *Phys. Rev. B*, vol. 80, no. 7, p. 075308, 2009.

[115] R. J. Blaikie, D. R. S. Cumming, J. R. A. Cleaver, H. Ahmed, and K. Nakazato, "Electron transport in multiprobe quantum wires anomalous magnetoresistance effects," *J. Appl. Phys.*, vol. 78, no. 1, pp. 330–343, 1995.